Ultra-Low-Temperature Silicon and Germanium-on-Silicon Avalanche Photodiodes: Modeling, Design, and Characterization

THÈSE N^{O} 6451 (2014)

PRÉSENTÉE LE 22 DÉCEMBRE 2014
À LA FACULTÉ DES SCIENCES ET TECHNIQUES DE L'INGENIEUR
GROUPE DE SCIENTIFIQUES IC
PROGRAMME DOCTORAL EN GÉNIE ÉLECTRIQUE

ÉCOLE POLYTECHNIQUE FÉDÉRALE DE LAUSANNE

POUR L'OBTENTION DU GRADE DE DOCTEUR ÈS SCIENCES

PAR

Mahdi AMINIAN

acceptée sur proposition du jury:

Prof. J.-Ph. Thiran, président du jury
Prof. E. Charbon, directeur de thèse
Prof. E. Cantatore, rapporteur
Prof. G. De Micheli, rapporteur
Prof. L. K. Nanver, rapporteuse

ÉCOLE POLYTECHNIQUE
FÉDÉRALE DE LAUSANNE
Suisse
2014

To my parents, Parvin & Hassan
for their love, endless support
and encouragement

Acknowledgements

It has been a long road, but now it's the end. Without the help and support from a large number of people, this work would not have been ended. Working with such great colleagues and friends is the most worthy part during my PhD, in my opinion.

First and foremost I would like to express my special thanks to my supervisor Prof. Edoardo Charbon, for all of his supports and encouragements. I have enjoyed from the opportunity to learn from your experience and knowledge. Your patience, good advises, and impressive comments are so appreciated.

I would also like to thank Prof. Lis Nanver from TUDelft for her tremendous guides. I am sure that this work could not have been possible without your advices. I am grateful to Dr. Amir Sammak as a best collaborator in fabrications and working together. Moreover, Lin Qi and other DIMES staffs at TUDelft, thank you for the chance to work with you. I am so proud to work with you all.

I would especially like to thank my examiners, Professors Jean-Philippe Thiran, Giovanni De Micheli, Eugenio Cantatore, and Lis Nanver, who provided encouraging and constructive feedbacks. I am grateful for their thoughtful and detailed comments.

I would like to express my sincere appreciation to my former supervisor, Prof. Morteza Saheb Zamani who encouraged me in this path and all of his supports. I learnt a lot from you and it was my honor to be your student and work with you. Also, I'm grateful to Prof. Hossein Pedram and Prof. Mohammad Kazem Akbari for supporting me spiritually throughout this work.

This thesis was funded by Switzerland Nano-tera program, with the goal of using engineering and information technology to improve health and security, and to broaden the management of energy and the environment. I would like to thank the organisation for their generous support, and Prof. Jerome Faist as the head of Irsens project, Dr. Yargo Bonetti, and all of the collaborators in this project.

My colleagues at EPFL and TUdelft have a significant role in my project. I wish to thank Dr. Hyung-June Yoon, Dr. Claudio Bruschini and Mauro Scandiuzzo for their great experiences and so helpful discussions. Special thanks to our lab members, Joëlle Radigois, Chantal Schneeberger, Francois Powolony, Christian Mester, Chockalingam Veerappan, Esteban Venialgo, and all other members at AQUA and LAP groups for their supports.

I should thank Wladek Grabinski and NANOLAB group for the time they spent helping me through cryogenic experiments, and Matthieu Legré and ID Quantique (IDQ) company to provide us the laser sources. I would also like to thank Dr. Nicholas Preyss and Telecommunications Circuits Laboratory, Oriol Lopez Sanchez and Prof. Andras Kis (Laboratory of Nanoscale Electronics and Structures), and Mehran Shahmohammdi for electrical and optical measurements support. I'm also grateful to Somayyeh Rahimian and Mohammad Amin Shoaie for helping me during my experiments and writing.

I am indebted to all my friends in Lausanne and Delft who have supported me over the last few years, Somayyeh, Amin, Samira, Farhang, Atefeh and Ali, Maryam and Hassan, Samira and Mokhtar, Sara and Naser, Samira and Saleh, Mahboobeh and Hadi, Vahid, Nasir, Hadi, Amir, and all of my lovely friends. I wish the best for you in your life.

The deepest thanks to my parents and my brother, Reza, for their continuous support, their love, and encouragement they have given me over the years. Words cannot express how grateful I am. I would just like to say that I love you.

Mahdi Aminian
Lausanne, October 2014

Abstract

Progress in the research and development of novel sensors and their applications has become essential to address some major challenges of today's society, such as monitoring and control of our environment and of our quality of life, and to ensure data security. Highly sensitive photon counters operating in the telecom band at 1.55 μm are essential in quantum communications for implementing quantum key distribution (QKD) protocols, and in several imaging techniques based on near infrared sources, such as Raman spectroscopy and time-of-flight rangefinding.

In this thesis we propose the use of photodiodes fabricated in planar technologies to address the detection problem in these applications. A number of solutions exist, optimized for these wavelengths, based on Germanium (Ge) and other III-V materials. In this thesis we focused on Ge thanks to its versatility and ease to use in the clean room. The main advantage of this material is in fact a good compatibility with Silicon and standard CMOS processes. Note that the proposed technology is not based on Silicon/Germanium (SiGe), whereby Ge is used to strain Si to achieve higher bandwidth in Si, not higher sensitivity. In our *pure* Ge approach, Ge is grafted onto Si (Ge-on-Si), achieving high responsivity (up to 0.231 A/W) at wavelengths of 900nm and higher. The proposed devices can operate in avalanche mode (avalanche photodiodes – APDs), and in Geiger mode (Geiger mode APDs – GAPDs or single-photon avalanche diodes – SPADs), while dark currents at 1V reverse bias, respectively dark count rates, are rather low (10 fA resp. 1000 cps).

To combine the advantages of Ge with single-photon sensitivity and excellent timing resolution of Si-based SPADs, this thesis proposes a new generation of SPADs, achieved in collaboration with Prof. Nanver at TUDelft, aimed at the near-infrared range. The fabrication process of the Ge-on-Si SPAD approach, which we are investigating together with the TUDelft group, consists of a standard CMOS process combined with post-processing steps to grow Ge on top of a Si/SiO_2 layer. One of the challenges of this approach is to prevent high noise caused by the lattice mismatch between Ge and Si, as well as potential instability of the process that could lead to compatibility problems with existing flows.

In our study we have investigated the potential for a new generation of massively parallel, Ge-on-Si sensors fabricated in fully CMOS compatible technology. The objective was to address the next challenges of super-parallel pixel arrays, while exploiting the advantages of the Ge substrate, *in primis* its higher mobility. Ultimately, we believe that this technology will become the core of next-generation processors and embedded accelerators operating at very high clock frequencies and, possibly, controlled optically, an idea we started exploring in fully

CMOS circuits.

The key technology developed in the thesis is a selective chemical-vapor deposition (CVD) epitaxial growth. A novel processing procedure was developed for the p^+ Ge surface doping by a sequence of pure-Ga and pure-B depositions (*PureGaB*). The deposition of a nm-thin Ga and B layer-stack fulfils two functions: the Ga forms an ultrashallow p^+n junction on the surface of Ge islands, which allows highly sensitive NIR photodiode detection in the Ge itself, and the B-layer forms a barrier that protects the Ge/Ga layers against oxidation when exposed to air and against spiking during metallization. The resulting p+n diodes have exceptionally good I-V characteristics with ideality factor of ~1.1 and low saturation currents. They can be operated both in proportional and in Geiger mode, and exhibit relatively low dark counts, as low as 10 kHz at 1 V excess reverse bias. The dark current at 1 V reverse bias is as low as 2 pA and 20 pA for $2 \times 2\ \mu m^2$ and $2 \times 20\ \mu m^2$ devices, respectively. Higher IR-induced current than that induced by visible light confirms the sensitivity of Ge photodiodes at room temperature. The timing response (Jitter) for the APD when exposed to a pulsed laser at 637 nm and 1 V excess bias is measured as 900 ps full width of half maximum (FWHM). This fabrication technology was used not only in single detectors but also in arrays, with the creation of imaging arrays with high yield.

We also looked at techniques to improve red and infrared sensitivity in conventional deep-submicron CMOS processes, by careful selection of standard layers at high depths in the Si substrate. Using the proposed approach, 12 μm-diameter SPADs were fabricated in 0.18 μm CMOS technology achieving peak photon detection probability at 500 nm and showing low dark count rates (363 cps) at room temperature and considerably lower rates at cryogenic temperatures (77 K), while the FWHM timing jitter is as low as 76 ps.

That of cryogenic SPADs is a novel research direction and in this thesis it was advocated as a significant trend for the future of optical sensing, especially in mid-infrared wavelengths. Low temperature characterizations reported in this thesis exposed how the relevant properties of fabrication materials, such as strength, thermal conductivity, ductility, and electrical resistance are changing. One of the most important properties is superconductivity in materials cooled to extreme temperatures: this is an important trend that will be pursued in the future activities of our group.

Key words: Avalanche Photodiode, APD, Cryogenic, CMOS compatible, Germanium, Ge-on-Si, Near-Infrared, NIR, Photodiode, Single photon avalanche diode, SPAD, SPAD array

Résumé

Les progrès réalisés dans la recherche et le développement de nouveaux capteurs et de leurs applications sont devenus essentiels pour relever certains défis majeurs de la société d'aujourd'hui, tels que la surveillance et le contrôle de notre environnement et de notre qualité de vie, et pour assurer la sécurité des données. Les compteurs de photons à haute sensibilité, fonctionnant dans la bande des télécommunications de 1,55 μm, sont essentiels dans les communications quantiques pour la mise en œuvre des protocoles de distribution de clés quantiques (QKD), ainsi que dans plusieurs techniques d'imagerie basées sur des sources dans le proche infrarouge, telles que la spectroscopie Raman et la télémétrie à temps de vol.

Dans cette thèse, nous proposons l'utilisation de photodiodes fabriquées à l'aide de technologies planaires pour résoudre le problème de détection dans ces applications. Un certain nombre de solutions, optimisées pour ces longueurs d'onde, existent et sont basées sur le Germanium (Ge) ainsi que d'autres matériaux III-V. Dans cette thèse, nous nous sommes concentrés sur le Ge à cause de sa polyvalence et sa facilité d'utilisation en salle blanche. Le principal avantage de ce matériau est une bonne compatibilité avec le silicium et les procès CMOS standard. A noter que la technologie proposée n'est pas à base de silicium/germanium (SiGe), dans lequel le Ge est utilisée pour contraindre mécaniquement le Si afin d'obtenir une bande passante plus élevée en Si, plutôt qu'une sensibilité supérieure. Dans notre approche à Ge pure, le Ge est greffé sur le Si (Ge-sur-Si), permettant un facteur de réponse élevé (jusqu'à 0,231 A/W) à des longueurs d'onde de 900 nm et plus. Les dispositifs proposés peuvent fonctionner en mode avalanche (photodiodes à avalanche - APDs), et en mode Geiger (APD en mode Geiger - GAPDs ou diodes avalanche à photon unique - SPADs), tandis que les courants d'obscurité à 1 V de polarisation inverse, respectivement les taux de comptages obscures, sont contenus (10 fA resp. 1000 cps).

Pour combiner les avantages du Ge, avec une sensibilité au photon unique, ainsi que l'excellente résolution temporelle des SPAD à base de Si, cette thèse propose une nouvelle génération de SPAD visant la région du proche infrarouge, réalisée en collaboration avec le professeur Nanver à TUDelft. Le procédé de fabrication de l'approche Ge-sur-Si SPAD, que nous étudions avec le groupe TUDelft, consiste en un procédé CMOS standard combiné avec des étapes de post-traitement afin de développer une couche de Ge sur un substrat Si/SiO_2. L'un des défis de cette approche est d'empêcher l'apparition d'un bruit fort causé par le "lattice mismatch" entre Ge et Si, ainsi que l'instabilité potentielle du procédé qui pourrait conduire à des problèmes de compatibilité avec les flux existants.

Dans cette étude, nous avons étudié la possibilité d'une nouvelle génération de capteurs Ge-sur-Si massivement parallèles, fabriqués dans une technologie pleinement compatible avec le CMOS. L'objectif était de répondre aux prochains défis des matrices de pixels super-parallèles, tout en exploitant les avantages d'un substrat Ge, principalement sa plus grande mobilité. En fin de compte, nous pensons que cette technologie sera au cœur des processeurs et des accélérateurs embarqués de prochaine génération fonctionnant à des fréquences d'horloge très élevées, et éventuellement contrôlées optiquement, une idée que nous avons commencé à explorer avec des circuits entièrement fabriqués en technologie CMOS.

La principale technologie développée dans cette thèse est la croissance épitaxiale par déposition en phase vapeur (CVD) sélective. Une nouvelle procédure de traitement a été développée pour le dopage p^+ d'une surface Ge par une séquence de dépositions Ga pure et B pure (PureGaB). Le dépôt d'une couche nanométrique de Ga et B remplit deux fonctions : le Ga forme une jonction p^+n ultrafine à la surface d'îlots de Ge, permettant une détection à haute sensibilité de la photodiode dans le proche infrarouge par le Ge lui-même, et la couche de B forme une barrière qui protège les couches de Ge/Ga de l'oxydation lorsqu'elles sont exposées à l'air, et de la formation de pointes pendant la métallisation. Les diodes p^+n obtenues ont des caractéristiques I-V exceptionnelles avec un facteur d'idéalité d'environ 1.1 et des courants de saturation faibles. Elles peuvent être utilisées à la fois en mode linéaire et en mode Geiger, et présentent des taux de comptages obscures relativement faibles, aussi bas que 10 kHz à 1 V de polarisation inverse. Le courant d'obscurité sous polarisation inverse de 1 V est faible, respectivement de l'ordre de 2 pA et 20 pA pour des tailles de $2 \times 2\ \mu m^2$ et $2 \times 20\ \mu m^2$. Un courant induit par IR supérieur à celui induit par la lumiére visible confirme la sensibilité des photodiodes Ge à température ambiante. La gigue pour les APD lorsqu'elles sont exposées à un laser pulsé de 637 nm et sous polarisation inverse de 1 V est mesurée à 900 ps à largeur de mi-hauteur (FWHM). Cette technique de fabrication a été utilisée non seulement dans les détecteurs individuels, mais également dans des matrices, avec création d'un réseau d'imagerie avec un rendement élevé.

Nous avons également étudié des techniques pour améliorer la sensibilité rouge et infrarouge dans les procédés CMOS classiques fortement submicroniques par une sélection rigoureuse des couches standards à haute profondeur dans le substrat de silicium. En utilisant l'approche proposée, des SPAD de 12 μm de diamètre ont été fabriqués en technologie CMOS 0.18 μm, atteignant une probabilité de détection de photons maximale à 500 nm et montrant des taux de comptages obscures faibles (de 363 cps) à température ambiante, ainsi que des taux nettement inférieurs à des températures cryogéniques (77 K), tandis que la gigue temporelle FWHM est aussi bas que 76 ps.

Les SPADs cryogéniques sont une nouvelle direction pour la recherche. Dans cette thèse, ils ont été préconisés comme une tendance importante pour l'avenir de la détection optique, en particulier dans les longueurs d'onde de l'infrarouge moyen. Les caractérisations à basse température présentées dans cette thèse ont exposé comment les propriétés pertinentes des matériaux de fabrication, telles que la résistance, la conductivité thermique, la ductilité et la résistance électrique sont en constante évolution. Une des propriétés les plus importantes est la supraconductivité dans des matériaux refroidis à température extrême : il s'agit d'une tendance importante qui sera poursuivi dans les activités futures de notre groupe.

Mots clefs : APD, Compatible CMOS, Cryogénique, Diode avalanche à photon unique, Germanium, Ge-sur-Si, Matrice SPAD, Matrice SPAD Photodiode à avalanche, NIR, Photodiode, Photodiode à avalanche, Proche Infra-rouge, SPAD

Contents

Acknowledgements **i**

Abstract (English/Français) **iii**

List of figures **xiii**

List of tables **xvii**

List of Abbreviations **xix**

1 Introduction **1**

1.1 Integrated sensing platform for gas and liquid (IrSens) 2

1.1.1 Detection and signal analysis 4

1.1.2 Optical sensor for human breath analysis 5

1.1.3 Optical sensor for liquids 6

1.2 Basics of photodetection 7

1.2.1 p-i-n photodiode 8

1.3 Challenges in building APD/SPAD 11

1.3.1 Silicon SPADs 12

1.3.2 Germanium SPADs 12

1.4 State-of-the-art in Si and Ge Photodiodes 13

1.4.1 Si/Ge photodetectors 14

1.4.2 Resonant Cavity-Enhanced Schottky photodetectors 15

1.4.3 Waveguide Si/Ge photodedetectors 15

1.4.4 Ge APDs 16

1.5 Thesis contributions and organization 17

2 Visible and Near-infrared SPADs **19**

2.1 Principles of Single Photon Avalanche Diode (SPAD) 19

2.1.1 Operation 21

2.1.2 Premature edge breakdown and guard ring 22

2.1.3 Dark count rate (DCR) 23

2.1.4 Responsivity and Quantum Efficiency (QE) 23

2.1.5 Photon Detection Probability (PDP) 24

2.1.6 Afterpulsing probability 25

2.1.7 Timing jitter 26
2.2 Si SPAD modeling and implementation in 180-nm CMOS 27
2.2.1 Vertical junction photodiode 27
2.2.2 Deep pn junction 28
2.2.3 Integrated quenching circuits 29
2.2.4 TCAD simulation 30
2.3 Ge-on-Si SPAD implementation 33
2.3.1 Ge-on-Si mushroom structure 33
2.3.2 Process flow 36
2.3.3 Ge-on-Si SPAD farm design 39

3 Geiger Mode Operation of Experimental SPADs 43
3.1 Si SPAD general characterization 43
3.1.1 Geiger mode operation 44
3.1.2 I-V characteristic 44
3.1.3 Light Emission Test 45
3.1.4 Dark count rate 46
3.1.5 Dark count rate versus temperature 47
3.1.6 Arrhenius plot 48
3.1.7 Photon detection probability 49
3.1.8 Timing jitter 50
3.1.9 Afterpulsing probability 52
3.1.10 Performance summary 52
3.2 Ge-on-Si SPAD Characterization 54
3.2.1 I-V characteristic 54
3.2.2 CV profiling 54
3.2.3 Geiger mode operation 55
3.2.4 DCR 55
3.2.5 Photoresponse 56
3.2.6 Timing jitter 57
3.2.7 Performance summary 58

4 Near-Infrared Ge-on-Si APD and SPAD array 61
4.1 Ge-on-Si 4×4 array simulation and implementation 61
4.1.1 JFET-pixel and NPN-readout array 61
4.1.2 JFET-pixel and PNP-differential-amplifier-readout array 62
4.1.3 JFET-pixel and common-emitter-amplifier-readout array 63
4.1.4 4×4 array implementation 63
4.2 Ge-on-Si 300×1 APD array 64
4.2.1 Ge-on-Si Line array design 65
4.2.2 Electrical characterization 67
4.2.3 Optical characterization 68
4.3 Ge-on-Si Photomultiplier line array (GePM) 70

4.3.1 Device fabrication and structure 70
4.3.2 Electrical characterization 72

5 Cryogenic Experimentation **73**
5.1 Temperature dependence of semiconductor properties 74
5.2 Cryogenic setup 76
5.3 Si SPAD measurements 78
5.3.1 Breakdown voltage 79
5.3.2 DCR versus temperature 80
5.3.3 Activation energy in low temperature 80
5.4 Cryogenic characterization of Ge-on-Si line array 82
5.4.1 Dark current temperature dependence 82
5.4.2 Ideality factor versus temperature 85
5.4.3 Low temperature photoresponse 86
5.4.4 Low temperature optical gain 87
5.4.5 Performance summary 91

6 Conclusions **93**
6.1 Achieved results 93
6.2 Future developments 94

Bibliography **102**

Curriculum Vitae **103**

List of Figures

1.1 General view of IrSens requirements . . . 3
1.2 IrSens schematic drawing . . . 5
1.3 Absorption coefficient versus wavelength . . . 8
1.4 PIN photodiode energy band diagram . . . 10
1.5 Germanium utilization . . . 13
1.6 Lattice mismatch between Ge and Si . . . 13
1.7 Back-illuminated Ge-SOI Schottkey photodetector . . . 14
1.8 Cross-section of the p-i-n Ge photodetector . . . 15
1.9 RCE Schottky photodetector . . . 16
1.10 p-i-n Ge photodetector integrated in SOI waveguide . . . 16
1.11 Mesa and Waveguide-type SiGe APD . . . 17

2.1 Impact ionization . . . 20
2.2 Photodiode operation modes . . . 21
2.3 Quenching mechanism . . . 22
2.4 Typical CMOS SPAD schematic . . . 22
2.5 Premature edge breakdown . . . 23
2.6 Schematic of PDP setup . . . 25
2.7 Three conventional SPAD structures . . . 27
2.8 Cross-section and schematic of the vertical junction SPAD structure . . . 28
2.9 Cross-section and schematic of the deep junction SPAD structure . . . 29
2.10 Resistor-inverter quenching . . . 29
2.11 Medici simulation of SPAD1 electric field . . . 30
2.12 Medici simulation of SPAD_RED electric field . . . 31
2.13 Medici simulation of SPAD_RED electric field without guard ring . . . 31
2.14 TCAD MEDICI simulation of current-voltage . . . 32
2.15 Ge-on-Si mushroom structure . . . 34
2.16 Top-view optical image of selective Ge-on-Si . . . 36
2.17 Schematic process flow for the PureGaB Ge-on-Si photodetector . . . 37
2.18 Cross-sectional TEM image of a Ge-island . . . 38
2.19 Top-view SEM images of Ge-islands . . . 38
2.20 Epitaxial n-Ge and PureGaB deposition . . . 39
2.21 Full chip layout of Ge-on-Si SPAD farm . . . 40

2.22 PureB/PureGaB dopant-deposition technology for photodiodes 41

3.1 Biasing circuit and Geiger pulses 44
3.2 Geiger pulses for SPAD_RED 45
3.3 Dark current for various SPAD sizes 45
3.4 Light emission test 46
3.5 Dark counts rate for various device active area 46
3.6 Dark count rate (DCR) from 310 K to 230 K 48
3.7 Arrhenius plot of DCR 49
3.8 PDP measurement 50
3.9 PDP for the 12 μm active diameter device 50
3.10 Jitter performance at wavelength of 785nm 51
3.11 Jitter performance at wavelength of 637nm 52
3.12 Afterpulsing distribution 53
3.13 I-V characteristics for 2×2 μm^2 and 2×20 μm^2 device area 54
3.14 C-V profiling for two different sizes 55
3.15 The SPAD biasing and test circuit 56
3.16 Dark count rate for three devices 56
3.17 Dark current and photo-response 57
3.18 I_d/I_{ref} of the 2×20 μm^2 APD in the NIR spectrum 57
3.19 Jitter performance of the 2×2 μm^2 APD 58

4.1 Block diagram of a 4×4 SPAD pixel array 62
4.2 JFET type pixel and NPN readout circuit 62
4.3 JFET-resistor type pixel and PNP-differential-amplifier readout circuit 63
4.4 JFET-resistor type pixel and PNP CE-amplifier readout circuit 63
4.5 Full chip layout of different 4 × 4 SPAD arrays 64
4.6 Photomicrograph of a 4 × 4 SPAD pixel array 65
4.7 Schematic of Ge-on-Si Line array 65
4.8 Schematic process flows of the PureGaB Ge-on-Si photodetector arrays 66
4.9 Top-view cell and the microscopic-view of the Ge APD design 67
4.10 I-V characteristics of the Ge APDs across the array for two designs 68
4.11 Reverse bias I-V characteristics of the Ge APDs 68
4.12 I_D/I_{ref} photo-response of the 26×26 μm^2 PureGaB Ge APD 69
4.13 Schematic cross section, TEM and SEM of a PureGaB Ge-on-Si photodiode . . 70
4.14 Optical images of single, quad, and hexa pixels and a TEM image of a quad pixel 71
4.15 Dark current in room temperature for different GePM pixel types 72

5.1 Carrier concentration versus reciprocal temperature for silicon 76
5.2 Block diagram of a Cryogenic Prober 77
5.3 Cooling system and measurement instruments 78
5.4 Breakdown voltage temperature dependence 79
5.5 Dark count rate (DCR) 80

5.6 Arrhenius plot of DCR 81
5.7 Dark current versus temperature 83
5.8 Reverse bias current spread across 70 devices at 77 K 84
5.9 Forward bias current spread across 70 devices at 77 K 84
5.10 Ideality factor for various temperature 86
5.11 Data acquisition system for testing the photomultipliers 87
5.12 Responsivity for three wavelengths at 77 K 88
5.13 Quantum efficiency for three wavelengths at 77 K 88
5.14 Optical gain as a function of reverse voltage at 77 K 89
5.15 Optical gain spread across 70 devices measured at 940 nm and 77 K 90
5.16 Spreading of maximum optical gain across 70 devices measured at 77 K 90

List of Tables

1.1 Some photonic parameters 8

2.1 Parameter values used in simulations 33

3.1 Inactive distance calculation 47
3.2 Timing jitter for SPAD1 and SPAD_RED 51
3.3 Silicon SPADs performance summary and comparison 53
3.4 Performance of Ge-on-Si photodiodes in conventional mode 58
3.5 Performance of Ge-on-Si photodiodes in APD/SPAD mode 58

4.1 Comparison of light sensitivity of the Ge and Si APDs 69
4.2 Geometrical differences the GePMs 71

5.1 Energy gap equation constants 74
5.2 Some properties of Nitrogen and Helium-4 77
5.3 Summary of performance of the GePMs 91
5.4 Summary of overall best performance 91

List of Abbreviations

AP	Afterpulsing Probability
APD	Avalanche Photodiode
As	Arsenic
B	Boron
$C-V$	Capacitance-Voltage
$CMOS$	Complementary Metal Oxide Semiconductor
CVD	Chemical Vapor Deposition
DCR	Dark Count Rate
$FLIM$	Fluorescence Lifetime Imaging (Microscopy)
$FWHM$	Full Width at Half Maximum
Ga	Gallium
$GAPD$	Geiger mode Avalanche Photodiode
Ge	Germanium
$GePM$	Germanium Photomultiplier
$Ge-on-Si$	Germanium on Silicon
He	Helium
$I-V$	Current-Voltage
IR	Infrared
LET	Light Emission Test
LHe	Liquid Helium
$LN2$	Liquid Nitrogen
$MTTF$	Mean Time To Failure
N	Nitrogen
NIR	Near Infrared
PDP	Photon Detection Probability
PEB	Premature Edge Breakdown
PMT	Photomultiplier Tube
QCL	Quantum Cascade Laser
$QCLAS$	QCL Absorption Spectroscopy
QCD	Quantum Cascade Detector
QE	Quantum Efficiency
R	Responsivity
Si	Silicon

SOI	Silicon-on-Insulator
SPAD	Single Photon Avalanche Diode
UV	Ultraviolet

1 Introduction

Progressing of sensors and their applications has become one of the key ingredients in the technological development of the industrialized world. Some major challenges of today's society such as monitoring and controlling the environment and the quality of life can be addressed by sensor developments. In recent years, semiconductor-based sensors for gas and liquid detection have experienced a great development. These devices have the benefit of relatively cheap manufacturing, while they suffer from limited sensitivity. To improve the sensitivity of devices, developing optical-based sensors is in great demand.

Techniques based on *optical absorption* offer the possibility to realize a non-invasive and highly sensitive detection platform for both gases and analytes dissolved in liquids. With this technique it is possible to probe the vibrational frequencies of the targeted molecules, most of which are located in the near and mid-infrared range, and to obtain an unambiguous signature of the investigated gas or liquid. Although the general principles of chemical sensing deploying optical methods are well-known and well-established in chemistry, recent developments, particularly in the field of infrared photonics, will lead to a real breakthrough in this technology.

Due to the progress in the telecommunication industry, now it is possible to fabricate low-cost semiconductor optical sources with very high performance and low power consumption. The invention of the quantum cascade laser and recent improvements in its room temperature performance allow the generation of single mode emission at room temperature across the whole fingerprint region relevant for chemical sensing. Progress in photonic bandgap structures leads to fabricating the essential interaction elements using low-cost materials such as Silicon (Si). Finally, novel semiconductor technologies have also triggered progress in the area of mid-infrared detectors.

In near-infrared range, several research activities are currently focused on Germanium (Ge). The advantage of this material is its compatibility with Silicon and standard CMOS processes as well as its much higher absorption coefficient as compared to Si. The availability of SiGe photodetectors and their convenient range of bias voltage allow one to achieve various sensitivity and efficiency levels [1]. However, in these devices, Ge is used to strain Si, so as to achieve higher speeds. On the contrary, the focus of this thesis is on pure Ge devices that exploit a reduced bandgap for improved sensitivity to longer wavelengths. Thus, we present new generations of avalanche photodiodes (APDs) and Geiger mode APDs (GAPDs), also known as single-photon avalanche diodes (SPADs) for red and near-infrared range operation.

SPADs are APDs biased above breakdown, where optical gain is virtually infinite, and are thus capable of capturing single photons, provided a quenching and recharge mechanism exists to avoid destruction of the device. While Si SPADs have been studied extensively, we felt that Ge APDs and SPADs still need further study. One of the major challenges of Ge SPADs is the need for a Ge substrate and the need for a dedicated process. In this thesis we explore an alternative method, where a conventional CMOS process is used as a substrate, on top of which Ge is grafted. The Ge-Si lattice mismatch generally results in high dark currents. For this reason, we decided to collaborate with an expert in Ge-on-Si growth, and as a result we could improve the quality of Ge-on-Si photodetectors and demonstrate operation in avalanche and Geiger mode with reasonable noise and sensitivity performance.

This chapter starts with the general aspects of IrSens project that kicked off our research activity on Ge sensors and the contribution of this thesis to this project. The basics of photodiodes are explained in the second section. It is followed by the challenges of Si and Ge APD/SPAD technology. Finally, the contributions and organization of this thesis are discussed.

1.1 Integrated sensing platform for gas and liquid (IrSens)

In the Nano-Tera project IrSens, a technology platform for optical chemical sensing was sought. The platform consists of the optical semiconductor source (QCL and VCSEL), gas and liquid assay preparation units, photodetectors, and signal processing. Also, the realization of a prototype demonstrator has been performed in collaboration with the University of Applied Sciences FHNW on two key medical applications. This thesis is dedicated to the photodiodes of the platform used for photodetection in visible and near-infrared wavelengths. The general view of the IrSens project is depicted in Figure 1.1.

Sensors for detecting gases and liquids have seen in the last 10 years an impressive progress boosted by a large number of applications. Strong demand in very sensitive, portable, and selective gas detectors resulted from increasing concerns about atmospheric pollutants responsible for global warming or connected to pulmonary diseases. Compact portable devices able to analyze the chemical composition of small quantities of fluids in short time delays will have an important role in medical, safety and bio-chemical sensing. For this purpose, national research programs such as the DARPA Center for Optofluidic Integration and the NSF Center MIRTHE for mid-IR sensing have been launched in the US in order to establish a strategic position in this field.

Up to now, and based on this strong demand, many compact sensors, mostly for gases, have been developed and several of them are now on the market. One big family of sensors is based

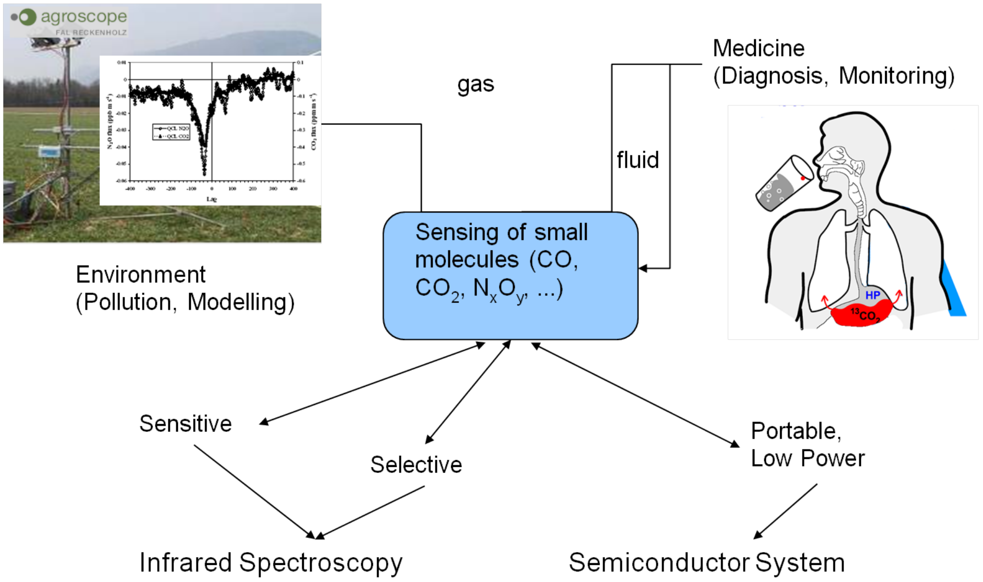

Figure 1.1: General view of IrSens requirements.

on micro machined devices (MEMS sensors) capable of measuring a physical signature of the probed gas, typically the thermal conductivity in the case of CO_2 or NO_2. Another concept, also based on semiconductor technology, is employing the effect of adsorbed gases on the electrical transport on a surface layer. In general, these devices are relatively cheap but suffer from a poor sensitivity (hundreds of ppm). They are therefore confined to the detection of high concentrations of relatively harmless gases.

Techniques based on *optical absorption*, on the other hand, offer the possibility to realize a non-invasive and highly sensitive detection platform for both gases and analytes dissolved in liquids. With this technique it is possible to probe the vibrational frequencies of the targeted molecules, most of which are located in the near and mid-infrared range, and to obtain an unambiguous signature of the investigated gas or liquid. Although the general principles of chemical sensing deploying optical methods are well known in chemistry, recent developments will lead to a real breakthrough in this technology. Whereas traditional optical techniques rely on the use of large instruments such as Fourier Transform Infrared spectrometers (FTIR) that are bulky, expensive and power consuming, we are now at the verge of a new generation of instruments that combine high sensitivity with a greatly reduced footprint, power consumption and price.

Progress in the telecommunication industry now enables the fabrication of semiconductor optical sources with very high performance in terms of power and precision, and low consumption at low cost. Compared to the traditional edge emitter, VCSELs enable a further reduction of power consumption and improved single mode tunability. Such lasers are already used commercially in O_2 sensors. The invention of the quantum cascade laser (QCL), as well as recent improvements in its room temperature performance, allow the generation of single mode emission at room temperature across the whole fingerprint region relevant for chemical sensing. Single mode QCLs operating in continuous wave (CW) with power dissipation below 2 Watt have been recently demonstrated and are now commercially available.

Another important aspect of sensors is the interaction cell, in which absorption of the analyte is probed at the relevant optical frequency. For liquid sensing, the combination of photonic bandgap structures with microfluidic channels fabricated in Silicon technology leads to the fabrication of very compact devices with good sensitivity for very small analyte volumes. New gas cell geometries with highly folded paths enable ultrahigh sensitivity measurement in small volumes of gas. In addition, optical sensing using the gas phase has the great advantage of being sufficiently selective to enable isotopic selectivity with high accuracy. This capability is definitely out of reach for chemical-based interactions of the competing sensor technologies.

The first sensor variant proposed by irSens deals with breath analysis. QCL absorption spectroscopy (QCLAS) can be used to detect helicobacter pylori by means of isotopic ratio measurements in exhaled CO_2. Helicobacter pylori have been linked to over 80% of gastric ulcers with an infection rate of around 25% in Western Europe. The infection can be detected based on an increase of $^{13}CO_2$ following ingestion of $^{13}C-labeled$ urea.

The second sensor variant deals with fluids, primarily bodily fluids that are forced into a micro-fluidic channel, where the analyte of interest is immersed in a cavity, in which QCLAS is performed. This platform is intended mainly for biomedical applications with an emphasis on drugs and doping agent detection, taking advantage of a high sensitivity performance together with the very small volume of specimen needed for the analysis. A first targeted demonstrative application for this sensor would be the cocaine detection in human saliva.

The irSens platform for both bodily fluids (human saliva) and gases (breath analysis), along with its components, is described pictorially in Figure 1.2.

1.1.1 Detection and signal analysis

Photodiodes sensitive to a wide range of wavelengths have been studied, implemented, and tested. The detectors proposed in IrSens are based on three complementary technologies: 1) bolometers for MIR, 2) InP based quantum cascade intersubband detectors (QCDs) for narrow bands in the 4-6 μm range, and 3) silicon/germanium Geiger mode avalanche photodiodes for UV-Visible-NIR [2–4].

The third technology is the focus of this thesis. Geiger mode avalanche photodetectors, has been known for decades [5]. Until recently, the devices of choice in many applications requiring high sensitivity and time resolution have been photomultiplier tubes (PMTs) and multi- or micro-channel plates (MCPs). The potential of these devices as single-photon detectors has been exploited for some time. Solid-state avalanche photodiodes (APDs) have appeared relatively recently but they have soon started competing with PMTs and MCPs directly. With the introduction of Geiger mode APDs, implemented in planar processes [6] and of single-photon avalanche diodes (SPADs) implemented in standard CMOS processes [7],

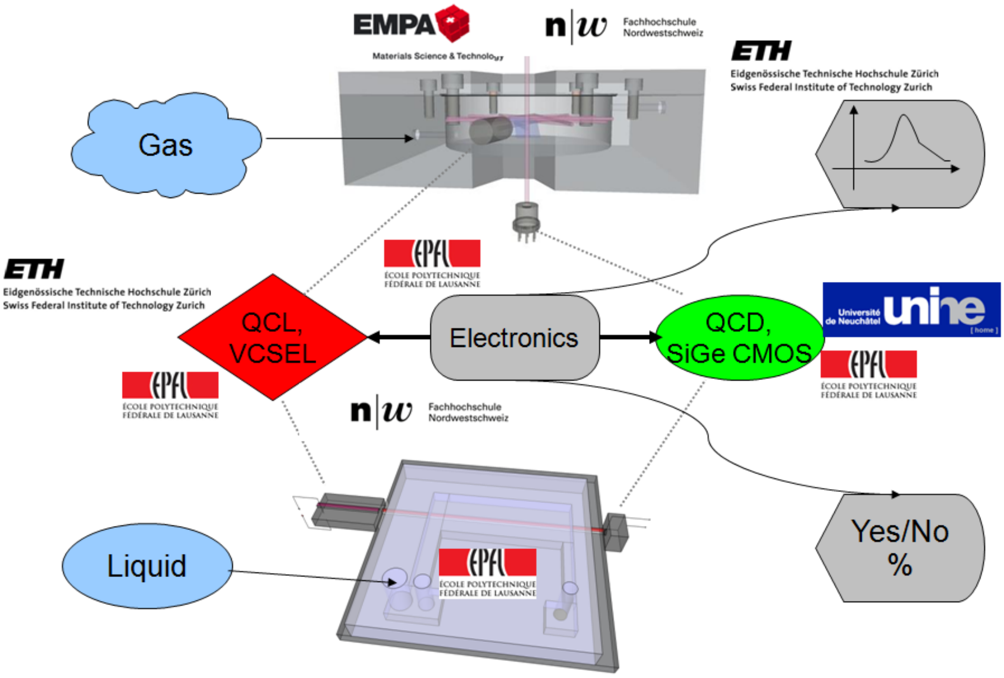

Figure 1.2: Schematic drawing of IrSens project.

this trend has further accelerated. The goal of the project was building a highly miniaturized, low-cost platform for wide bandwidth. Thus, ancillary electronics must be highly adaptable, reconfigurable, and high-performance to support our three sensing technologies. Novel hardware and software were developed to interpret spectral measurements and to quickly and efficiently determine certain spectral absorptions and signatures. Specific detection algorithms and calibration mechanisms were developed as embedded processing units in separate hardware that can ultimately be implemented in a low cost ASIC.

1.1.2 Optical sensor for human breath analysis

Analyzing compounds in breath for clinical diagnosis and therapeutic management is a burgeoning field with great potential. Breath analysis may in time be incorporated into routine clinical care as blood tests are used today for disease screening, diagnosis, prognosis, activity (inflammatory status) and response to therapy. Prominent substances of interest are NO, CO, NH_3 and $HCHO$, acetone, ethane, pentane and COS [8, 9].

More specifically, the metabolism of stable isotope marked compounds can be used for diagnostic purposes [10, 11]. The most prominent application of stable isotopes is the ^{13}C-urea breath test, which detects a Helicobacter pylori infection of the stomach. H. pylori cause more than 90% of duodenal ulcers and up to 80% of gastric ulcers. In Western Europe, infection rates are around 25%. In most individuals H. pylori infection is asymptomatic; however, about 10-15% of infected individuals will some time experience peptic ulcer disease. The ^{13}C-urea breath test for H. pylori is based on the absence of urease in the healthy human gastrointestinal tract. Urea ingested orally by a healthy human is therefore excreted unmodified. H. pylori, however, has a high urease activity, and converts urea $(CO(NH_2)_2)$ into HCO_3 and NH_4. The HCO_3 finds its way through the blood stream to the lungs and is exhaled as CO_2. Hence, individuals harboring H. pylori will exhibit an increase in $^{13}CO_2$ in their breath following ingestion of $^{13}C - labeled$ urea. Results are reported as the difference over baseline (DOB) value which is recorded before the treatment. The demand on the $\delta^{13}CO_2$ ratio measurement is that the instrument has a precision better than 1% for CO_2 concentrations of a few percent [12].

A compact and portable optical sensor based on quantum cascade lasers was developed for various components in human breath. This sensor shall be quite universal through slight modifications mainly in laser wavelength and optical path length of the measurement cell. As a first demonstrator we concentrate on the detection of the isotopic ratio $\delta^{13}CO_2$. This parameter has a very wide application, and is especially suited for MIR laser spectroscopy.

The core part of this sensor is an optical cell with a total length of about 10 cm. The cell is combined with a continuous wave, room temperature distributed feedback (DFB) single-mode quantum cascade laser operating at 4.3 μm. The divergent light from the QCL will be focused using a fast optical module. The cell is equipped with the bolometer light detection. While bolometers give very universal broadband detection, QCDs have the inherent advantage to react solely to photons in a narrow energy range. This feature is especially important for the mid-infrared wavelength range, where the blackbody background radiation of the environment creates a background noise signal in the detector.

1.1.3 Optical sensor for liquids

Chemical sensors in liquid environment based on optical absorption have been subject of wide interest for over 10 years. This family of sensors encompasses a large variety of techniques including - for instance - direct absorption infrared spectroscopy, attenuated total reflection measurements and evanescent field based probes. Although many of these techniques offer a very high sensitivity, if compared to thermal or electrochemical sensors, the main inconvenience comes mostly from the large dimension of the optical setup needed for high sensitivity and high spectral resolution measurements. This main drawback prevents having a compact portable device to be used for medical diagnostic or environmental monitoring.

The recent advent of semiconductor mid-infrared laser sources, such as the Quantum Cascade Lasers, paves the way to the realization of a new family of low-cost compact optical sensors. The aim of this work is to couple these novel laser sources with silicon based optical module taking advantage of the high transparency window of this material in most of the mid-infrared electromagnetic spectrum. The targeted sensor presents a large array of single mode QCLs closely spaced in frequency and individually addressed in order to mimic a quasi-continuously tunable broadband MIR laser source. The laser beams will be coupled into a multi waveguides silicon module in order to interact with the liquid sample delivered with a microfluidic channel fully integrated in the optical chip.

1.2 Basics of photodetection

Photodetection and light emission in semiconductors are two interesting application areas, which are working on the general principle of the creation or recombination of electron-hole pairs when exposed to light [13]. Photons with energy greater than or equal to a semiconductor bandgap can promote electrons from the valence band into excited states in the conduction band if they are absorbed by the semiconductor material. These electrons, similarly to free electrons, are able to produce electrical currents in the crystal structure under the presence of an electric field. Photo detectors are divided into two major categories:

1) Photoconductors 2) Photovoltaics

While a photoconductor is a simple layer of semiconductor whose resistivity changes in the presence of light, photovoltaic photodetectors produce current or voltage at their output. One of the most common types of Photovoltaic devices are photodiodes; the main device in this thesis. A pn diode can be used to realize a photodetector of the photovoltaic type.

The semiconductor photodiodes are made from various materials such as Si, Ge, InGaAs, InP, GaAs. Each material has a specific bandgap energy (E_g) that determines the photon absorption capability. The bandgap energy should be smaller than the photon energy ($E = h\nu$) in the detection range ($E_g < h\nu$). Thus, materials with smaller bandgaps can absorb longer wavelengths. Equation (1.1) shows the relation between E_g and cut-off wavelength (λ_C).

$$\lambda_C = \frac{(1.24 \times 10^3 (nm))}{(E_g(eV)} \tag{1.1}$$

The other main important parameter in semiconductor materials is the absorption coefficient. In fact, the Quantum Efficiency (QE) of the detector measures the efficiency of incident photon absorption to generate electron-hole pairs and create photocurrent. QE depends on the wavelength, and therefore, the absorption coefficient of the semiconductor should be sufficiently high in the detection range to have high quantum efficiency. Absorption coefficient (α) as a function of wavelength is shown in Figure 1.3 [14, 15]. As a consequence of the cut-off wavelength, while direct bandgap semiconductor materials (such as GaAs and InP) have a sharp edge in their absorption coefficient, the indirect bandgap materials (such as Si and Ge) have a long tail.

The penetration depth is related to the reverse of absorption coefficient. If the semiconductor thickness is smaller than the penetration depth, not all the photons can be absorbed, resulting in low QE. For example, in Si the penetration depth is 10 μm and 1 μm for 800 nm (infrared wavelength) and 550 nm, respectively. Thus, to have a good QE in the infrared range, the

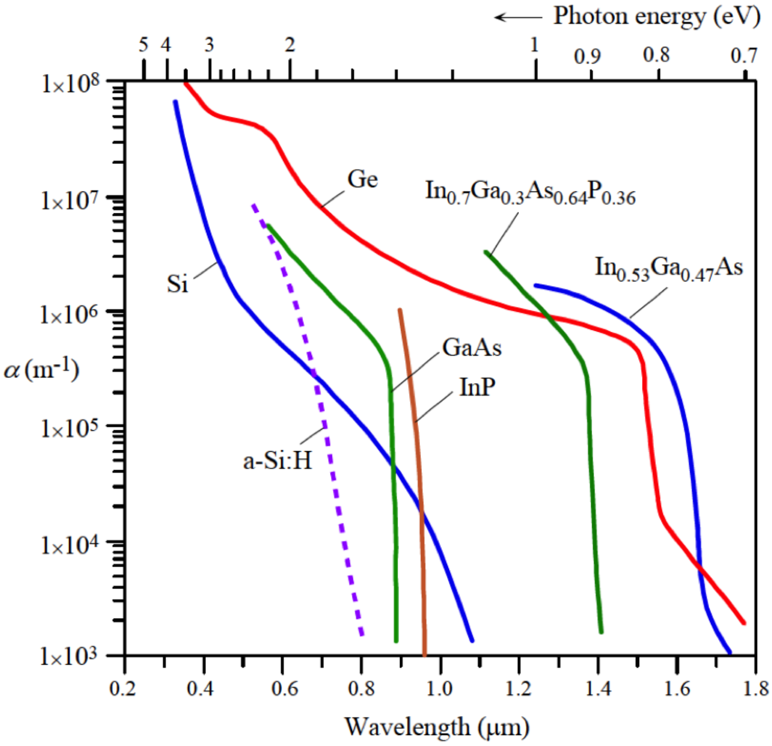

Figure 1.3: Absorption coefficient versus wavelength for semiconductor materials [14].

absorption layer should be thicker. Table 1.1 summarizes some parameters for some photonic materials.

Table 1.1: Some photonic parameters.

Material	Bandgap	$E_g[eV]$	$\lambda_c[nm]$	Sensitivity Range
Si	Indirect	1.12	1100	Visible
Ge	Indirect	0.66	1800	Near-Infrared
GaAs	Direct	1.42	875	Visible
InGaAs	Direct	0.75	1700	Near-Infrared

1.2.1 p-i-n photodiode

A photodiode is formed by joining n and p type semiconductor materials across which a built-in potential, V_{bi}, is generated due to the diffusion of carriers across the junction. Therefore, already with zero biasing across the junction an electric field is formed. The V_{bi} depends on the bandgap of its material and can be seen as the knee voltage in the linear I-V characteristics. A silicon p-n junction has the knee around 0.7 V whereas in germanium it is 0.3 V. Increasing the bandgap leads to higher built-in potential. The initial diffusion of charge carriers depletes the mobile carriers around the junction and the built-in potential that is created prevents further flow of charge. The width of the depleted region, (W), is given by Equation (1.2) [16].

$$W = \sqrt{\frac{2\varepsilon_s(N_A + N_D)}{q(N_A N_D)}(V_{bi} - V)} \tag{1.2}$$

In Equation (1.2), N_A and N_D stand for impurity concentrations of the p and n regions, respectively; q is the electron charge; V_{bi} is the built-in potential, ε_s is the semiconductor permittivity, and V is the applied bias (negative for reverse-bias operation). From Equation (1.2) it follows that the depletion width (W) increases under reverse bias. Increasing W causes a decrease in the capacitance of the photodiode ($C = \epsilon_s A/W$). A p-n photodiode is similar to a parallel plate capacitor, where the p-type anode and the n-type cathode are the two plates and the depletion width (W) is the separating medium.

A p-i-n (PIN) photodiode is a p-n junction with an intrinsic (i) layer, which is a very lightly doped p- or n- layer, between the more heavily doped layers. The energy band diagram of this structure is shown in Figure 1.4 together with the mechanisms that govern the generation of a photocurrent. The PIN photodiode is operated in the reverse-bias mode, and because of the i-region with low concentration of free carriers, it can be depleted by a low voltage. Therefore, the depletion region can extend through the entire i-region. When photons with energy greater than or equal to E_g are incident on the photodiode, electron-hole pairs are generated. Electron-hole pairs can be generated in 3 possible regions. For carriers generated within depletion region the electrons and holes quickly drift in opposite directions under the influence of the strong electric field, thus generating a reverse photocurrent. The electric field in the depletion region can be so high that the carriers travel at saturation velocities [17].

The carriers generated near the depletion region only experience a low electric field but enter the depletion region by random diffusion, thus contributing to the reverse photocurrent. Finally, the carriers generated away from the depletion region that do not reach the depletion region by diffusion will wander until they recombine without contributing to the photocurrent.

A p-i-n photodiode must have high sensitivity and low noise for various applications ranging from optical communications (III-V compound semiconductors) to infrared sensing (Si, Ge, III-V, and II-VI compound semiconductors). The dark current is often the parameter that needs to be reduced to obtain better performance of the devices. The three major components of the dark current are diffusion current, generation-recombination current, and tunneling current [16].

The diffusion current is formed by electron-hole pairs generated near the depletion region by the ambient temperature. They are diffused into the depletion region. This carrier generation is temperature dependent as given by Equation (1.3), where E_g is the bandgap of the photodiode material, k is Boltzmann's constant, and T is the ambient temperature in degrees Kelvin. From this equation it follows that the diffusion current is higher in low-bandgap material.

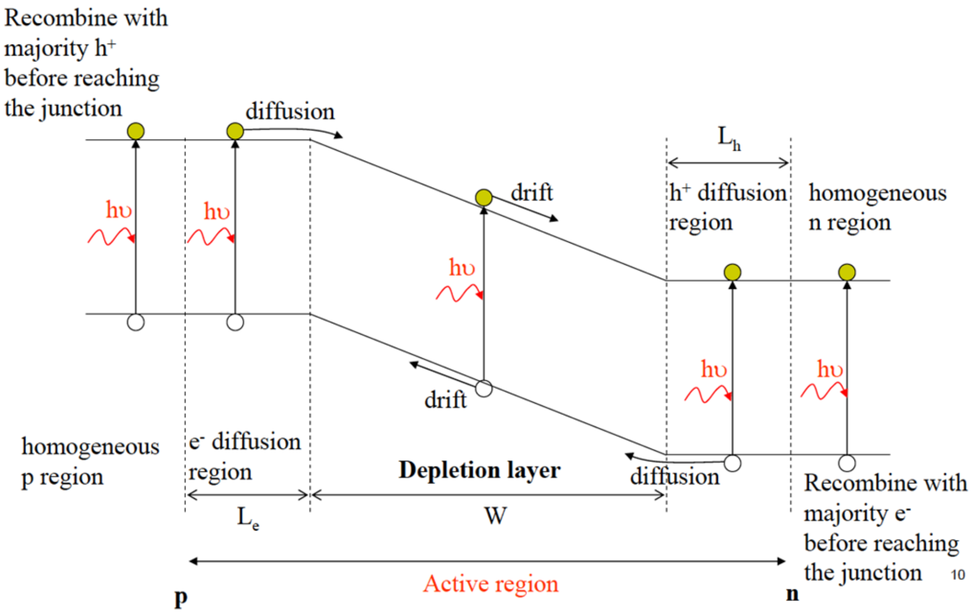

Figure 1.4: Energy band diagram of PIN photodiode [17] with the mechanisms governing the photon-generated photocurrent shown schematically.

For example, Ge (E_g=0.66 eV) has far higher diffusion current than silicon (E_g=1.12 eV). To decrease this current, the device must be cooled.

$$I_{diff} \propto e^{-E_g/kT} \tag{1.3}$$

If impurity trap levels are present within the bandgap they can be filled from the valence band or trapped carriers can be raised to the conduction band, processes that required less energy than needed to excite carrier from the valence band to the conduction band. The current generated by impurity traps in the depletion region is called the generation-recombination current, known as “trap-assisted” current, and is given by Equation (1.4).

$$I_(g-r) \propto \sqrt{(V_{bi}-V)}e^{-E_g/2kT} \tag{1.4}$$

From Equation (1.2), the depletion width (W) is proportional to the square root $(V_{bi}-V)$. Thus, Equation (1.4) can be rewritten as Equation (1.5).

$$I_{g-r} \propto We^{-E_g/2kT} \tag{1.5}$$

While the generation-recombination current is proportional to the volume of the depletion width, and is reverse-bias-dependent, the diffusion current is bias-independent. For high-bandgap semiconductors with a bandgap above 1.0 eV (for example, silicon), the generation-recombination current usually dominates over the diffusion current at room temperature.

A tunneling current is produced when the electric field in a reverse-biased p-n junction exceeds a critical field ($\sim 10^5$ V/cm) and a valence band electron can jump to the conduction band due to the quantum mechanical effect [18]. This current, called tunneling, occurs at high field and with geometrically narrow energy barriers. The tunneling current is expressed by Equation (1.6).

$$I_{tunneling} \propto EVexp(\frac{-\theta\sqrt{m}}{E}E_g^{3/2}) \tag{1.6}$$

where E is the applied electric field, m is the effective mass of an electron, and θ is a constant that depends on the tunneling barrier height. Higher doping levels on both sides of the p-n junction cause a narrower depletion width which leads to higher electric fields. As a result, the tunneling current increases. Low-bandgap photodiodes are prone to much more tunneling than higher-bandgap diodes. The tunneling current shows a weak dependence on temperature through the temperature dependence of the bandgap. This results in decreasing breakdown voltage with increasing temperature as opposed to breakdown due to the avalanche effect that increases with temperature [16].

1.3 Challenges in building APD/SPAD

When a photodiode is strongly reverse-biased until the resulting electric field across the junction exceeds the critical value, i.e. sufficient for a sustained avalanche by impact ionization, it is known as avalanche photodiode. If a photon is absorbed in the device, it generates an electron-hole pair. The impact ionization causes the electron to ionize an atom generating another electron-hole pair and so on. The energy required for an electron to ionize an atom is supplied by relaxing the kinetic energy of the electron in a high electric field [19].

The capability of an electron or a hole to trigger ionization is quantified by ionization coefficient, α_e (or just α) for electrons and α_h (or β) for holes. α_e and α_h increase with electric field and decrease with temperature. The increase of the ionization coefficient by electric field is because of electron acceleration. Increasing the temperature increases the frequency of collision which in turn decreases the probability of gaining enough energy by a carrier to cause ionization.

The internal gain (M), also known as avalanche gain, of an APD is described as the number of generated carriers for a single detected photon [20]. The optimum value of M is the ratio α/β.

the avalanche gain increasing is achievable by increasing the multiplication region. However, multiplication region widening results in decreasing the response bandwidth and increasing the noise level. This mechanism is the reason why linear APDs have the maximum gain of α/β [21].

By further increasing the bias voltage above breakdown, the gain becomes virtually infinite: this is known as Geiger mode of operation. The devices with the capability of operating in this mode are called GAPDs or SPADs. In this case a single electron can start the avalanche process until an external circuit quenches the avalanche current, thereby preventing the destruction of the device. Upon happening of an avalanche event by a free carrier, a spike of current is generated. More details about APD and SPAD structures are found in Chapter 2.

1.3.1 Silicon SPADs

Silicon is considered the best material for avalanche photodiodes among other bulk semiconductors because of its favorable ionization coefficient ratio [22, 23]. Furthermore, when compared to other semiconductors silicon has a very low temperature dependence of the avalanche breakdown [22]. Various silicon photodetectors have been widely used for visible light applications; however they suffer from low absorption capability in the near-Infrared wavelength range (above 700 nm). Chapter 2 describes the design we adopted for Si SPADs to widen the sensitivity to 800 nm, and Ge-on-Si APD and SPAD to go beyond this wavelength.

One of the challenges in Si SPAD, and generally in all kind of SPADs, is improving the timing resolution of single detectors without impairing the other device characteristics such as photon detection efficiency and dark count rate. Another challenge in SPAD devices is the increased dark counts when reducing feature size, as it happens in MOS scaling. Scaling to lower feature sizes results in reduction of voltages, currents, lateral and vertical dimensions, but increases doping concentrations in most implants. Additionally, the fabrication processes reduce the strength and duration of annealing. The absence of effective annealing increases the concentration of impurities that introduce carrier recombination-generation and trapping centers. Therefore, it increases the trapping centers resulting higher dark count rate due to both thermally generated free carriers and trap-assisted tunneling. Another challenge is to obtain the same performance of a single device in (large) SPAD arrays [24].

1.3.2 Germanium SPADs

Current research activity focused on Germanium has proposed this material for detection of photons in the wavelength range of 600-1550 nm thanks to the reduced bandgap (E_g=0.66 eV) [22, 25–27]. Ge has also been proposed because it could be used in standard CMOS processes [25], provided that the 4% lattice mismatch between Ge and Si is dealt with appropriately [22, 25]. Ge also has higher mobility than Si ($\mu_n = 0.39$ and $\mu_p = 0.19$ $m^2V^{-1}s^{-1}$ compared to $\mu_n = 0.15$ and $\mu_p = 0.045$ $m^2V^{-1}s^{-1}$), and its lattice constant matches with some of the III-V semiconductors such as GaAs. See Figure 1.5.

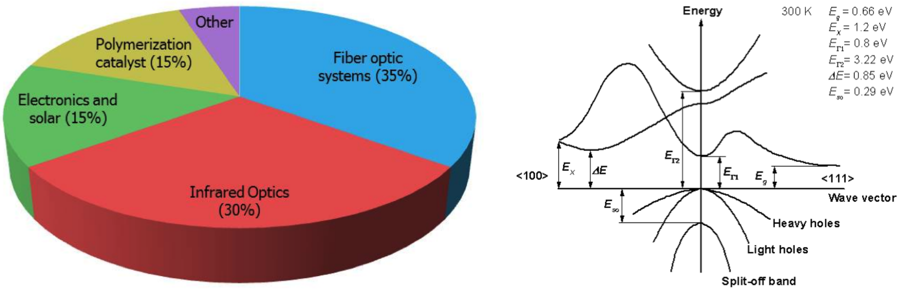

Figure 1.5: Germanium utilization [28] presentation.

However, Germanium has some disadvantages. Ge substrate production is limited by its sources. In 1998 Si could be bought for less than 10$ per kg while the price of 1 kg of Ge was almost 800$. Germanium oxide is unstable and has CMOS compatibility problem. There are some technological problems for growing Ge on Si such as the lattice mismatch between these two materials and lack of good germanium oxide. The lattice constant of Ge (5.43Å) and Si (5.65Å) shows 4.2% lattice mismatch (Figure 1.6) which can result in a bad contact between Si and Ge.

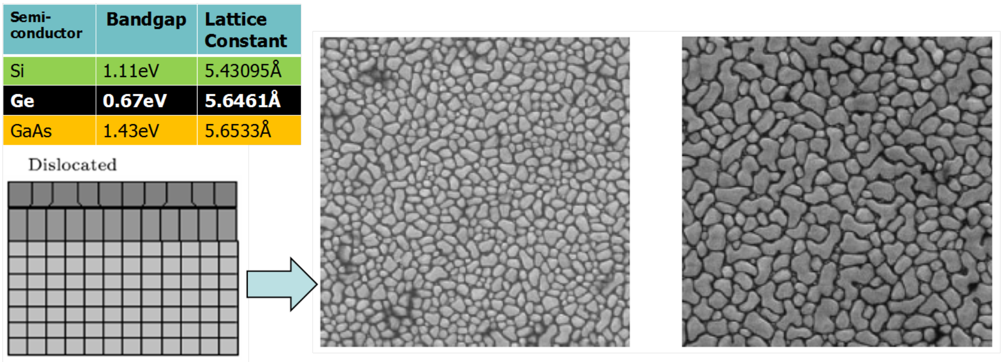

Semi-conductor	Bandgap	Lattice Constant
Si	1.11eV	5.43095Å
Ge	**0.67eV**	**5.6461Å**
GaAs	1.43eV	5.6533Å

Figure 1.6: Lattice mismatch between Germanium and Silicon [29].

1.4 State-of-the-art in Si and Ge Photodiodes

As this thesis is focused on the fabrication of visible and near-infrared APD and SPAD devices, a state-of-the-art is given in the following sections. Specific details on SPADs and their design are explained in the following chapters.

1.4.1 Si/Ge photodetectors

In [30], a high-speed resonant cavity enhanced Germanium Schottky photodetector on a silicon-on-insulator (SOI) substrate was designed and fabricated. Because bulk Ge is still a relatively weak absorbing material in the 1550 nm wavelength, as compared to some other semiconductors such as InGaAs, a thick Ge active region was needed to achieve sufficient quantum efficiency (QE); this results in a large area where drift dominates and thus the response time is slow. To decrease this side effect, the absorption region was placed within a Fabry-Perot, or a resonant cavity (Figure 1.7). In the structure proposed in [30], a Ge layer was heteroepitaxially grown on a double side SOI substrate through a low-temperature Ge buffer layer technique. This back-illuminated Ge-SOI photodetector exhibited 3-dB bandwidth of more than 12 GHz at 3V reverse bias, a peak of QE of 59%, and responsivity of 0.73 A/W for 1540 nm wavelength. This device has several drawbacks such as non-planarity and no CMOS compatibility).

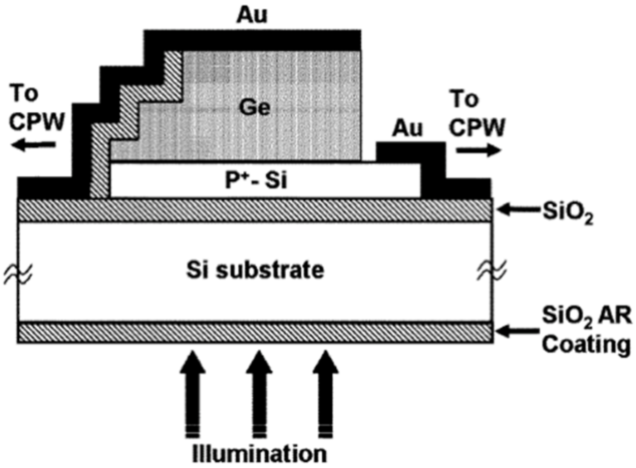

Figure 1.7: Cross-section view of the back-illuminated Ge-SOI Schottkey photodetector [30].

In [31] a vertical incidence SiGe p-i-n photodetector structure integrated on Si was proposed. Due to a 4% lattice mis-match between Ge and Si, a virtual substrate was used to correct this problem. To achieve very sharp doping profiles, the Ge p-i-n photodetector layer sequence was grown with Molecular Beam Epitaxy (*MBE*). The schematic cross-section of this structure is shown in Figure 1.8. This Ge photodetector was realized as a mesa-type diode with diameters ranging from 10 to 80 μm. The dark current of the $10\mu m$ diameter device was 75 nA at 1 V reverse bias. Also, the 3-dB bandwidth for the 1552 nm wavelength was 25.1 GHz and 38.9 GHz for 0 V and 2 V reverse biases, respectively. Again, this device is plagued with problems such as a high dark current of 75 nA at 1 V reverse bias.

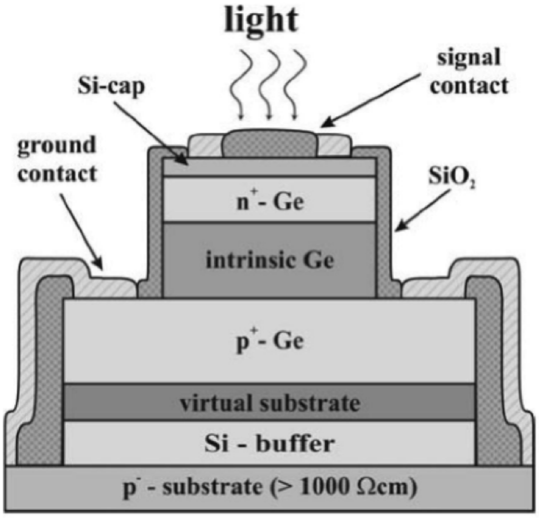

Figure 1.8: Schematic cross-section of the p-i-n Ge photodetector [31].

1.4.2 Resonant Cavity-Enhanced Schottky photodetectors

The authors of [32] proposed a resonant cavity-enhanced Schottkey photodetector based on internal photoemission effect over a Schottkey junction Au-Si, front illuminated. The resonant cavity was a Fabry-Perot vertical-to-the-surface structure which was formed by a buried reflector. This buried reflector was a Bragg mirror formed by alternating layers of different refractive indices, Si and SiO$_2$ having refractive index 3.45 and 1.45, and different thicknesses. In this design, four periods of Si/SiO$_2$ formed the bottom mirror (Figure 1.9). The QE of this method was 0.1% and theoretical 3-dB bandwidth was 100 GHz, which means 100 MHz bandwidth-efficiency product. Although Schottkey photodiodes have high switching speed, the QE of this method was very small because incident photons need to traverse across the top Schottkey metallic layer.

1.4.3 Waveguide Si/Ge photodedetectors

Two different approaches can be considered for near-infrared detectors based on SiGe: surface illuminated photodetectors and waveguide integrated photodetectors. Since 2007, several results have been reported on Ge-on-Si photodetectors integrated in Si-based waveguides [25, 26, 33, 34].

In [26], a Ge-on-Si photodetector integrated in a SOI rib waveguide was reported. The schematic view of this structure is shown in Figure 1.10. A good overlap between the guided mode in the SOI waveguide and the absorbing Ge layer was obtained by this configuration. A 3dB bandwidth of this device was measured as 42 GHz at 4 V reverse bias for a photodetector with length and width of 15 μm and 3 μm, respectively. The quantum efficiency of 80% caused the product of QE by the bandwidth to reach 33.6 GHz at 1.55μm wavelength. Also the respon-

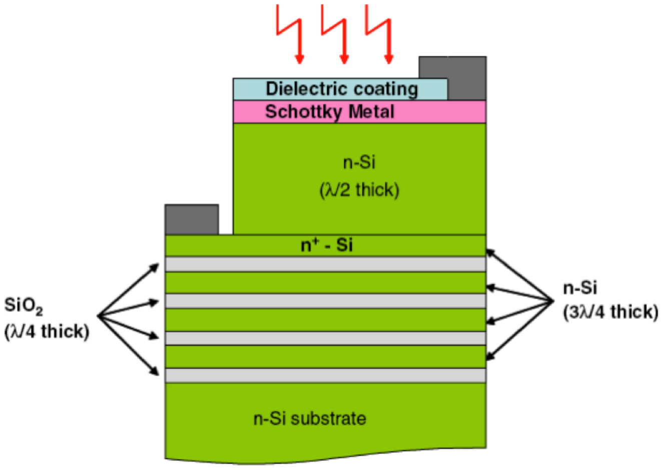

Figure 1.9: Schematic cross-section of RCE Schottky photodetector [32].

sivity was 1 A/W at the wavelength of 1.52 μm and 0.5 V reverse bias. The technology process used to fabricate this structure was fully compatible with CMOS process.

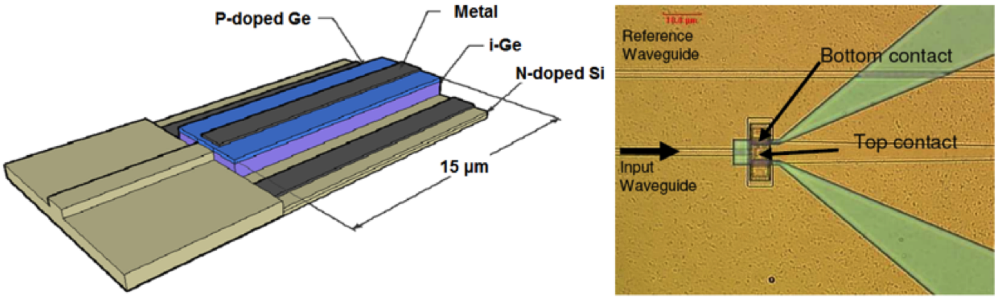

Figure 1.10: Schematic view of p-i-n Ge photodetector integrated in SOI waveguide [26].

1.4.4 Ge APDs

The authors of [34, 35] proposed mesa-type and waveguide-type SiGe APDs. This SiGe APD was based on the conventional separate absorption, charge and multiplication (SACM) APD structure. In this structure, light absorption and carrier multiplication occur inside Ge and Si, respectively. The schematic cross-section of the mesa-type and waveguide-type SiGe APD is presented in Figure 1.11 (a) and (b), respectively. Also, the dark current and photocurrent of the mesa-type device is shown in Figure 1:11 (c). The breakdown voltage, defined at a dark current of 10 μA, was close to -25 V for this device. The gain-bandwidth product for the mesa-type APD was 340 GHz for the 1300 nm wavelength. The 3dB bandwidth for the waveguide-type was measured as 23 GHz when the bias was low. At high bias, the 3dB bandwidth dropped to 8 GHz due to increase of the avalanche build-up time.

All of the above-mentioned methods propose interesting ideas to implement Si/Ge photode-

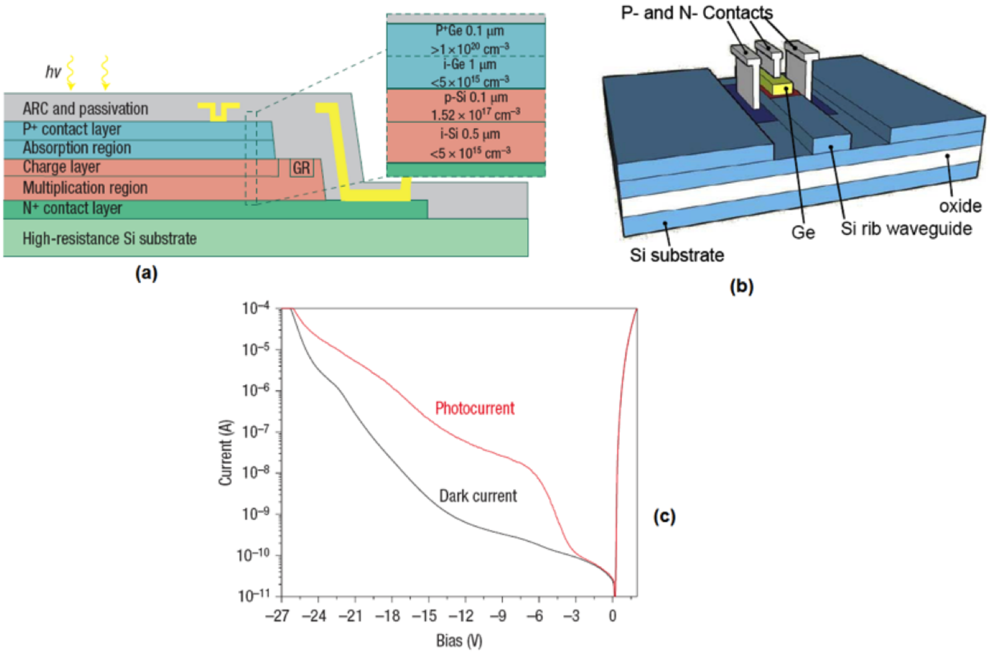

Figure 1.11: (a) Schematic view of mesa-type and (b) waveguide-type SiGe APD, (c) dark and photocurrent of the mesa type [34, 35].

tectors working in linear or proportional modes. However, the problem of these devices is their ability to work above breakdown voltage: because of the junction between Ge and Si, they are all suffering from premature breakdown voltage or edge breakdown that de facto prevents them to reach the Geiger mode, and therefore be able to work as SPADs.

1.5 Thesis contributions and organization

The work carried out during this PhD thesis addresses two main photodetector device platforms for visible and near-infrared wavelengths amenable to ultra-low temperature operation:

1. Ge-on-Si photodiodes working in APD/SPAD mode for near-infrared

2. Deep-junction single photon detector in CMOS technology for visible to deep red wavelengths

Several Ge-on-Si SPAD and APD devices as single or arrays of photodiodes have been fabricated for the first time. The main motivation is to use alternative semiconductors with standard Si technology to increase the sensitivity range. Such techniques are advantageous when special properties of a specific semiconductor are needed together with routine IC technologies such as CMOS.

The target applications for these devices are fluorescence lifetime imaging microscopy (FLIM), Raman spectroscopy, near infrared optical tomography (NIROT) for deep tissue imaging, where sensitivity to the 800nm range is critical.

The thesis is organized as follows. In the Introduction Chapter, firstly, the framework of the main project and role of this thesis is reviewed. In the second part, basics of photodetection are described. The challenges in building Si and Ge photodetectors and state-of-the-art are discussed in details.

In Chapter 2, the principles of single-photon avalanche diodes are described. The Si SPAD modeling and simulation as well as various designed structures are introduced. Moreover, the Ge-on-Si fabrication process and device design are discussed.

Chapter 3 shows the experimental results for single pixel SPADs in Si and Ge-on-Si. I-V characteristics and dark count performance are shown for SPADs. Their performance is also characterized in terms of response time jitter and photo response. Light emission test, afterpulsing distribution, and activation energy are studied for Si devices. Moreover, CV profiling is measured for the new Ge-on-Si photodiodes.

Chapter 4 focuses on different array designs for Ge-on-Si photodetectors. The design of 4×4 arrays with integrated readout circuitry and preamplifier is introduced. Different BJT and JFET transistors are used to investigate appropriate ancillary circuits for Ge-on-Si photodiodes. Furthermore, a 300×1 line array is reported as the first Ge-on-Si APD array. Various pixel designs to achieve Germanium Photomultipliers (GePM) are also fabricated and tested.

Chapter 5 is dedicated to low temperature measurements for Si and Ge-on-Si devices. Most semiconductor parameters are affected by temperature. While some parameters show only a relatively slight dependence, others may change by several orders of magnitude at very low temperature. For Si SPADs, the variations on dark count rate and breakdown voltages based on temperature are reviewed. More studies on the novel Ge-on-Si photodiodes are reported in this chapter.

Chapter 6 summarizes the main conclusions of this thesis and provides a number of recommendations for future work.

2 Visible and Near-infrared SPADs

The NIR spectral range of detection is only accessible in semiconductors with small bandgaps and high cut-off wavelengths. The cut-off wavelength in Si for light absorption at room temperature is 1100 nm [36] which means Si alone is not suitable for long wavelength detection. On the contrary, some lower-bandgap semiconductors such as Ge and InGaAs (with cut-off wavelengths at room temperature of 1800 nm for Ge and up to 2600 nm for InGaAs, depending on the Ga to In fraction) are more suitable semiconductors for detection of low-frequency NIR wavelengths. Both Ge and InGaAs are all well known and commercialized in different infrared spectral range applications [37] - [38]. However, the price range and the complexity of InGaAs as a compound semiconductor and compatibility of both Ge and InGaAs with standard Si-CMOS processing have always been the main critical issues. The integration of such materials on Si substrates are mostly achieved either by flip-chip, which is costly and leads to yield reduction, or by hetero-epitaxial growth, which usually requires extra processing steps such as Aspect-ratio trapping [39, 40] and overgrowth and planarization steps [41] to reduce the threading dislocation density.

2.1 Principles of Single Photon Avalanche Diode (SPAD)

Single-photon avalanche diodes (SPADs) implemented in CMOS technology consist of a p-n junction, biased above breakdown voltage V_{BD} so as to achieve virtually infinite optical gain. In this regime, known as Geiger mode of operation, SPADs can detect single photons. In a SPAD, upon seeding of a photon, an avalanche may be triggered followed by the classical phases of buildup, spreading, and quenching. Quenching can be achieved passively, with a ballast resistance, and actively, with a feedback circuitry. After quenching, a recharge phase is required to bring the SPAD back to the original state, thus enabling the next avalanche.

If a photon impinges the diode and is absorbed in the depletion region, the photon absorption generates a primary electron-hole pair inside the high electric field region. The critical electric field in this bias voltage forces the electron to accelerate towards the cathode and the hole towards the anode. Possibly, one of those carriers acquires enough kinetic energy to generate secondary electron-hole pairs by impact ionization (Figure 2.1). In addition, this phenomenon may occur on primary and secondary carriers, which result in a chain of impact ionizations, causing the diode's depletion capacitance to be rapidly discharged. Thus, a sharp current pulse is generated and may be easily measured [42]. This effect is commonly known as avalanche multiplication and this mode of operation is called Geiger-mode.

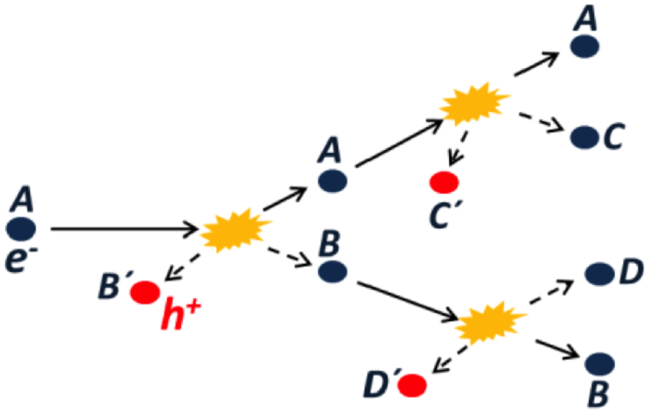

Figure 2.1: Impact ionization [13].

Typical p-n junctions used in conventional CMOS image sensors [43], are not compatible with the Geiger mode of operation, since they cannot support high voltage biasing without producing an immediate breakdown current. Most often this breakdown occurs on the edge of a junction (in a planar process), thus causing the so-called premature edge breakdown (PEB). The main reason for PEB is that the electric field is not uniform across the junction area but it is highest in the perimeter. Because of PEB, the electric field in the multiplication area cannot reach the critical value for impact ionization; this effectively reduces the fill factor to near zero. Utilizing specific avalanche photodiode structures instead of a simple p-n junction can prevent or drastically reduce PEB. Note that SPADs achieve infinite optical gain by operating above breakdown, while APDs operate at a bias slightly lower than the breakdown voltage, thereby achieving finite optical gains. This mode of operation is known as proportional and the optical gain is typically in the hundreds to a few hundred thousands.

As compared to general PIN photodetectors, APDs improve sensitivity. APDs can respond to modulated light at frequency of a few GHz, which define the application of APDs in most of simultaneous high-frequency and low-intensity light signals. Moreover, APDs are generally useful in applications where the noise of the amplifier is higher than the noise in PIN photodetectors. In this case, although the APD is noisier than the equivalent conventional PIN photodiode, improved S/N can be obtained in APD gain up to the point that the APD noise is equivalent to that of the amplifier. Applications of APDs includes, for example, optical fiber communication, spatial light transmission, general low-light-level detection, laser radar, and biomedical devices [44].

SPADs generally exhibit an exceptional timing jitter, of the order of a few tens or hundreds of picoseconds and can be enabled and disabled within less than a nanosecond. Thanks to this property, SPADs are amenable to use in fast photon counting setups required in LIDARs and 3D time-of-flight cameras [45], as well as in Raman spectroscopes, where sub-nanosecond active gates are required [46].

2.1.1 Operation

In Geiger mode, the bias voltage above V_{BD} is known as excess bias voltage and denoted as V_e or V_{ex}. Figure 2.2 shows the I-V characteristics of a diode, with its three operating regimes. The optical gain grows exponentially when approaching breakdown in proportional mode, while it becomes virtually infinite above breakdown.

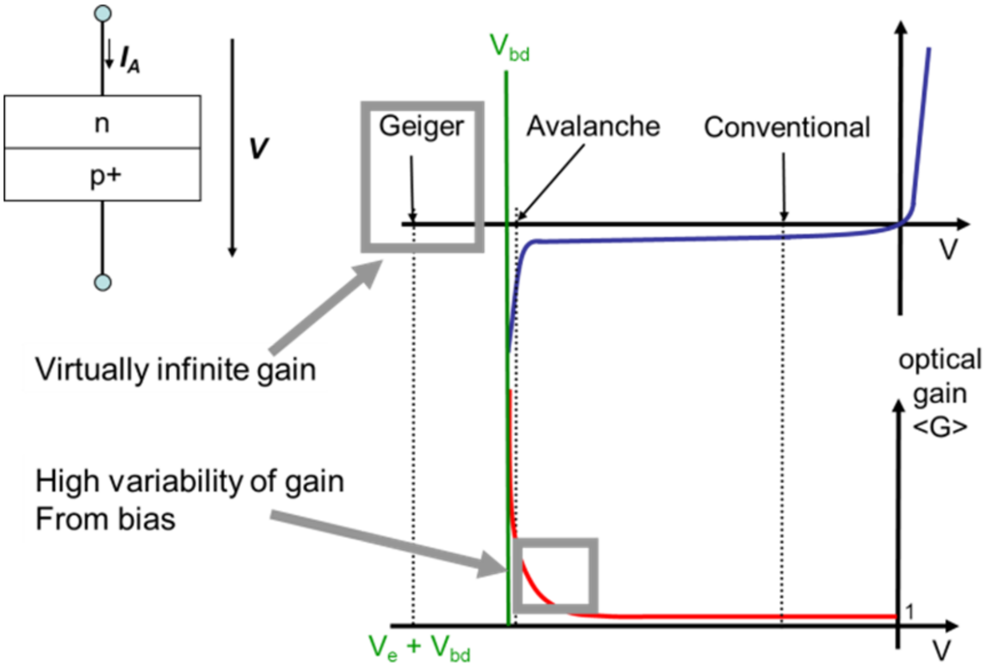

Figure 2.2: Photodiode operation modes.

The avalanche current must be quenched by a mechanism to avoid damaging the device by overheating. In general, a SPAD circuit consists of a diode, a quenching mechanism, and a recharge circuitry (Figure 2.3). A quenching mechanism can be as simple as resistor or transistor along the avalanche path as shown in Figure 2.3.

The avalanche quenching function is followed by a recharge phase that brings the SPAD to the same bias condition that it had before the Geiger event. Therefore, the SPAD recovers its single photon detection ability in a short time after each Geiger event. In this time slot (known as dead-time or DT), because the SPAD device is under a lower bias condition, it's unable to detect photons. Furthermore, a properly designed inverter (or buffer) converts the avalanche current onto a digital voltage pulse. Figure 2.4 [47] shows a PMOS transistor, which performs

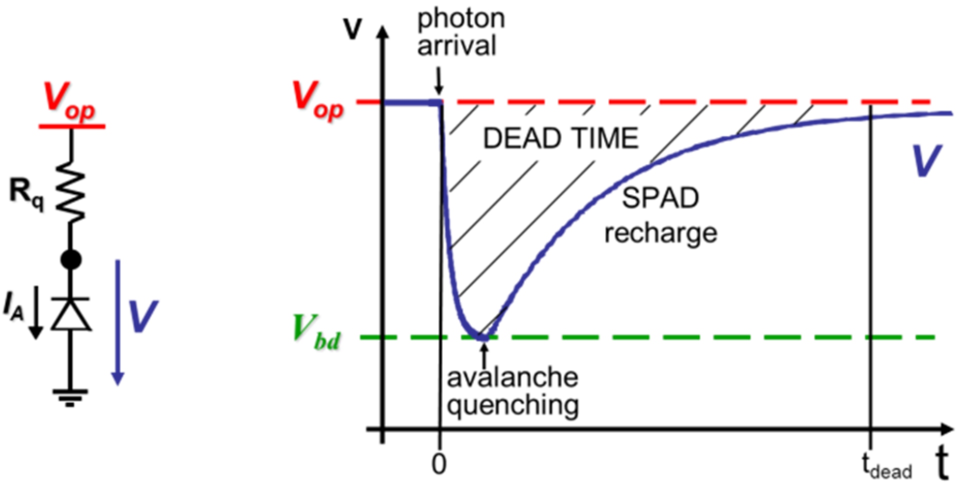

Figure 2.3: (left) passive quenching, (right) operation cycle.

quenching, and a CMOS inverter converting a Geiger pulse to digital one.

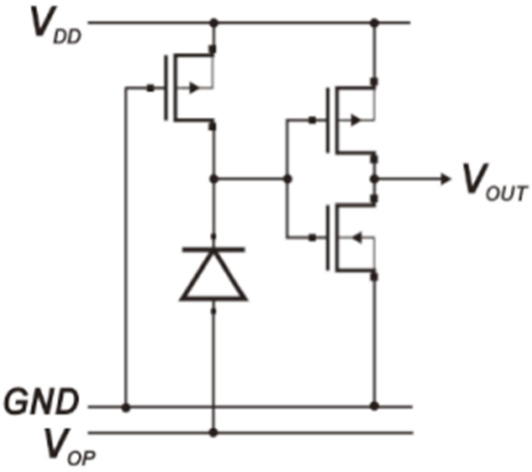

Figure 2.4: Typical CMOS SPAD schematic [47].

2.1.2 Premature edge breakdown and guard ring

Increasing the thickness of multiplication region in SPADs can increase the breakdown voltage. Whatever this layer thickness, the active region should be separated from the surrounding area. The structure responsible for this separation is known as the guard ring. The purpose of a guard ring is to either increase the breakdown voltage locally or to reduce the electric field at the edge. Both effects reduce premature edge breakdown (PEB).

Figure 2.5 depicts a cross-section of a device without guard ring that would show edge break-

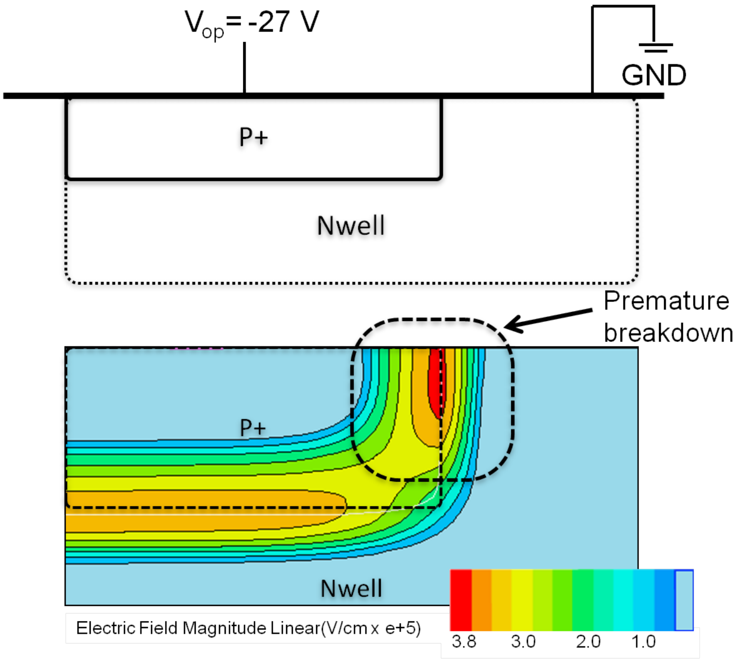

Figure 2.5: premature edge breakdown, (top) a SPAD without a guard ring; (bottom) the electric field simulation at -27 V.

down. The simulation of the electric field at the applied voltage of -27 V is in bottom of the figure. The electric field strength is much larger near the device edge than the center. Devices with premature breakdowns suffer from high noise. Thus, the guard ring requirement is a constraint in all SPAD design.

2.1.3 Dark count rate (DCR)

A SPAD should ideally produce no response in the dark. However, thermally generated or trap assisted tunneling may cause spurious counts that are indistinguishable from photon-generated counts. This noise is characterized in terms of the mean frequency of dark counts, known as dark count rate (DCR).

2.1.4 Responsivity and Quantum Efficiency (QE)

Quantum efficiency (*QE* or η) is defined as the ratio of electron-hole pairs generated for each incident photon. In a non-avalanche pin photodiode, QE is less than unity. The responsivity (R) is measured in A/W and relates the incoming optical power with the resulting photocurrent as Equation (2.1) [48].

$$i_p = RP_{in} \Longrightarrow R = \frac{i_p}{P_{in}} \tag{2.1}$$

The relation between responsivity (R) and QE (η) is shown in Equation (2.2), where i_p is the current generated by photons, q is the electron charge, h is plank constant, v is the light frequency, and λ is wavelength. The term hv stands for photon's energy.

$$\eta = \frac{number\ of\ electrons\ of\ photocurrent\ generation\ rate}{photon\ incident\ rate},$$

$$\Longrightarrow \eta = \frac{i_p/q}{P_{in}/hv} = \frac{hv}{q}R \approx \frac{1.24}{\lambda}R \tag{2.2}$$

These equations are true while photon energy is below the semiconductor bandgap ($hv < E_g$); otherwise QE will become zero since no absorption will be occurred after cut-off wavelength.

The responsivity of photodiode is limited and take a maximum value for a $QE = 1$. It means $R = \lambda/1.24$ from Equation (2.2). Though, R can be larger in APDs due to the internal gain induced by avalanching. This gain, or avalanche multiplication (M), is defined as Equation (2.3).

$$R_{APD} = MR = M\frac{\eta q}{hv}, \qquad M = \frac{I_{R1}}{I_{R0}} \tag{2.3}$$

where I_{R1} is the reverse current generated by avalanche action and I_{R0} is the unity gain current.

2.1.5 Photon Detection Probability (PDP)

The probability that a photon triggers a multiplication is known as photon detection probability (PDP). PDP is defined as the probability of successful photon detection when a photon hits the SPAD active area (Equation (2.4)).

$$PDP = \frac{photon\ count\ rate}{area\ normalized\ incident\ photon\ rate}$$

$$Photon\ count\ rate = (total\ count\ rate - DCR),$$

$$area\ normalized\ photon\ rate = \frac{P_{in} \times \lambda \times (\frac{Active\ Area}{laser\ beam\ spot\ area})}{hc} \tag{2.4}$$

In Equation (2.4), P_{in} is the incident optical power to the SPAD active area, h is Planck's constant, c the speed of light, and λ the wavelength. PDP strongly depends on photon wavelength and excess bias. Figure 2.6 shows a possible setup to measure PDP. It consists of a light source passing from wavelength selector to have a unique λ beam. The integration sphere is used to uniformy illuminate the sample while redirecting a portion of the light onto a reference diode. A neutral density filter (ndFilter) can be used to equally reduce the light intensity of all wavelengths to avoid saturation in the sample.

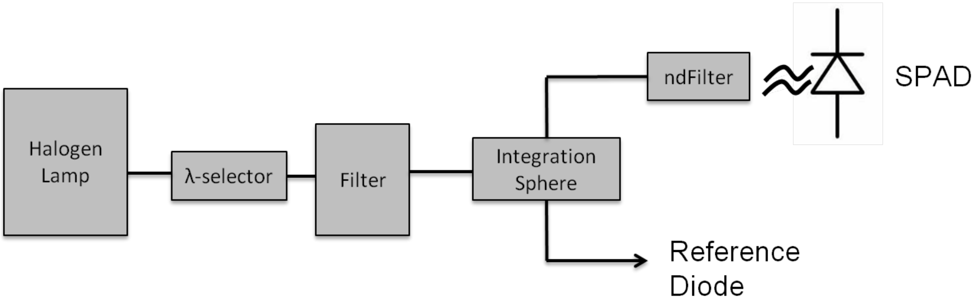

Figure 2.6: Schematic of photon detection probability setup.

2.1.6 Afterpulsing probability

During fabrication of semiconductors, some defects are added intentionally or involuntarily in the crystal due to impurities, which create generation-recombination centers with energy levels in the middle of the forbidden band. Actually, impurities may create many trapping centers having energy levels in the forbidden band ranging from the proximity of valence up to the conduction band [18].

In a SPAD when a Geiger discharge occurs, a very large number of carriers go through the junction, but some of them may be captured by trapping centers. When a captured electron or hole from a trap is reemitted in the multiplication region after dead time, there is a probability to generate another Geiger event [49, 50]. Since the latter event is correlated in time with the original Geiger discharge, it is known as afterpulse. Afterpulsing is characterized in terms of the probability of occurrence as a function of dead time, known as afterpulsing probability.

Afterpulsing probability depends on the density of deep-level trapping centers. Traps with energy levels close to edges of the forbidden bands have short lifetimes and tend to reemit carriers shortly after the capturing process. Hence, they have small contributions to afterpulsing since carriers are likely to be reemitted during dead time. On the other hand, deep-level traps tend to reemit carriers after the dead time and as a result, they typically induce afterpulses.

2.1.7 Timing jitter

Another important characteristic of SPADs is their ability to accurately detect the arrival time of photons [51]. Timing jitter or timing resolution is defined as the statistical fluctuation of the interval time between the arrival of photon and the leading edge of the output pulse. In this definition, the term resolution actually stands for the statistical spread of a SPAD response to a short light pulse. Timing resolution is normally reported as the full width at half maximum (FWHM) of the photon arrival time distribution.

In a SPAD, timing jitter usually includes two timing components: a narrow distribution and a low-amplitude tail given by one or more exponential decay components. The narrow distribution around the actual photon arrival time may be drawn by a Gaussian distribution. This distribution is mostly related to photons that are absorbed in the depletion region of SPADs. The lower limit for timing resolution is theoretically given by the carrier transit delay from the absorption point in the depletion layer up to the multiplication region, at saturation velocity, approximately 10ps per micrometer of depth [42]. Moreover, the avalanche build-up fluctuation also widens timing resolution. This component increases with ionization coefficients of electrons and holes, which successively may be enhanced by increasing the SPAD bias voltage. Consequently, to achieve higher timing resolution higher V_{ex} is desirable.

The avalanche event propagates laterally over the whole junction area. In SPADs with bigger active area, this propagation time of the avalanche is significant and it can impose higher timing fluctuations. The photon absorption location is important in this propagation. As a result, the timing resolution depends on the photon absorption location; and the SPAD's center may lead to the fastest timing response [52]. Besides, in large devices the energy involved in the breakdown discharge is high due to parasitic capacitance. This high energy may lead to hot carriers, resulting in photon emission and enhancement of the lateral propagation [53]. These photons can be absorbed at different locations in SPAD's depletion region and initiate multiple avalanches, thus accelerating the lateral propagation.

The other component of timing jitter, the slow tail typically presents in timing response of SPADs, is due to incident photons that are absorbed in quasi-neutral regions of the p-n junction [54]. In order to trigger an avalanche event in those regions, primary carriers should diffuse to the SPAD's depletion region. The distance from the origin of the carriers to the depletion region determines the mean value of tail length and the diffusion delay fluctuation. Because diffusion is a slow process, the typical timing resolution tail is orders of magnitude longer than the main narrow peak. Moreover, because the photon absorption location is statistically distributed in depth, the response tail does not exhibit a single exponential decay component. Thus, the typical tail response may only be fitted by the superposition of many exponential decay components and it will depend on the incident photon wavelength.

2.2 Si SPAD modeling and implementation in 180-nm CMOS

In general, a conventional blue or green sensitive SPAD structure is a p-type diffusion as an anode and n-type well (Nwell) or deep-Nwell (DNwell) as a cathode, as shown in Figure 2.7 (a) [55, 56]. In this structure, the p-n junction is between P^+ and Nwell/DNwell, and is generally a shallow junction much smaller than 1 μm (several 10 or 100 nm). In structures with shallow multiplication regions, PDP peaks at shorter wavelengths, with deeper multiplication regions PDP will peak at longer wavelengths [57]. Figure 2.7 (b) shows such a configuration [58]. This structure can achieve higher PDP for longer wavelengths because generated electrons in the deep junction may trigger the avalanche with high impact ionization possibilities. But this structure shows low sensitivity to blue light. Finally, Figure 2.7 (c) shows a structure with possibly wide spectral range of detection [59], in cost of higher doping of the substrate.

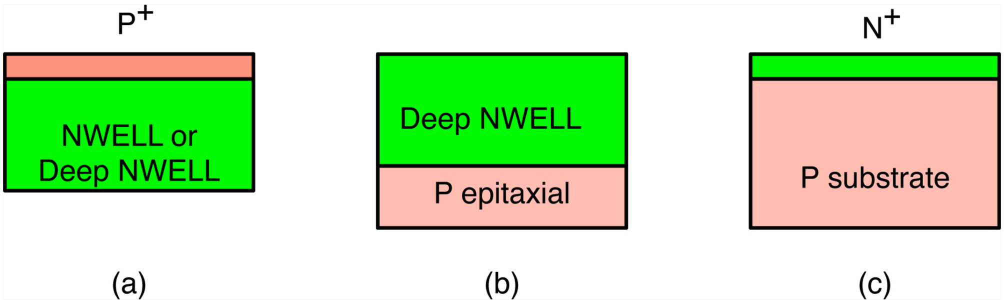

Figure 2.7: Three conventional SPAD structures [60].

This section presents some SPAD structures including an ultra-deep junction that has been designed and implemented in 180nm CMOS technology. In this analysis, device structures with promissing performance towards the integration of large SPAD arrays are described. One of the most promissing one is the ultra-deep junction SPAD optimized for red and near-infrared (NIR) sensitivities, while not sacrificing timing jitter performance.

Amongst several SPAD structures that has been designed and implemented in CMOS 180nm technology, the two best performing devices will be presented in the following sections. The former structure is a vertical photodiode, and the latter one is a deep junction photodiode.

2.2.1 Vertical junction photodiode

A vertical SPAD structure (SPAD1) is shown in Figure 2.8, where low doped N-type diffusion (N^-) and P-type diffusion (P^-) are used as a cathode and anode, respectively,with N^+ and P^+ diffusions for the cathode and anode metal contacts. N-diffusion is related to N^+ contact doping via Deep-Nwell and Nwell regions. No-well zones between P^- and Nwell makes a virtual guard ring area, therefore the multiplication area is created between N^- and P^-. The depth of P^- is larger than that of P^+, resulting in a deeper multiplication area.

In this structure, similar to Figure 2.7 (a), three regions can contribute to PDP. Electrons by absorbed photons with low-er wavelength in P^+ can diffuse to the junction area and generate an electron-hole pair; possibly triggering an avalanche event. The possibility of these events is not considerable, because of the distance between P^+ and depletion (multiplication) area at the border of P^-/N^-. Longer wavelengths close to red can be absorbed in P^- or N^- regions. Generating electrons or holes in the multiplication region may trigger an avalanche event. Also, long wavelengths in red or near-infrared may generate holes in N^-/Deep-Nwell moving toward the junction and possibly triggering an avalanche event. The latter can contribute in increased sensitivity in the red.

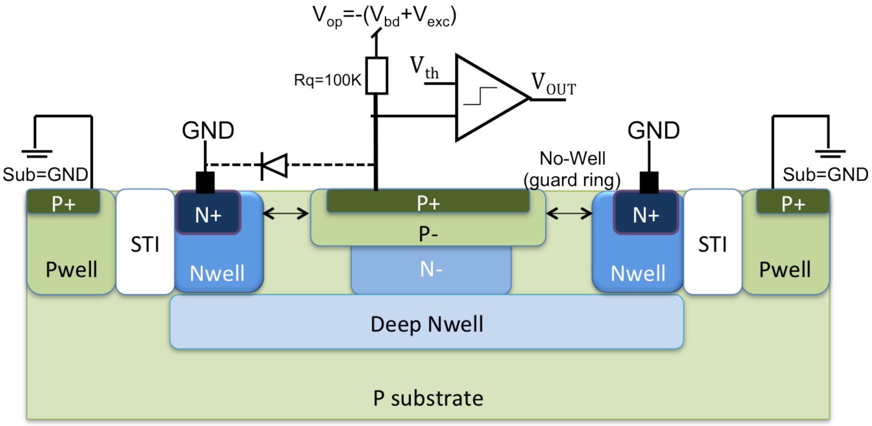

Figure 2.8: Cross-section and schematic of the 180nm vertical junction SPAD structure (SPAD1) and readout circuit.

2.2.2 Deep pn junction

The device structure for deep junction SPAD (SPAD_RED) is shown in Figure 2.9. A P-type well (pwell) and an N-type deep well (Deep-Nwell) connected to N^+ diffusion by nwell are used as anode and cathode, respectively. No-well zones between Pwell and Nwell are creating a guard ring. The multiplication area is localized in the junction between Pwell and Deep-Nwell.

The deep junction has been realized to extend the SPAD sensitivity to longer wavelengths. This structure has also three main regions that can contribute to PDP. Although the distance between P^+ and the depletion region (at the border of Pwell and Deep-Nwell) is long, electrons generated by absorbed photons in low wavelength may diffuse to the depletion area, generate an electron-hole pair, and trigger an avalanche event. This distance will definitely decrease the sensitivity in blue. Longer wavelengths can be absorbed in Pwell or Deep-Nwell regions, generating electrons or holes in the multiplication region and trigger an avalanche event

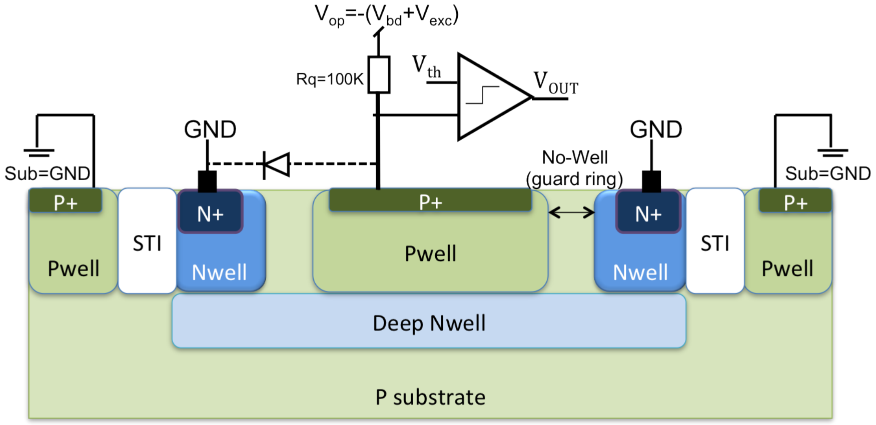

Figure 2.9: Cross-section and schematic of the 180nm deep junction SPAD structure (SPAD_RED) and readout circuit.

with higher probability. Also, long wavelengths in red or near-infrared may generate holes in Pwell/Deep-Nwell moving toward the junction and possibly trigger an avalanche event. The latter can contribute to increased sensitivity in the red.

Furthermore, the junction between Deep-Nwell and P-substrate can assist the absorption of photons around 800nm wavelength. The junction between Pwell is around 1.35 μm to 1.5 μm, while the junction with the P-substrate would be around 4 μm. However, the dimensions are still relatively small, so as to prevent too long random walks from photon detection to multiplication, and thus large jitter [51].

2.2.3 Integrated quenching circuits

To have on-chip quenching and readout circuitry, the circuit depicted in Figure 2.10 (left) has been realized. The passive quenching resistor of 100$k\Omega$ is used as a ballast resistor. The inverter converts Geiger pulses into digital ones. To be able to drive output PADs with large capacitance, appropriate cascaded buffers have been inserted between the inverter and PADs.

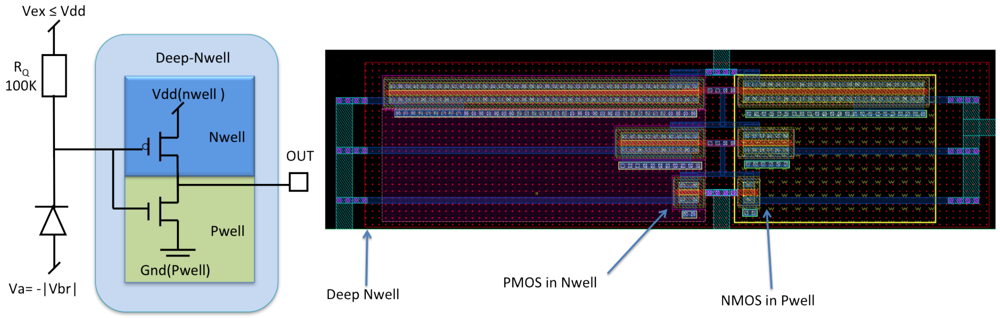

Figure 2.10: Resistor-inverter quenching, cascaded 3 inverters for driving output PAD, Inverter size of 1x, 4x, 16x.

The layout of the circuitry is shown in Figure 2:10 (right). NMOS and PMOS transistors were implemented in Pwell and Nwell, respectively. Deep-Nwell area covers all the transistors to separate them from SPAD zones. Size of transistors was multiplied by 4 to have better output current driving.

2.2.4 TCAD simulation

The device structures used in this thesis have been modeled in two device simulators: *Taurus Medici* and *Sentaurus Device* [61]. The CMOS process at the basis of the simulations was derived from process simulation steps using tools such as *Sentaurus Process* or *Taurus TSUPREM-4* or through CAD operations and *process emulation* steps.

Taurus Medici is a 2D device simulator used to model electrical, thermal and optical characteristics of semiconductor devices. This tool is useful for a wide variety of devices including MOSFETs, BJTs, HBTs, power devices, IGBTs, HEMTs, CCDs and photodetectors to be modeled; it can also be used during design to optimize devices so as to meet performance goals. Device simulation helped us quantify the electric field in the junctions, so as to identify the size and location of the multiplication region, thus illustrating the effectiveness of the guard ring to prevent PEB.

The electric field of SPAD1 is shown in Figure 2.11, where the electric field exceeds critical value for impact ionization (3×10^5 V/cm in Si) only in the multiplication region and it is below the critical value in the guard rings. The multiplication region is formed between P^+ and N^- and confines high electric fields.

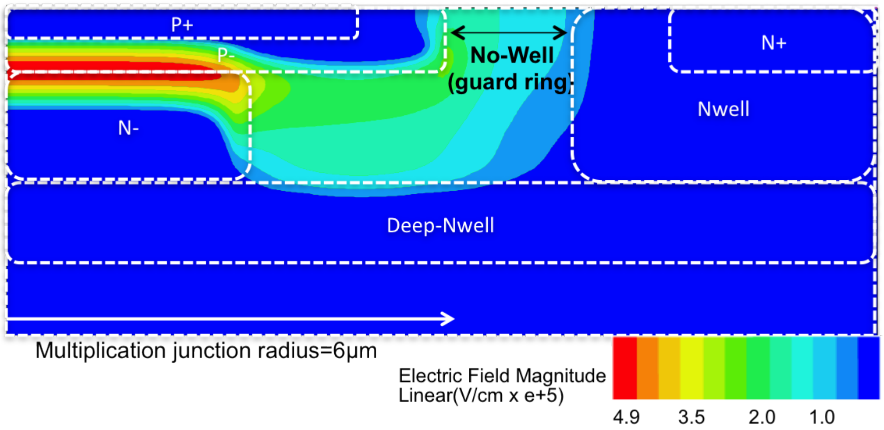

Figure 2.11: Medici simulation of electric field for 12μm active diameter SPAD1.

The electric field simulation is shown in Figure 2.12 for SPAD_RED. The multiplication region is formed between pwell and deep-nwell where high electric fields are confined. The electric field in the multiplication region exceeds critical value for impact ionization in Si. The effect of No-well zones as guard rings is also illustrated. Lower electric field in these regions prevents PEB effectively.

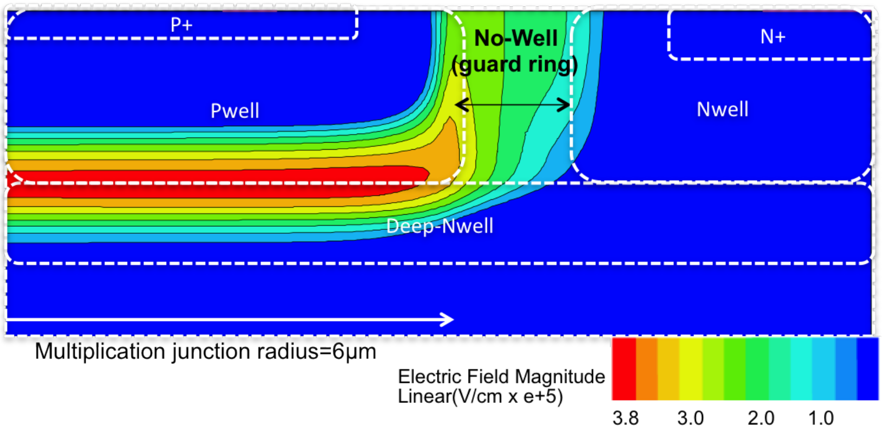

Figure 2.12: Medici simulation of electric field for 12μm active diameter SPAD_RED.

To show the effect of guard rings, the electric field simulation of SPAD_RED without any guard ring between Pwell and Nwell is depicted in Figure 2.13. The multiplication region is not only formed between Pwell and deep-Nwell, but also between Pwell and Nwell. Therefore, the high electric fields cannot be confined to Pwell/deep-Nwell zone and it can cause a premature breakdown in Pwell/Nwell region. In fact, since the penetration depth of RED wavelengths in Si is relatively high, deeper multiplication area is preferred to increase the photon detection probability.

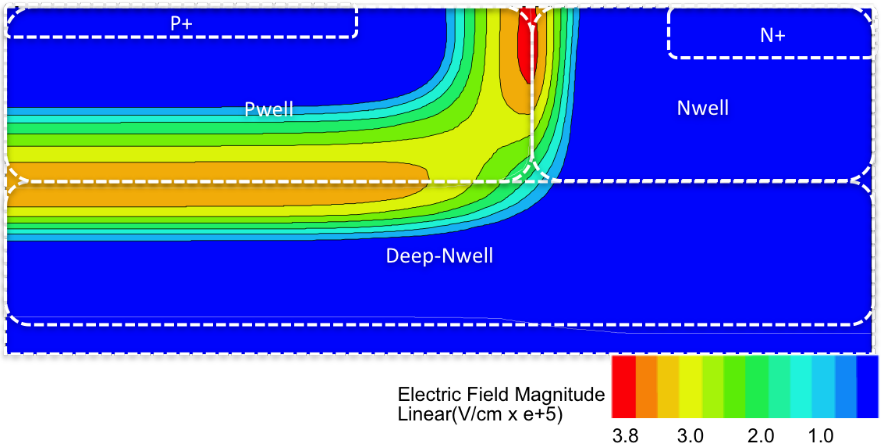

Figure 2.13: Medici simulation of electric field for 12μm active diameter SPAD_RED without guard ring.

The simulation result of current-voltage characteristics in the dark is shown in Figure 2.14. Based on the simulation, we expect a breakdown voltage of ~21.5 V and ~26 V for SPAD1 and SPAD_RED, respectively. The V_{BD} of SPAD_RED is higher because the p-n junction is located between Pwell and Deep_Nwell, which has lower doping concentrations compared to the P^-/N^- junction in SPAD1.

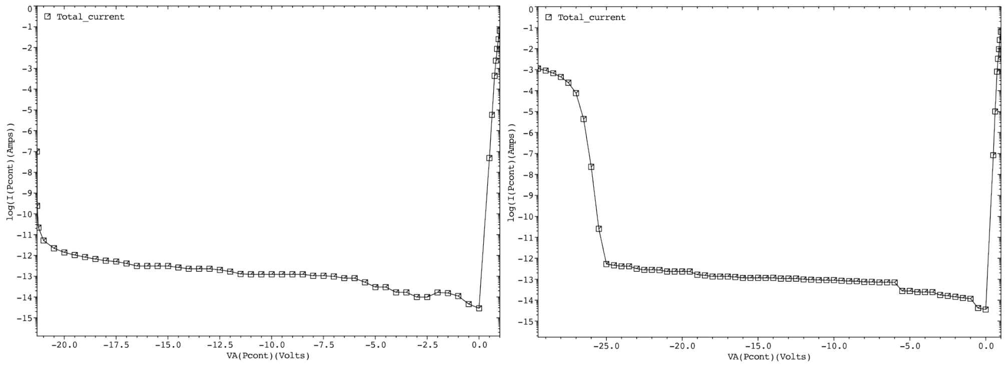

Figure 2.14: TCAD MEDICI simulation of current-voltage for $12\mu m$ active diameter (left) SPAD1, (right) SPAD_RED.

For the simulation of the I-V curve, one of the most important considerations is the analysis of the effect of impact ionization on current and breakdown voltage. Impact ionization is a pure generation process. The generation rate can be modeled by the current densities of electron and hole, and expressed by Equation (2.5) [62].

$$G^{II} = \alpha_n \frac{|\vec{J_n}|}{q} + \alpha_p \frac{|\vec{J_p}|}{q} \tag{2.5}$$

where α_n and α_p are the electron and hole ionization coefficients, and $|\vec{J_n}|$ and $|\vec{J_p}|$ are current densities of electrons and holes. The ionization coefficients α_n and α_p are expressed in Equation (2.6) in terms of an effective driving fields for electrons and holes.

$$\alpha_n = \alpha_n^{\infty} exp[-(\frac{E_n^{crit}}{F_n})^{\beta_n}], \alpha_p = \alpha_p^{\infty} exp[-(\frac{E_p^{crit}}{F_p})^{\beta_p}], \tag{2.6}$$

where E_n^{crit} and E_p^{crit} are the critical electric fields for electrons and holes, α_n^{∞} and α_p^{∞} are ionization rates at infinite field, and F_n and F_p are the effective driving fields for electrons and holes. The critical electric fields can depend on temperature. The effective driving fields in impact ionization expressions are the components of electric field in the direction of electron and hole current flow. Equation (2.7) shows F_n and F_p.

$$F_n = \vec{E}.\frac{\vec{J_n}}{|J_n|}, F_p = \vec{E}.\frac{\vec{J_p}}{|J_p|} \tag{2.7}$$

Equation (2.5) provides means to simulate the behavior of a wide variety of devices where impact ionization related phenomena are important. The parameter values used in these simulations are shown in Table 2.1.

Table 2.1: Parameter values used in simulations.

Parameter	Units	Silicon	Germanium
E_n^{crit}	V/cm	1.23×10^6	1.56×10^6
β_n	-	1	1
E_p^{crit}	V/cm	2.036×10^6	1.28×10^6
β_p	-	1	1

2.3 Ge-on-Si SPAD implementation

The good absorption properties and performance of III-V compounds and alloys, such as InGaAs/InP, have been exploited in many applications where it is required to operate in this band [63]. As an example, available commercial devices based on these technologies can reach quantum efficiency higher than 50% and dark count rates less than 100 Hz. However, they are usually cooled to operate at very low temperatures. Because of lattice mismatch between Si and III-V compounds, a fundamental incompatibility with standard CMOS process is common for all of these technologies, and thus they cannot be used as low-cost photon solutions for large photon-counting pixel arrays. CMOS SPADs cannot be used in the telecom band, because their bandgap enable the detection of shorter than 1.1 μm wavelengths, unless upconversion techniques are used [64]. Such techniques are extremely inefficient and inappropriate in most applications. On the other hand, Ge has a bandgap of 0.67 eV corresponding to deep infrared wavelengths, thus it is a suitable candidate for infrared applications.

2.3.1 Ge-on-Si mushroom structure

Nowadays, although the Czochralski method of ingot growth provides the best quality single crystal Ge, for a low-cost, versatile implementation of Ge devices, techniques such as epitaxial growth on Si substrates are effective means for merging Ge and Si. This enables different Ge applications on standard Si-based CMOS technologies [65, 66].

The technique of merging Ge with Si to reduce the price and obtain better compatibility with CMOS technology has led to the development of several techniques to grow crystalline Ge on Si substrates [41, 67, 68]. Some approaches with better results are, those using SiGe buffer layers [69, 70], lateral overgrowth [71] and aspect ratio trapping (ART) by growth in high aspect ratio trenches [39, 40]. However, these approaches suffer from crystalline quality problem or poor contact between Si and Ge lattices. Ge epitaxial growth on SiGe buffer layers, which can be as thick as a micron, still results in some degree of dislocations degrading the quality of the Ge [72]. The lateral overgrowth and ART techniques, until now, are dependent on critical nano-scale patterning and selective growth over window sizes in the 100 nm range [13].

The Ge-on-Si mushroom method, developed by Prof. L.K. Nanver in Delft and used in this thesis (Figure 2.15), is based on a CVD technique for selective growth of Ge-on-Si substrates that results in low defect crystalline Ge in tens of microns large window sizes. Most of the defects that persist are localized at the interface of Si-Ge and disappear within the first 200 nm of growth. Because the system was adapted for merging GaAs and Si epitaxies in one reactor, the integration of good-quality crystalline intrinsic layer and GaAs doped layers on Ge could be accomplished directly after the Ge growth.

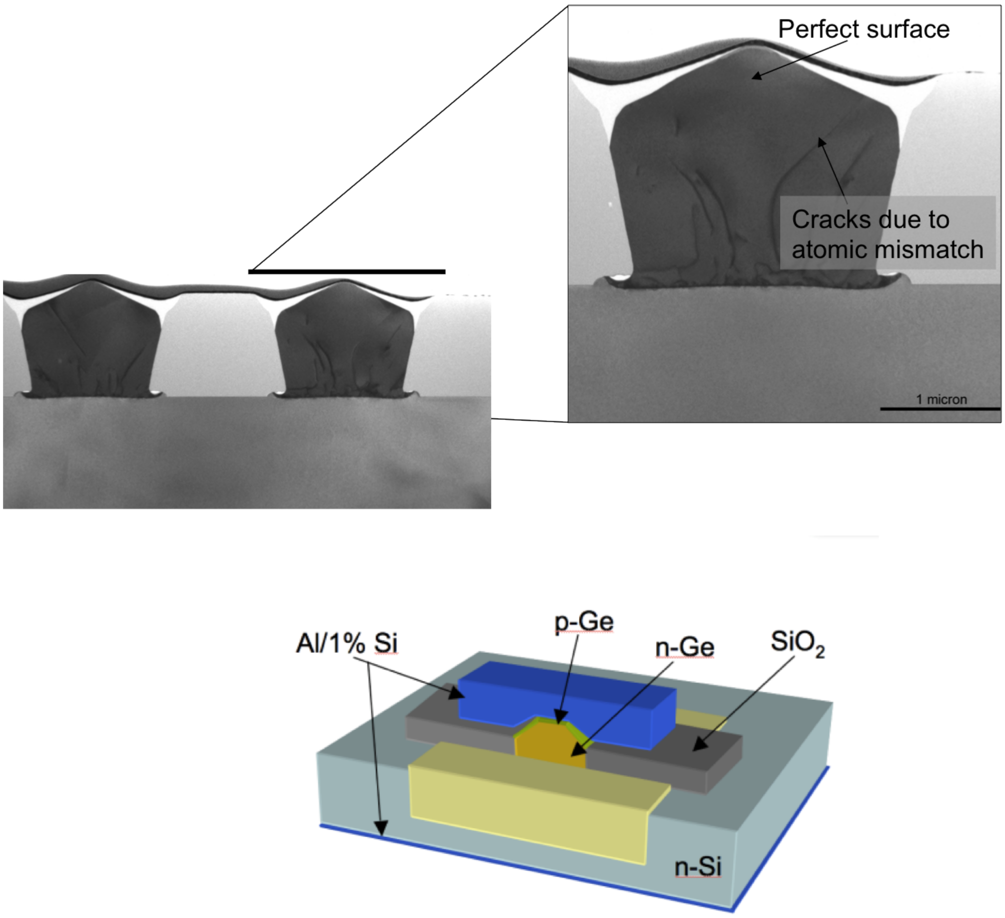

Figure 2.15: Ge-on-Si mushroom structure (Courtesy: A. Sammak and L.K. Nanver, TU Delft).

The selective Ge-on-Si epitaxial growth is using a chemical vapor deposition technique (CVD) to achieve Ge crystals directly on Si substrates. A threading dislocation density in the Ge of $\sim 10^7$ cm^{-2} was achieved with a surface roughness of 4.3Å RMS [73], and the crystal quality was suitable for fabricating electronic devices such as photodetectors. Direct deposition of a nm-thin Ga/B layer stack (so-called PureGaB) on top of the selectively-grown Ge-islands with in-situ n-type doping, delivers high-quality Ge photodiodes with ideality and dark currents that to our knowledge are among the lowest values reported in the literature for any Ge diodes [28].

Experiments have shown that the nm-thick Ga deposition at 400°C on top of Ge forms an ultra-shallow P^+ region and creates a high-quality junction on the surface of Ge. The junction is then covered by a nm-thick B layer, which acts as a barrier protecting the junction from oxidation and also allowing a reliably good contacting to the final Al metallization. The main advantage of this process is that the Ge crystal growth and subsequent deposition of PureGaB take place all in one deposition cycle without any need to break the vacuum of the CVD reactor. This ensures the quality of the junction at the surface of the Ge-crystal islands [74].

The quality of Ge-on-Si crystal is investigated by cross-sectional transmission electron microscopy (TEM) and atomic-force microscopy (AFM) for Ge-islands and PureGaB deposition. Ge-on-Si crystal growth strongly depends on the growth conditions. The temperature should be sufficiently high to allow the chemical reaction to take place and let Ge atoms arrange in a single crystal. In order to get a better quality of Ge-on-Si, low-pressure growth is needed. As the growth temperature increases, more Ge nuclei start to form on large SiO_2 areas that are far from deposition windows. Although the Ge nuclei formation on SiO_2 is negligible at 550°C, the amount of Ge nuclei may cause problems in further processing of the wafers at 700°C, such as short circuiting the electronic devices. The selectivity, however, can be very well controlled by proper pattern design on SiO_2. Experiments show that the surface diffusion length of Ge on LPCVD SiO_2 surface at 700°C is more than 400μm. This means that if the spacing between desired Ge-on-Si regions is more than 800 μm, the Ge nuclei start to form on SiO_2 surface (Figure 2.16 (a)) [13].

To prevent nuclei formation and achieve complete selectivity at 700°C, large size sacrificial regions are designed on the pattern within periodic distances of 800 μm around desired Ge-on-Si regions. These regions can accumulate the Ge nuclei and help to keep a clean SiO_2 surface after Ge growth. Figure 2.16 (a) and (b) shows optical microscopic pictures after selective Ge growth with two different pattern designs without and with sacrificial regions, respectively. Figure 2.16 (b) shows that complete selectivity is achieved while the sacrificial regions gather all the Ge nuclei, which guarantee a clean area around desired Ge-on-Si epitaxy for further processing.

The new Ge-on-Si APD epitaxially grown on Si is used in a manner that is highly compatible with standard Si CMOS processing. The CVD growth technique used to fabricate these p^+n ultrashallow Ge junction diodes has several exceptionally attractive properties, summarized as the following:

- Ge with a very low density of threading dislocations is grown selectively in oxide windows to the Si that can be tens-of-microns large,
- Threading dislocations are trapped within the first 300 nm of Ge growth and good quality single-crystal Ge with a planar surface is achieved for a layer thickness of 1 μm,
- A nm-thin P^+-doping is formed by pure Ga (PureGa) deposition,

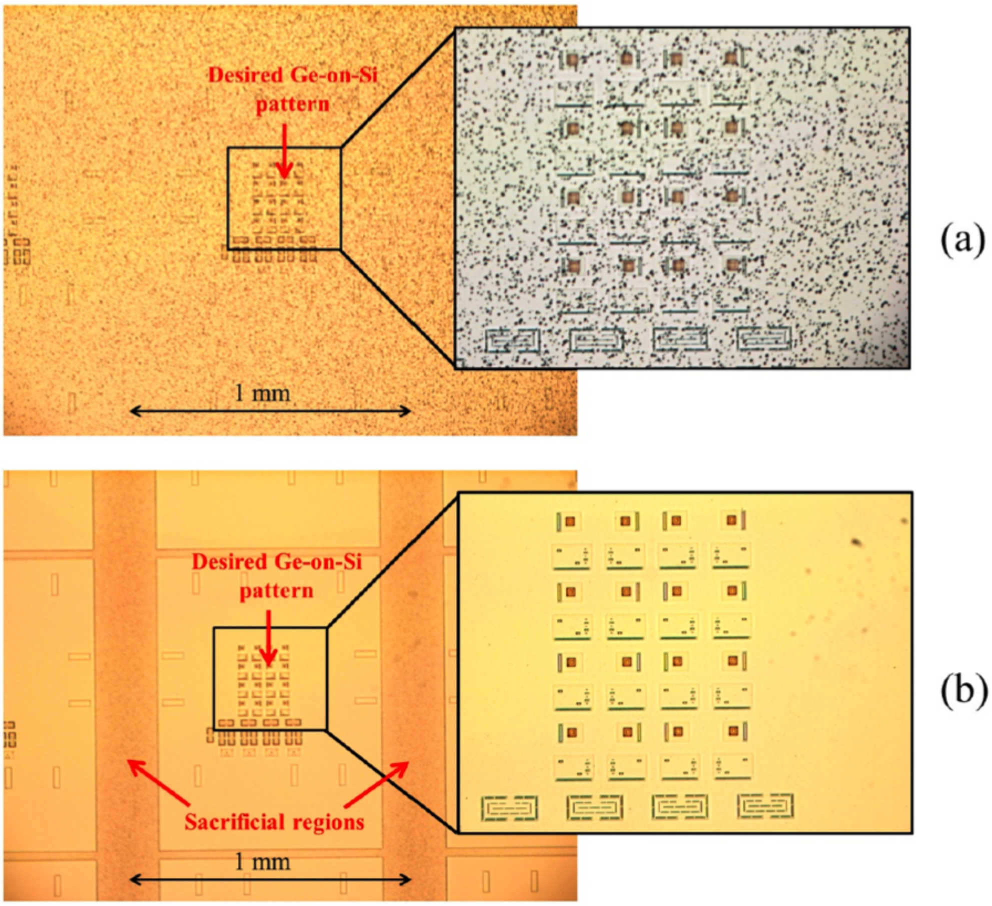

Figure 2.16: Top-view optical image of selective Ge-on-Si (a) without and (b) with sacrificial regions [13].

- After Ga deposition a nm-thin pure B (PureB) deposition is performed to create an amorphous B-layer that is a barrier to the Al-metallization, giving reliable contacting and a low series resistance. The term PureGaB is introduced for the combination of pure Ga/B depositions,
- No extra perimeter isolation techniques were necessary to obtain good diode characteristics and avalanche behavior,
- For maximum photon absorption, the Al-metal on the Ge diode surface can be removed selectively to the PureB layer as has been demonstrated for Si photodiodes in [32].

2.3.2 Process flow

The basic process flow of Ge-on-Si APD fabrication is illustrated in Figure 2.17. The starting material is p-type Si (100) wafers with a resistivity of 2-5 Ω-cm. First a buried n^+-layer is implanted and capped with a 0.5-μm-thick Si epi-layer. Then n^+- and p^+-plugs are implanted for contacting the buried *n*-region and *p*-substrate, respectively. An isolation layer of 1 μm LPCVD SiO_2 is then deposited and those regions where Ge growth is desired are opened by plasma etching to the Si with soft landing. Selective epitaxial growth of Ge is performed in an ASMI Epsilon 2000 CVD Si/SiGe system after a native oxide free Si surface is ensured by doing a HF dip-etch and Marangoni cleaning step followed by a 1-min bake at 1100°C in the reactor itself [28].

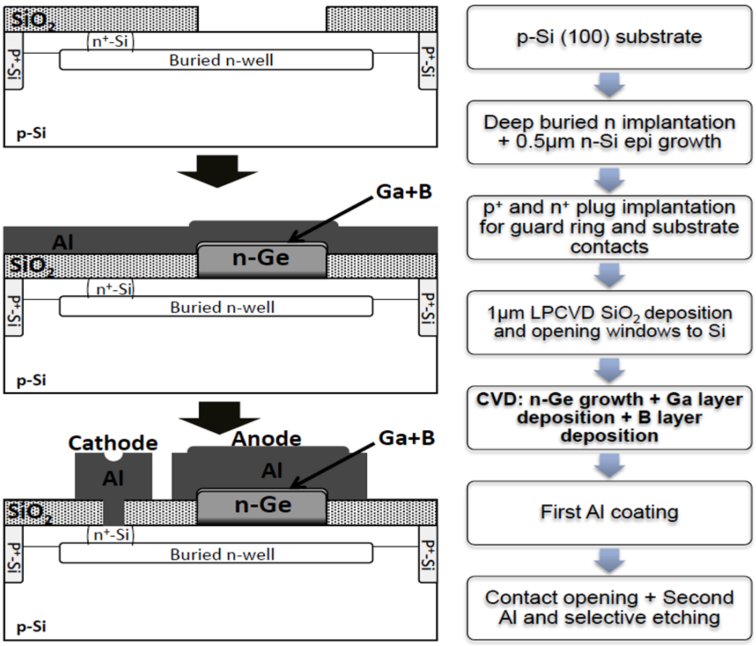

Figure 2.17: Schematic process flow for the fabrication of PureGaB Ge-on-Si photodetector (Courtesy: A. Sammak and L.K. Nanver, TU Delft).

Fabrication of Ge APDs on a Si substrate confronts three basic challenges: 1) epitaxial growth of low defect density crystalline Ge on Si substrate; 2) high quality junction formation that is ultra-shallow, to avoid the depletion region from reaching defects that have propagated from the Ge-to-Si interface and 3) good low-ohmic contacting to the Ge by the metal interconnect. The first challenge is solved here by epitaxial growth of Ge on Si in a standard CVD reactor at a deposition temperature of 700°C. To ensure that the surface is free of native oxide, a HF dip-etch and Marangoni cleaning are performed just before loading the wafers into the CVD reactor and also in the reactor a 4-min baking step at 800°C is applied.

For Ge deposition, 2% diluted GeH4 gas is used as the precursor gas at a pressure of 20 Torr. Such conditions were found to render high quality Ge growth as well as good selectivity of growth on Si over SiO_2. Figure 2.18 and Figure 2.19 show a cross-section TEM/SEM of Ge grown selectively on Si with patterned LPCVD SiO_2, at a deposition temperature of 700°C. Due to the rounded form of the Ge surface, the GaAs growth is not entirely free of dislocations.

The second and third challenges were solved together by fabrication of ultrashallow p^+n

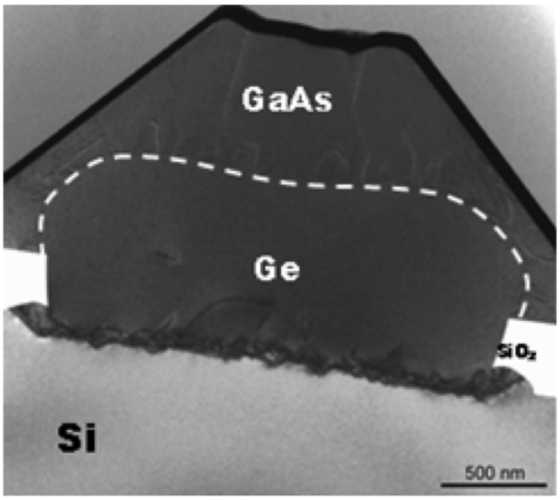

Figure 2.18: Cross-sectional TEM image of a Ge-island epitaxially grown at 700°C on patterned Si followed by in-situ growth of a GaAs layer [75].

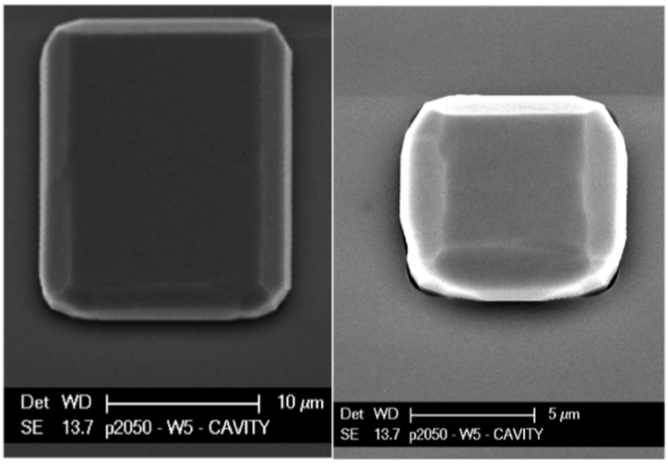

Figure 2.19: Top-view SEM images of Ge-islands grown on a Si substrate, taken before metallization [28].

junction on Ge using the "PureGaB" technology [28]. First, around $1\mu m$-thick epitaxial n-Ge is selectively grown on the patterned Si wafers as described. For n-doping of the Ge during epitaxy, 0.7% AsH_3 is utilized. Taking advantage of the dilution system of the reactor, AsH_3 is further diluted to allow a wider doping range while the average doping of AsH_3 at the desired deposition temperature of 700°C is around 10^{18} atoms/cm^3. Then, in order to form the shallow p^+-doping on the surface of epitaxial Ge, TMGa and B_2H_6 are used for deposition of the so-called PureGaB layer (Figure 2.20). Both these precursors have in the past been shown to dope the Si surface [76, 77]. For Ga this was the most effective approach at a temperature of 400°C and the same conditions have been applied here to create a surface p-doping of the Ge.

On the other hand, exposure of Ge to B_2H_6 does not effectively dope the surface even at 700°C,

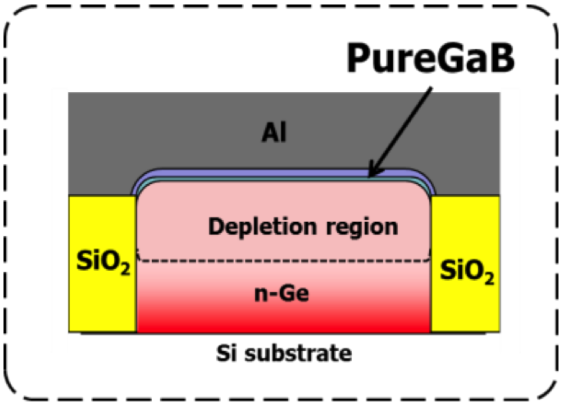

Figure 2.20: Epitaxial n-Ge and PureGaB deposition (Courtesy: A. Sammak and L.K. Nanver, TU Delft).

which is normally used for Si B-layer diodes. However, after doping with Ga, exposure to B_2H_6 will create a thin B-layer on the surface at temperature of $700°C$. The presence of the B-layer has two advantages: before metallization (*e.g.* with sputtered aluminum), it protects the surface against oxidation, and after metallization it protects against Al-spiking in the Ge that could otherwise short-circuit the junction. As the final step of the process, wafers are loaded immediately after APD growth into a sputter coater for a 675nm Al/1%Si deposition to contact the n-type Si and the anode of the p^+n Ge diode.

2.3.3 Ge-on-Si SPAD farm design

Several Ge-on-Si photodiodes with different areas, as large as 40×40 μm^2, were implemented and fabricated by DIMES03 technology at TUDelft DIMES cleanroom [78]. A full layout of the chip is shown in Figure 2.21.

They all displayed good I-V characteristics and the smaller ones could be operated in Geiger mode. Figure 2.22 shows 3×3 μm^2 square-shape device.

This PureGaB technology is an attractive method of fabricating diodes on Ge. PureGaB technology is used to design and implement Ge-on-Si photodiodes that can be operated both in proportional and in Geiger mode. The fabricated Ge-on-Si SPADs exhibit relatively low dark counts rate and high sensitivity at room temperature. In the next chapter, characterization results of the designed APDs with various sizes are described.

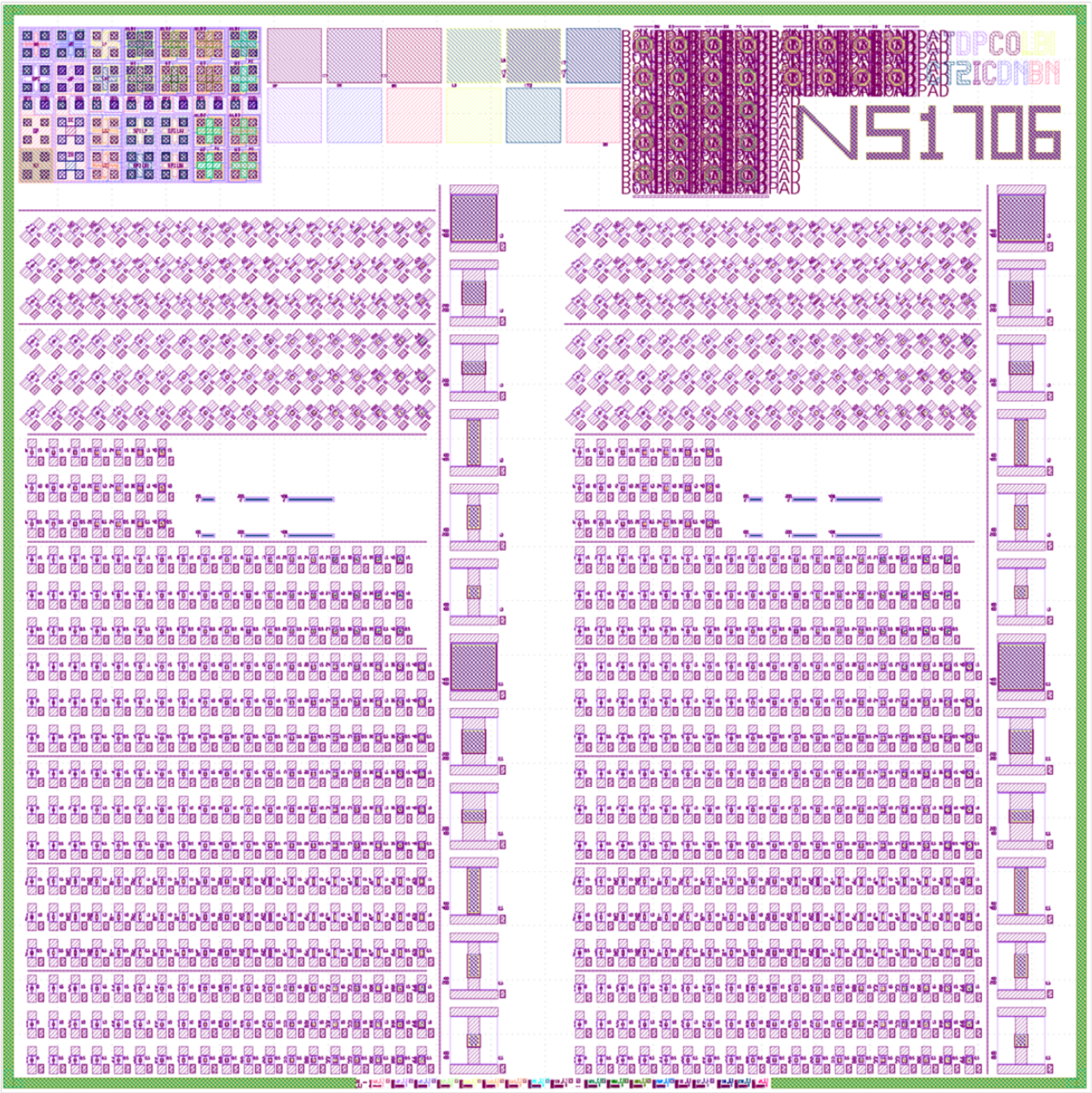

Figure 2.21: Full chip layout of Ge-on-Si SPAD farm.

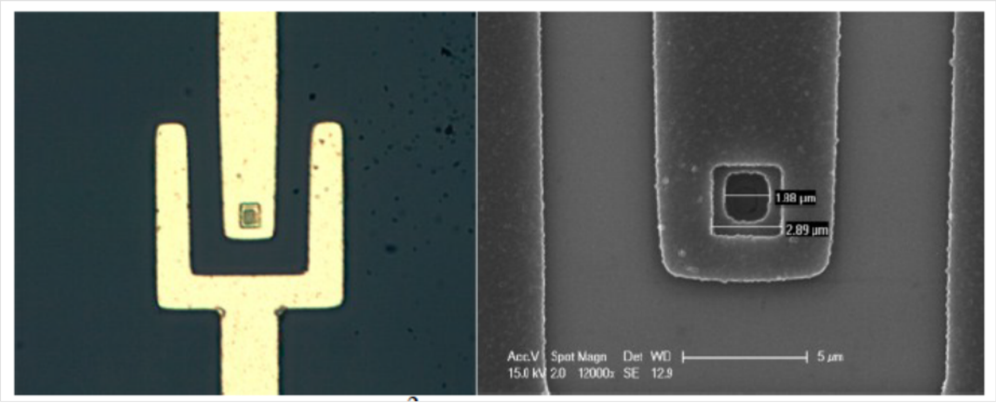

Figure 2.22: PureB/PureGaB dopant-deposition technology for photodiodes with photon-counting potential.

3 Geiger Mode Operation of Experimental SPADs

A CMOS SPAD with high sensitivity in red and near-infrared wavelengths has been implemented and fabricated. The devices are fabricated in an advanced 180nm CMOS imaging sensor technology. The 12μm-diameter SPAD achieves a peak photon detection probability of 29% at 500nm, a low dark count rate of 545 Hz at room temperature and 2 Hz at 77 K; the FWHM timing jitter is as low as 76 ps at a large range of temperatures and excess bias. Complete results are shown in Section 3.1.

Moreover, a CMOS compatible Ge avalanche photodiode has been fabricated on Si by using selective CVD epitaxial growth. This technique, created in the group of Prof. L.K. Nanver (section 2.3.1), enables p^+n diodes with exceptionally good I-V characteristics, ideality factors of ~1.1, and reliably low saturation currents. The measurements show high sensitivity of the photodiodes to IR wavelengths above 1 μm in avalanche and Geiger modes. The detailed experimental results are drawn in section 3.2.

3.1 Si SPAD general characterization

The Si SPADs have been designed and implemented with various structures and sizes. One of the most promissing one is an ultra-deep junction CMOS SPAD that was optimized for red and near-infrared (NIR) sensitivities, while not sacrificing timing jitter performance. The structures, introduced in Section 2-2, have been fabricated and optimized in an advanced 0.18μm CMOS technology with low dark count rate (DCR), thanks to the low density of lattice defects and traps. For the same reasons, the structure is amenable to cryogenic operation. The readout circuits are used to operate in Geiger mode with passive quenching and passive recharge via a ballast resistor. In all the structures, the anode is connected to negative voltage of V_{BD} plus excess bias voltage via the resistor, and the cathode is grounded. The active area diameter of the implemented devices is from 6 μm to 24 μm. Each SPAD was measured at a wide range of temperatures from room temperature to 77 K.

3.1.1 Geiger mode operation

The simplified circuit for operation in Geiger mode is shown in Figure 3.1. The SPAD was biased above breakdown by excess bias voltage V_{ex}. The total negative voltage, V_{op}, is the breakdown voltage plus the excess bias. To operate in Geiger mode, the device is quenched with a 100 $k\Omega$ resistor. The output is sent to a high performance oscilloscope (LeCroy 8600A). The Geiger pulses are illustrated in Figure 3.1 (right).

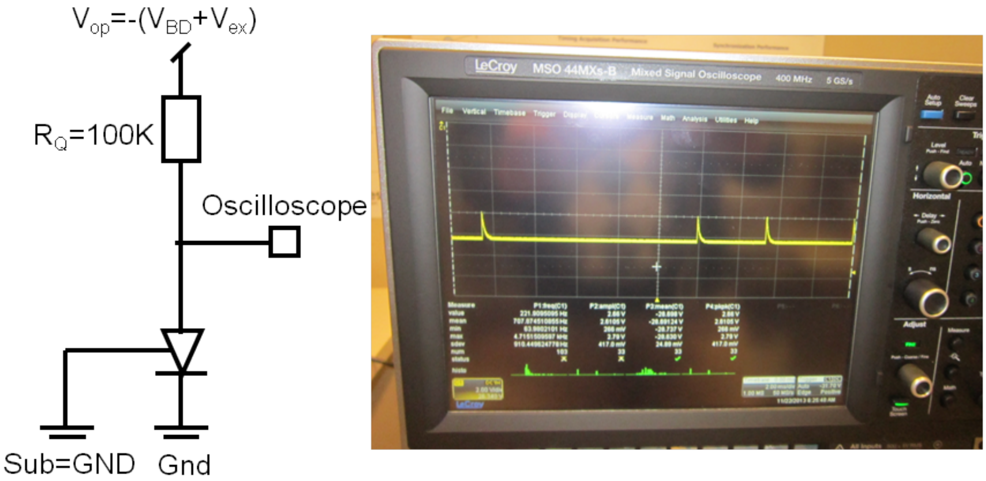

Figure 3.1: Biasing circuit and Geiger pulses.

The ability of devices to operate in Geiger mode for various excess bias values is also tested. Figure 3.2 shows the functionality of SPAD_RED under a variety of excess bias voltages. The device can work in high excess bias voltage without being damaged. The breakdown voltage of this device is near -25 V. For higher excess bias, the voltage drop is bigger until the device is completely quenched.

3.1.2 I-V characteristic

The I-V characteristics of various devices is shown in Figure 3.3. The left graph shows the I-V curves for SPAD1 with various diameters of active area from 6 μm to 24 μm. The breakdown voltage ranges from -21 V to -22 V, higher V_{BD} for smaller devices is generally observed. The results are compatible with simulation results in Chapter 2 for the breakdown voltage.

The right graph shows the I-V curves for SPAD_RED for various diameters. The median breakdown voltage is around -26.1 V. The breakdown voltage is higher than that of SPAD1, mostly because of doping concentrations in the p-n junction. Due to lower edge electric field in SPAD_RED, the breakdown uniformity is higher than that of SPAD1.

Measurements were performed in a probe station with light covering. The SPADs were at room temperature. In smaller devices, a static effect raises the breakdown voltage. Increasing the

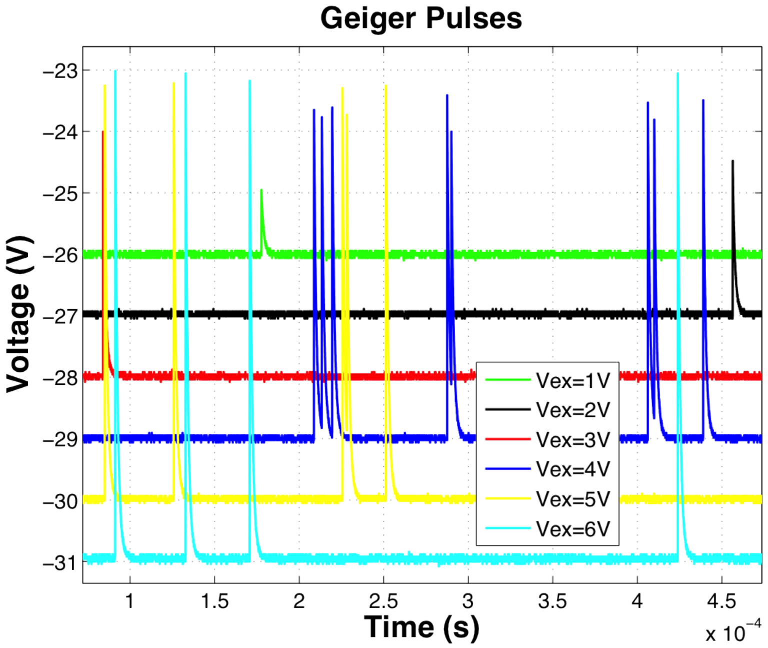

Figure 3.2: Geiger pulses for SPAD_RED under various excess biases.

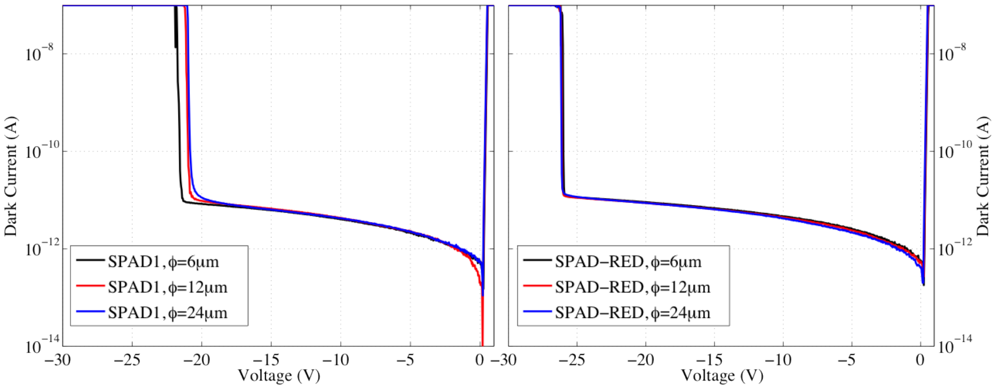

Figure 3.3: Dark current for various SPAD sizes, (left) SPAD1, (right) SPAD-RED.

Pwell or N^- doping would lower the breakdown voltage, indicating that the smaller diodes have a lower doping in their Pwell or N^-.

3.1.3 Light Emission Test

Light emission for a 24 μm SPAD1 and 12 μm SPAD_RED is shown in figure 3.2. The SPADs are properly quenched (with chip area under no light). A light emission test confirmed the presence of a uniform multiplication region and effective edge breakdown prevention at room temperature.

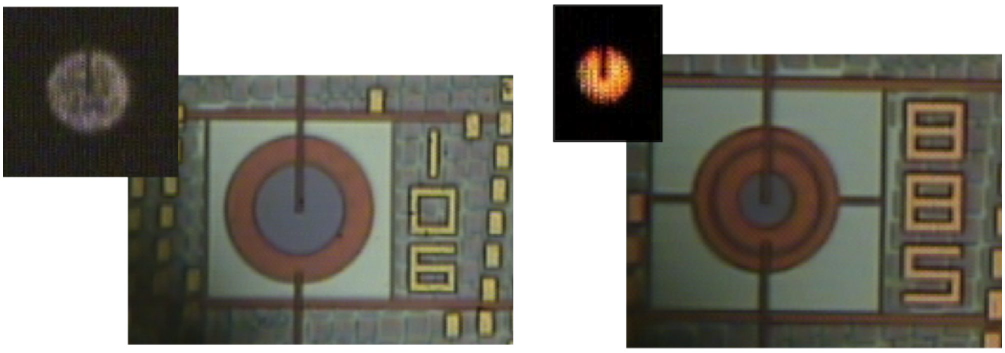

Figure 3.4: Light emission tests of (left) 24 μm SPAD1, and (right) 12 μm SPAD_RED.

3.1.4 Dark count rate

Two devices with three different sizes were characterized in Geiger mode. The SPAD's anode is connected to a high performance oscilloscope (LeCroy 8600A) to count DCR. The minimum V_{op} for Geiger mode operation in SPAD1 is 24 V and SPAD_RED is 29 V; excess biases ranging from 1 V to 6 V are applied with a 1 V step. These V_{op} values are higher than the breakdown voltage, because the leakage current through the quenching resistor and SPAD decreases the actual bias voltage on the photodiode. Figure 3.3 shows the DCR measurement results for different SPADs.

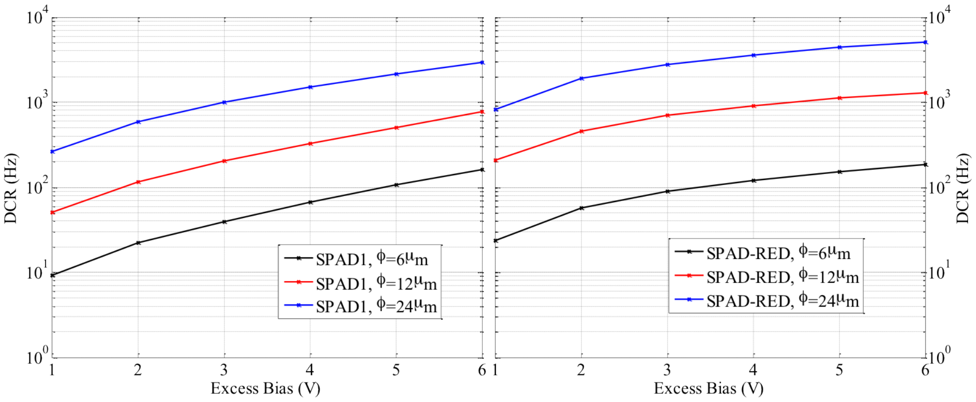

Figure 3.5: Dark counts rate for various device active area, (left) SPAD1, (right) SPAD_RED.

DCR is proportional to the active area of SPADs, while in turn the active area is generally smaller than the drawn area due to the fact that, to prevent PEB, the electric field on the perimeter is lower than that in the center where the avalanche has to be sustained. We call this space inactive area or inactive distance. There are many factors that determine the inactive distance, such as processing variation, annealing of implant layers, and undocumented processing by the CMOS foundry [79]. The assumption in the actual active area estimatation technique is an identical breakdown voltage across the entire active area. Based on the light emission test in the previous section, this assumption is valid for the SPAD1 and SPAD_RED.

The technique used here is based on the measurement of DCR in two or more SPADs with different areas. Let inactive distance d_i be the distance between the edge of the drawn active area and the edge of effective active area. In case of circular devices, the inactive distance is calculated by Equation (3.1).

$$\frac{\pi(r_1-d_i)^2}{\pi(r_2-d_i)^2}=\frac{DCR_1}{DCR_2}$$

$$d_i=\frac{r_1-r_2\sqrt{DCR_1/DCR_2}}{1-\sqrt{DCR_1/DCR_2}} \tag{3.1}$$

where r_1 and r_2 are radii of devices, having DCR_1 and DCR_2. The inactive distance is calculated for SPAD1 and SPAD_RED for radii of 6 μm and 12 μm. The results are shown in Table 3.1 in μm. Results for DCR-based inactive distance estimation show a decreasing inactive distance for both SPAD1 and SPAD_RED as the excess bias increases from 1 V to 6 V.

Table 3.1: Inactive distance calculation.

Device	Radius	$V_{ex}=1V$	$V_{ex}=2V$	$V_{ex}=3V$	$V_{ex}=4V$	$V_{ex}=25V$	$V_{ex}=6V$
SPAD1	$6\mu m$	0.7851	0.6489	0.6266	0.5329	0.4502	0.4420
SPAD1	$12\mu m$	0.9343	0.8363	0.7472	0.5867	0.4319	0.2165
SPAD_RED	$6\mu m$	1.4871	1.3548	1.3375	1.2782	1.2365	1.1595
SPAD_RED	$12\mu m$	1.1612	1.1006	1.0257	0.9796	0.9329	0.8720

3.1.5 Dark count rate versus temperature

DCR was measured as a function of excess bias at various temperatures. Using cooling chamber PMC150 (SUSS Micro-Tech AG), the device was stabilized in temperature at a given temperature; the SPAD's anode was connected to a quenching resistor and a high performance oscilloscope (LeCroy 8600A); the excess bias was swept from 1 V to 6 V. The measured DCR is plotted in Figure 3.6.

Figure 3.6 shows DCR variation as a function of excess bias and temperature for SPAD1 and SPAD-RED with 12 μm diameter. As shown in the figure, the DCR increases as V_{ex} or temperature increase. Different devices may show different DCR behaviors depending on whether tunneling or thermal effects are dominant.

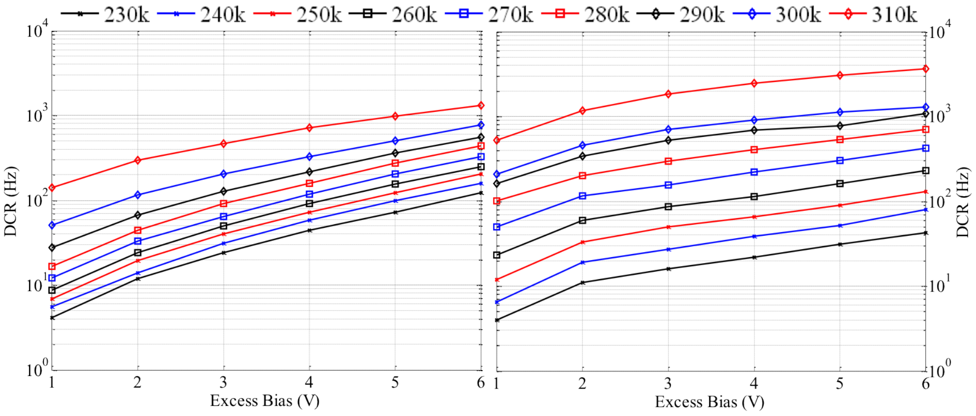

Figure 3.6: Dark count rate (DCR) for the 12 μm active diameter device, from 310 K to 230 K, (left) SPAD1, (right) SPAD_RED.

3.1.6 Arrhenius plot

The traps are normally initiated in the fabrication process. In n-type materials, electrons concentration in the conduction band increases with temperature. In p-type materials, by increasing the temperature, holes concentration in the valance band is increased.

At the room temperature, the impurity atoms are ionized; by increasing the temperature beyond that, both electrons and holes will be increased because of electron excitation from valence band to conduction band (known as electron-hole generation, Equation (3.2)) .

$$I_{G-R} \propto e^{-Eg/2kT} \tag{3.2}$$

Defects and traps in the material can be identified by the activation energy. The activation energy (E_a) indicates the kind of trap material. Because dark current and dark counts rate are proportional to T, the activation energy can be calculated by the Arrhenius plot [19]. The general Arrhenius equation is shown in Equation (3.3).

$$k = Ae^{E\alpha/k_B T} \tag{3.3}$$

where E_a is the activation energy (dark current activation energy at avalanche event), A is a pre-exponential factor and constant, T is the temperature, and k_B is the Boltzmann constant (8.6×10^{-5} eV/K) [80]. Equation (3.4) is the logarithmic version of the Arrhenius equation, whereby E_a can be calculated by fitting a line to the data points.

$$ln(k) = ln(A) - {}^{E_a}/_{k_B}({}^{1}/_{T}) \tag{3.4}$$

Figure 3.7 plots ln(DCR) obtained for SPAD1 and SPAD_RED as a function of 1/T for various excess biases. The thermal activation energy is extracted from the linear fitting. The fitted lines yield activation energy of 0.33 eV to 0.22 eV for SPAD1 and 0.35 eV to 0.32 eV for SPAD_RED which decreases slightly at higher excess bias voltages. SPAD_RED device yields more similar values for E_a over the excess bias than those for SPAD1. The higher variation of E_a in SPAD1 shows higher band-to-band tunneling effect.

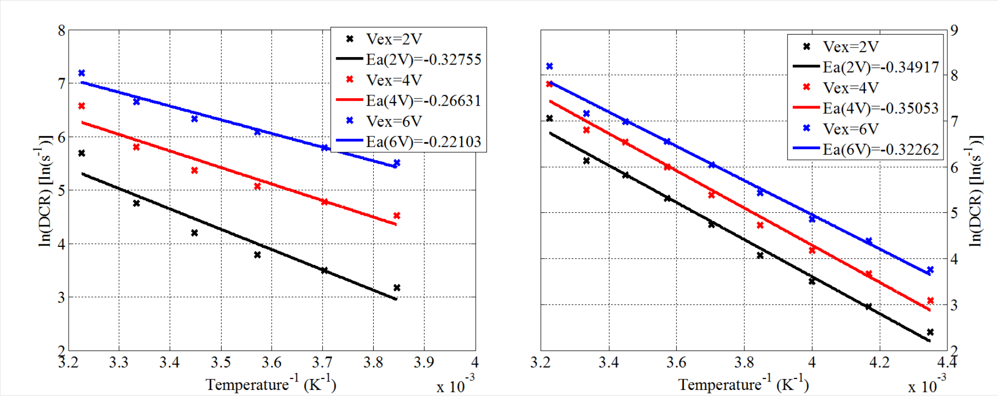

Figure 3.7: Arrhenius plot of DCR for the 12 μm active diameter device, (left) SPAD1, (right) SPAD_RED.

The relatively low thermal E_a shows a moderately deep energy defect in the bandgap, with consequent tunneling, allowing carriers to go through the bandgap. It is also indicating that tunneling currents at room temperature are relatively high.

3.1.7 Photon detection probability

Photon detection probability (PDP) is measured with front-side illumination by the light from a monochromator through an integrating sphere. The active area and incident lights from the monochromator on a SPAD device are shown in Figure 3.8. The monochromator light spot is covering all the active area. The incident power to devices was measured with a power meter and the beam area was calculated. The PDP is estimated by the ratio of detected and incident photons.

Figure 3.9 shows the PDP measurement results for a 12 μm device at various excess bias voltages from 1 V to 4 V. The PDP peak is 29% at 4 V excess bias and at 500 nm, and more than 10% for 700 nm wavelength (deep-red range).

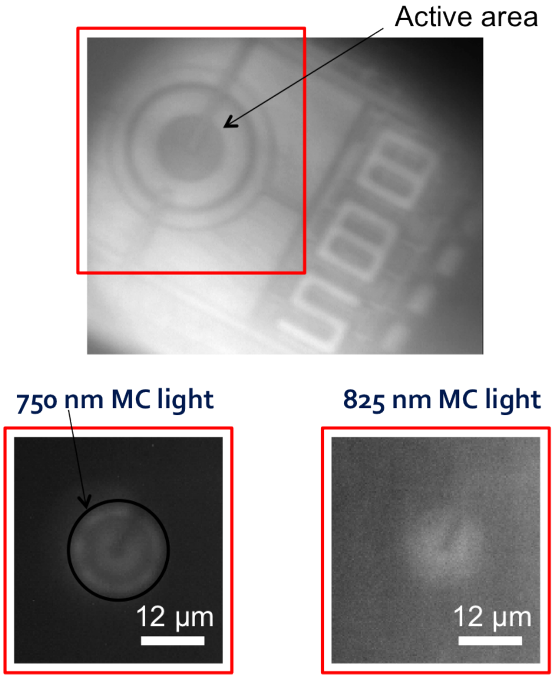

Figure 3.8: PDP measurement (top) 12μm-diameter SPAD active area, (bottom) light beams of 750 nm and 825 nm.

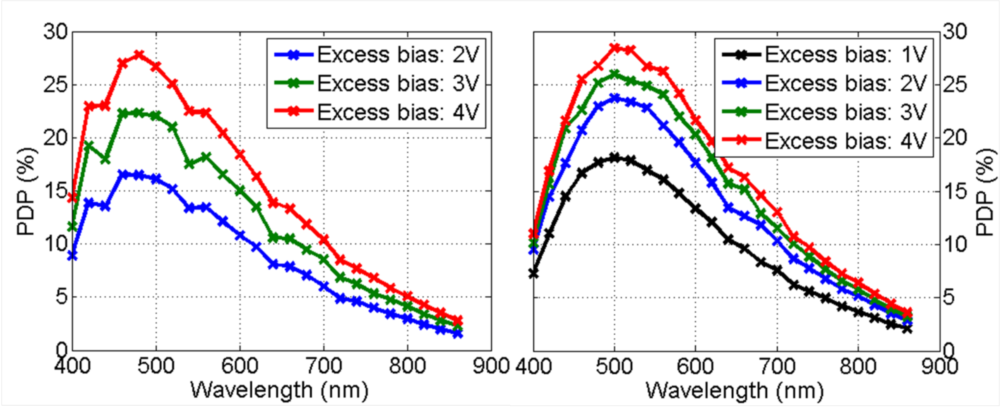

Figure 3.9: PDP for the 12 μm active diameter device, (left) SPAD1, (right) SPAD_RED.

3.1.8 Timing jitter

The statistical timing variation of Geiger depends on the position of free carriers within the depletion region. The avalanche timing uncertainty can be expressed in terms of the carrier transit time range through the junction at saturation velocity [81]. Normally, the Gaussian distribution of avalanche events is the dominating source of SPADs jitter. Therefore, the timing jitter of a SPAD is usually given as the full-width-half-maximum (FWHM) of the photon arrival time distribution. In addition to the Gaussian distribution of avalanche events, a small tail of lower amplitude is typically present in the SPAD's timing characteristics. The tail can be referred to diffusion; photons absorbed beneath the depletion region create an electron-hole pair and the minority carrier. The generated carriers may diffuse back into the avalanche region and trigger another breakdown event. The tail timing jitter induced by diffusion can be significantly larger than the jitter from the avalanche events, because diffusion is a slow process. Moreover, since the mean penetration depth of a photon is strongly dependent on wavelength, the characteristics of the diffusion tail notably change in function of the wavelength.

To measure timing jitter, the SPAD was illuminated by a picosecond laser diode source emitting pulses at a specific wavelength. Two laser sources have been used, an 80ps-pulse-width 40 MHz picosecond laser at 637 nm wavelength (Advanced Laser Diode Systems GmBH, Berlin, Germany), and a 50ps-pulse-width 20 MHz picosecond laser at 785 nm wavelength (Becker & Hickl GmBH, Berlin, Germany). The time interval between the laser output trigger and the consequent edge of the SPAD signal was measured using a Rohde&Schwarz RTO1044 high-performance oscilloscope. To avoid pileup, a neutral density filter (NDF) was inserted between laser and SPAD. The timing jitter of the entire system (including laser, detector and oscilloscope) is shown in Figure 3.10 and Figure 3.11 for 785 nm and 637 nm lasers, respectively.

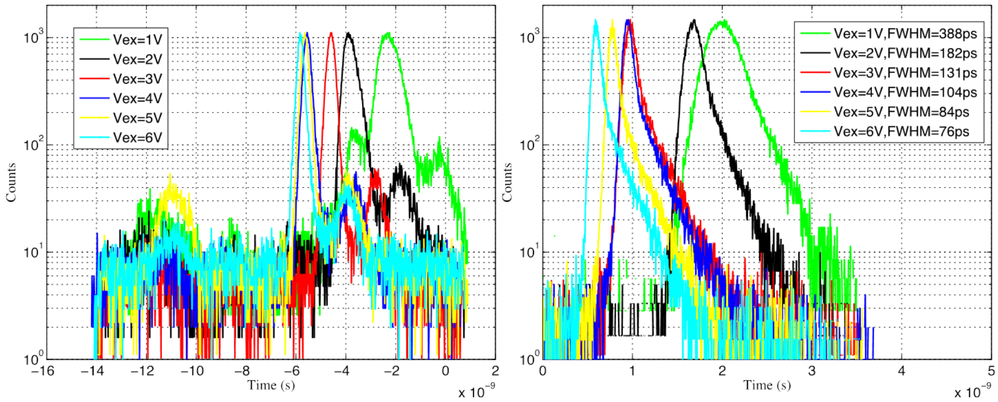

Figure 3.10: Jitter performance of Si SPADs, illuminated by a pulsed laser source at a wavelength of 785 nm with a pulse width of 50 ps, (left) SPAD1, (right) SPAD_RED.

The summary of full-width-half-maximum is reported in Table 3.2. The FWHM of timing jitter including laser and photodiode jitters is measured as 115 ps and 76 ps at 6 V excess bias for SPAD1 and SPAD_RED, respectively.

Table 3.2: Timing jitter for SPAD1 and SPAD_RED.

Device	laser λ	$V_{ex} = 1V$	$V_{ex} = 2V$	$V_{ex} = 3V$	$V_{ex} = 4V$	$V_{ex} = 25V$	$V_{ex} = 6V$
SPAD1	785nm	677.04ps	366.97ps	294.3ps	207.89ps	151.89ps	115.79ps
SPAD1	637nm	908.9ps	548.81ps	355.86ps	305.02ps	292.6ps	273.46ps
SPAD_RED	785nm	388ps	182ps	130.98ps	104.08ps	84.5ps	76.02ps
SPAD_RED	637nm	778.23ps	392.57ps	312ps	259.29ps	282.43ps	263.79ps

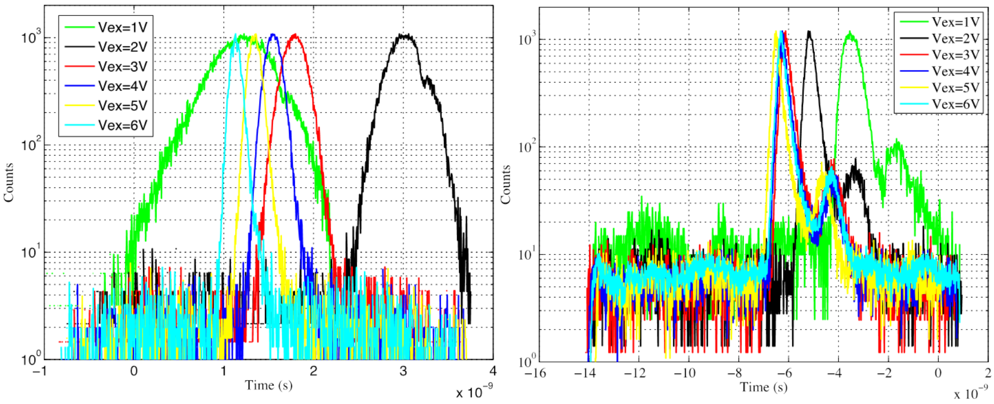

Figure 3.11: Jitter performance of Si SPADs, illuminated by a pulsed laser source at a wavelength of 637 nm with a pulse width of 80 ps, (left) SPAD1, (right) SPAD_RED.

3.1.9 Afterpulsing probability

Afterpulsing can be limited by decreasing the quantity of charges passing through the diode during breakdown, thereby limiting the chance for filling the traps. It can be done by minimizing the parasitic capacitance at the border of the photodiode as carriers are discharged through the device during breakdown. The quenching circuitry should be placed as close as possible to the detector to reduce the parasitic capacitances. Another way of decreasing the afterpulsing probability is reducing the trap density within the SPAD, which is process dependent.

To calculate the afterpulsing probability, the distribution of avalanche event within time should be plotted. The inter-avalanche time under constant light intensity is measured. The afterpulsing distribution is depicted in Figure 3.12. The device was biased at a variety of excess bias voltages, left for 12h, and measured with a high Rohde&Schwarz RTO1044 high performance oscilloscope.

Because the SPADs are connected directly to PADs, the parasitic capacitance is large. Therefore, afterpulsing probability is expected to be relatively high. However, an internal comparator and quenching mechanism could drastically reduce afterpulsing.

3.1.10 Performance summary

The summary of the performance characterization of the SPAD devices is shown in Table 3.3 for two different implemented structure families ($'\phi'$ is the diameter of active area). The active area of the photodiodes is from 28.3 to 452.2 μm^2. The breakdown voltages of the devices are -21.2 V and -26.2 V for SPAD1 and SPAD_RED, respectively. The excess biases of 0 to 6 V were applied to the SPADs for DCR and jitter measurements.

DCR is as low as 9.2 Hz for 3μm-radius SPAD1 and 23.6 Hz for 3μm-radius SPAD_RED at

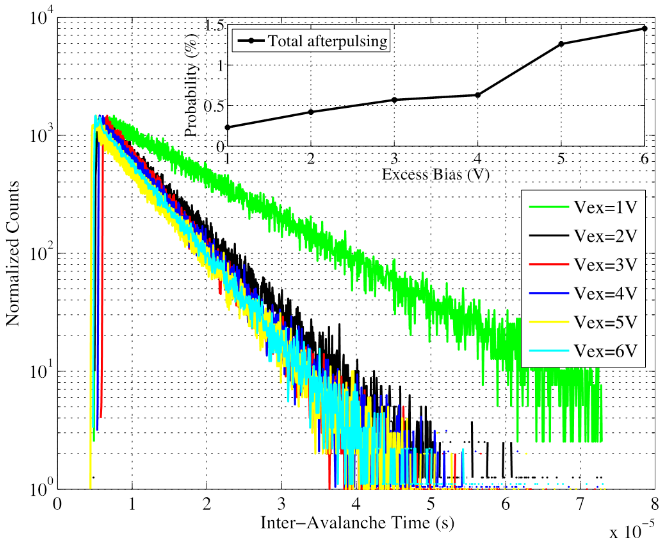

Figure 3.12: Afterpulsing distribution for the 12μm active diameter Si SPAD for various excess biases, (inset) total afterpulsing probability.

Table 3.3: Silicon SPADs performance summary and comparison.

Parameters	SPAD1			SPAD_RED		
	Min.	Typ.	Max.	Min.	Typ.	Max.
Active area $[\mu m^2]$	28.27	113.1	452.39	28.27	113.1	452.39
V_{BD} [V]	-21	-21.25	-21.8	-26	-26.2	-26.25
V_{ex} [V]	1	4	6	1	4	6
DCR [Hz] @V_{ex}=1V	9.2 $\phi=6\mu m$	51 $\phi=12\mu m$	264 $\phi=24\mu m$	23.6 $\phi=6\mu m$	210 $\phi=12\mu m$	820 $\phi=24\mu m$
DCR [Hz] @V_{ex}=4V	67.2 ϕ=6μm	330 ϕ=12μm	1503 ϕ=24μm	121 ϕ=6μm	910 ϕ=12μm	3600 ϕ=24μm
DCR density @V_{ex}=4V $\left[Hz/\mu m^2\right]$	2.38	2.92	3.32	4.3	7.96	8.05
PDP peak [%]	-	16.5 480nm	27.7 480nm	18.1 500nm	23.7 500nm	28.5 500nm
FWHM jitter @637nm [ps]	273.46 V_{ex}=6V	305.02 V_{ex}=4V	908.9 V_{ex}=1V	259.29 V_{ex}=4V	263.79 V_{ex}=6V	778.23 V_{ex}=1V
FWHM jitter @785nm [ps]	115.79 V_{ex}=6V	207.89 V_{ex}=4V	677.04 V_{ex}=1V	76.02 V_{ex}=6V	104.08 V_{ex}=4V	388 V_{ex}=1V
Afterpulsing probability [%]	0.22 V_{ex}=1V	0.43 V_{ex}=4V	-	0.23 V_{ex}=1V	0.63 V_{ex}=4V	1.45 V_{ex}=6V

1 V excess bias at room temperature. Density of dark counts rate is lower than 3.5 and 8 $Hz/\mu m^2$ at room temperature for SPAD1 and SPAD_RED at 4 V excess bias. The SPAD_RED

achieves high PDP of 29 % at 500nm and 13% at 700nm wavelengths. Moreover, the jitter of SPAD_RED is lower for the deep-red laser (785 nm) than that for the red laser (637 nm). More improvements will be achieved by integrating readout circuits in the future fabrications.

3.2 Ge-on-Si SPAD Characterization

The Ge-on-Si SPADs were fabricated with different sizes and shapes of active Ge area. The square shapes with various widths are reported in this section. The devices have 0.5 μm n-Si expitaxy growth and $1 \mu m$-thick Ge absorption layer.

3.2.1 I-V characteristic

Figure 3.13 shows the current-voltage (I-V) characteristics of two different sizes of photodiodes. The breakdown voltages, V_{BD}, for these devices are 9 V and 13 V for the 2×2 μm^2 and 2×20 μm^2 devices, respectively. Ideality factors of 1.1 to 1.3 were measured for all sizes. The dark current for the smallest device is as low as 2 pA and increases to hundreds of micro-amps for after the breakdown voltage, while the series resistance is as low as possible in this process.

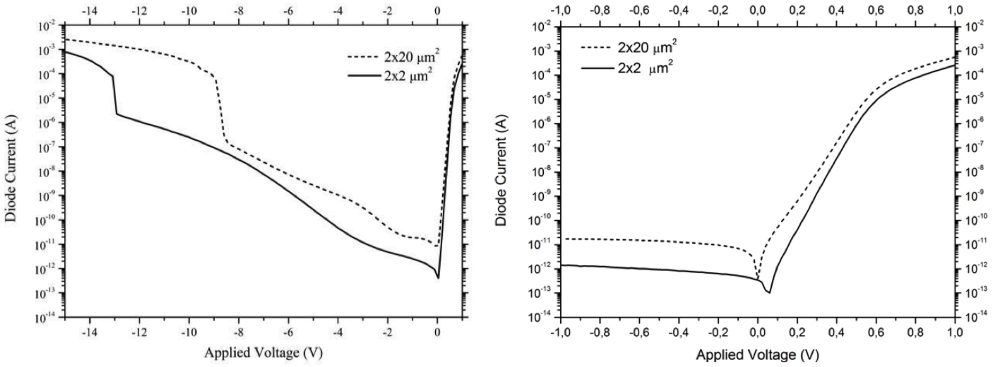

Figure 3.13: I-V characteristics for 2×2 μm^2 and 2×20 μm^2 Ge-on-Si APD device area, (left) breakdown of 9 V and 13 V, (right) ideality factor of 1.15 and 1.35, respectively.

3.2.2 CV profiling

The capacitance-voltage characteristics, C-V, of two different device sizes are shown in Figure 3.14 where they have identical perimeters but different areas. The C-V measurements are for photodiodes with geometries of 2×20 μm^2 and 10×10 μm^2 , reverse biased at 0 to 8 V. It can be concluded that capacitance is slowly increasing with area. Due to a loading effect combined with a low diffusivity of the As across the Ge surface, this is a non-uniform doping of each island. It causes higher doping at the peripheral area than the central regions. This results in higher peripheral capacitance per unit than the bulk capacitance [82].

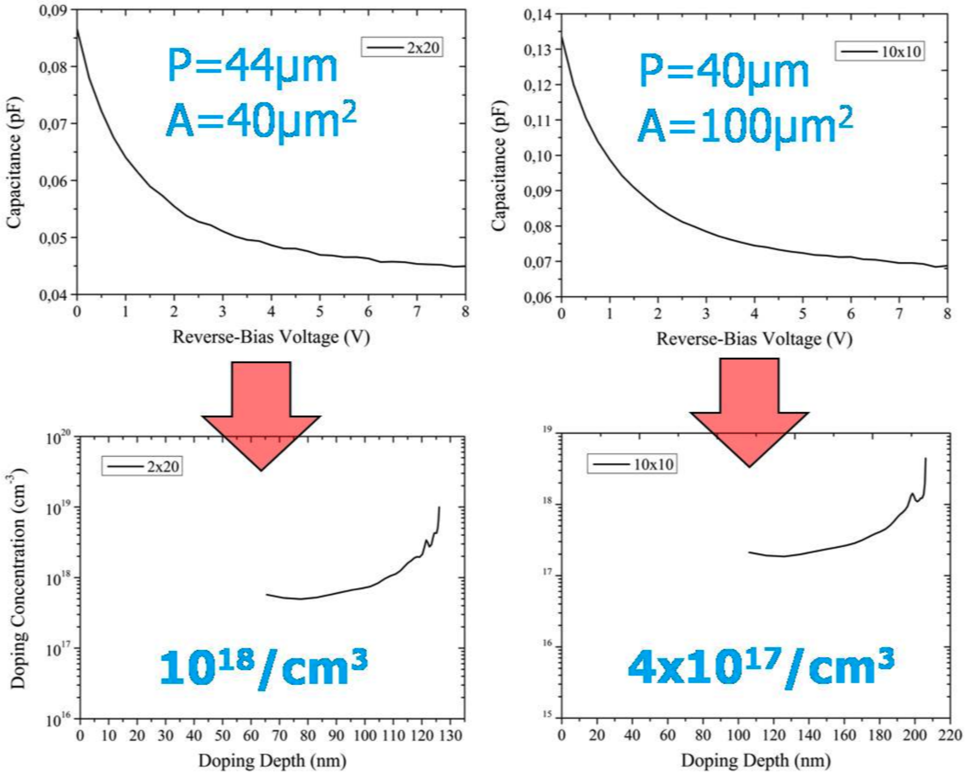

Figure 3.14: C-V profiling for two different Ge-on-Si APD sizes with same perimeter but different areas, (left) $2 \times 20\ \mu m^2$ device, (right) $10 \times 10\ \mu m^2$ device.

3.2.3 Geiger mode operation

The circuit for APD operation with quenching resistance is shown in Figure 3.15. The APD was biased above the breakdown voltage by the excess bias (V_{ex}), whereas $V_{op} = V_{BD} + V_{ex}$. The excess bias varies from 0 to 4 V. To operate in Geiger mode, the device must be quenched with a 64 $k\Omega$ resistor. The output is sent to a comparator and a counter or a time-to-digital converter.

3.2.4 DCR

Figure 3.16 shows the dark count rate for three different sizes of photodiode devices. The measurement is a function of excess bias voltage that is let vary from 0 to 2 V at room temperature. We can compare the DCR of the SPADs at room temperature and the rates reported in [83], where the best DCR is 3×10^7 for 1% excess bias at 180 K temperature. This shows the better quality of Ge growth on top of silicon.

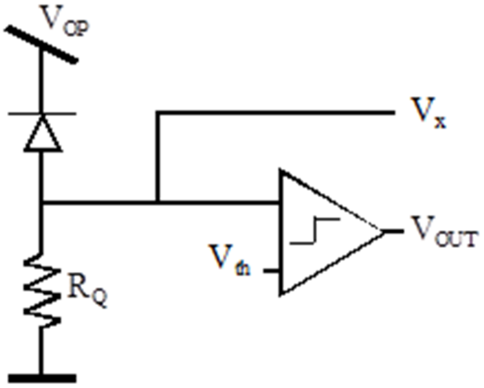

Figure 3.15: The SPAD biasing and test circuit.

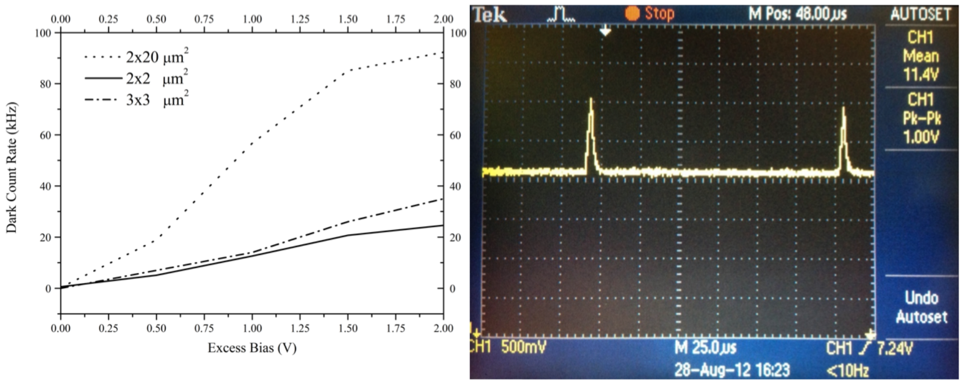

Figure 3.16: Dark count rate for three Ge-on-Si SPAD devices with size of $2 \times 2\ \mu m^2$, $3 \times 3\ \mu m^2$, and $2 \times 20\ \mu m^2$.

3.2.5 Photoresponse

The dark current and photo-response for the $2 \times 20\ \mu m^2$ device are shown in Figure 3.17 in linear and proportional APD modes. The larger the infrared-induced the higher the sensitivity of Ge photodiodes to infrared photons. Also, the current after breakdown voltage (11 V) is 500 times larger than proportional APD mode current of 200 nA.

The photocurrent I_d of the $2 \times 20\ \mu m^2$ photodiode is measured at different wavelengths for different bias voltages. The I_d is compared with the photocurrent I_{ref} measured on a reference photodiode for which the quantum efficiency QE is known for all interesting wavelengths. Figure 3.18 shows the ratio I_d/I_{ref} as a function of wavelength for the bias of 3 V and 9 V (below breakdown), as well as 14 V and 15 V (Geiger mode). The peak of 27% was measured for an excess bias of 3 V and 4 V at infrared wavelength of 1100 nm in Geiger mode.

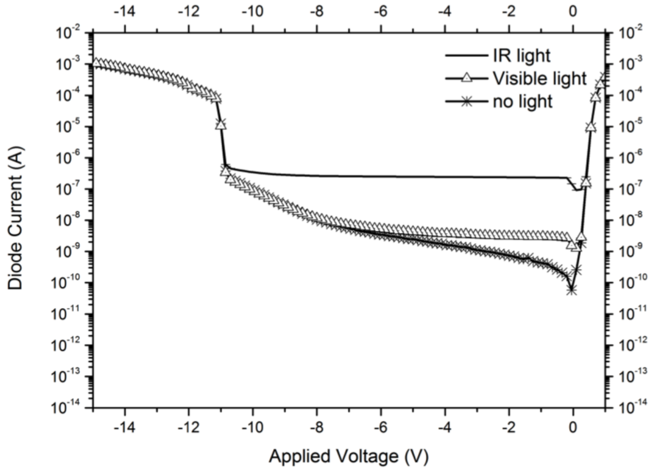

Figure 3.17: Dark current and photo-response of $2 \times 20\ \mu m^2$ Ge-on-Si photodiode as a function of reverse bias.

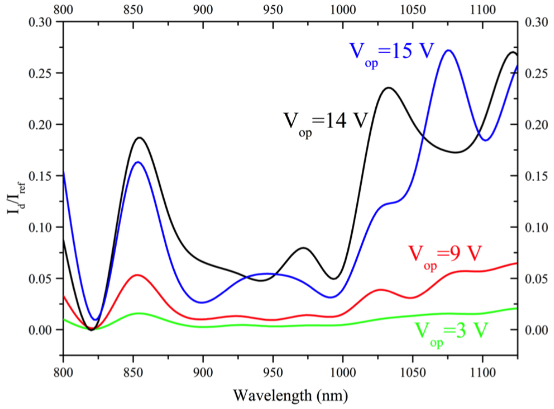

Figure 3.18: I_d/I_{ref} of the $2 \times 20\ \mu m^2$ Ge-on-Si APD in the NIR spectrum for various bias voltages V_{OP}.

3.2.6 Timing jitter

The jitter performance of the $2 \times 2\ \mu m^2$ photodiode is plotted in Figure 3.19 when the SPAD operated in Geiger mode at 1 V excess bias. A pulsed laser centered at 637 nm (Advanced Laser Diode Systems GmBH, Berlin, Germany) with a pulse width of 80 ps was used. The measurement was done using the embedded time discriminator of a LeCroy WaveMaster 8600A. The measured FWHM time jitter was 900 ps. We believe that this result can be improved by decoupling the SPAD from the setup through an integrated pulse shaper and/or a comparator, combined with active quenching/recharge, thus resulting in a much reduced parasitic capacitance at the anode of the SPAD.

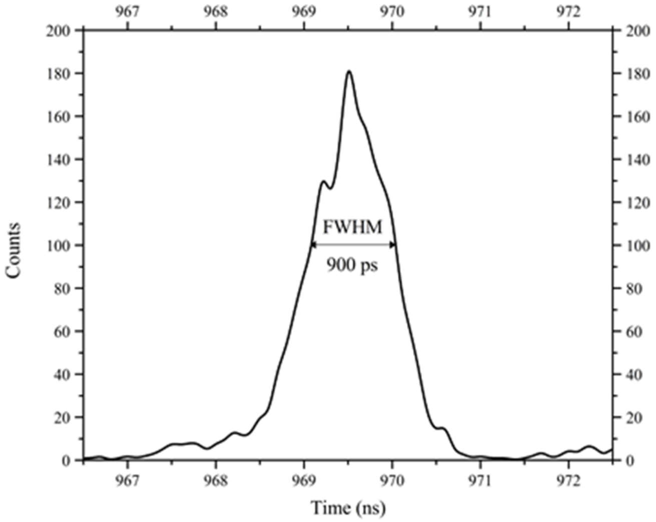

Figure 3.19: Jitter performance of the $2 \times 2\ \mu m^2$ Ge-on-Si APD when operated in Geiger mode.

3.2.7 Performance summary

The summary of the performance characterization of the photodiodes is shown in Table 3.4 and Table 3:6 for three modes of operation (Linear, APD, and Geiger). The active area of photodiodes has been chosen from 4 to 40 μm^2. The breakdown voltages of the devices can be controlled in the fabrication process with a range of 9 V in minimum to 13 V at maximum. The excess biases of 0 to 4V were applied to the APDs for DCR measurements. DCR is as low as 10 kHz for $2 \times 2\ \mu m^2$ APD device at 1 V reverse bias.

Table 3.4: Performance of Ge-on-Si photodiodes in conventional mode.

Performance	Min.	Typ.	Max.	Unit
Active area	4		40	μm^2
Breakdown voltage	9	11	13	V
Dark current @1V reverse bias	2		20	pA

Table 3.5: Performance of Ge-on-Si photodiodes in APD/SPAD mode.

Performance	Min.	Typ.	Max.	Unit
Excess bias voltage	0		4	V
DCR @V_{ex}=1V	10		60	kHz
I_d/I_{ref} @V_{ex}=3V			25	%
FWHM time jitter			900	ps

The fabricated Ge APD detectors can be operated both in proportional and in Geiger mode.

They exhibit relatively low dark counts and high sensitivity at room temperature. This correlates well with the fact that the I-V characteristics have, to our knowledge, uniquely low values of reverse current, series resistance and ideality factors as well as good uniformity across the wafer.

4 Near-Infrared Ge-on-Si APD and SPAD array

This chapter focuses on the design and characterization of arrays of Ge-on-Si pixels and the corresponding readout architecture. Several Ge-on-Si array implementations are discussed, Followed by the characterization of larger line arrays.

4.1 Ge-on-Si 4×4 array simulation and implementation

After the exceptionally good results of Ge-on-Si photodiodes, Ge-on-Si SPAD arrays are the next step. Therefore, designing several kinds of small 2D array and large 1D arrays have been considered. In the first step, several types of small 2D arrays with different pixel size and read-out circuits have been designed and implemented. The schematic of a 2D SPAD array concept is shown in Figure 4.1. Pixel decoders and row decoders are used to address a specific SPAD pixel or entire a row. At end of the rows, there are readout circuits to transfer detected photon counts to the exterior of the chip.

The 4×4 Ge array consists of Ge photodiodes with an integrated quenching mechanism for each pixel and a readout circuit for each column. The fabrication technology of Ge-on-Si allows us to integrate pJFET and BJT transistors. Using these transistors, three different types of pixels and corresponding readout circuit have been designed and simulated. Since the output voltage level of SPADs is relatively low, the readout circuits are aimed at amplifying the SPAD outputs.

4.1.1 JFET-pixel and NPN-readout array

The schematic of the first full pixel is shown in Figure 4.2 (left). The main component is a Ge-on-Si SPAD controlled by a pJFET transistor. This transistor performs the quenching operation and controls the SPAD on/off mode. If the row is selected, the SPAD can be operated at V_{OP} voltage. The generated signals upon arriving photons can be transmitted to the column by another pJFET switch. Each column has a NPN-based readout circuit to convert the analog signal to digital pulse to be readable at output pads.

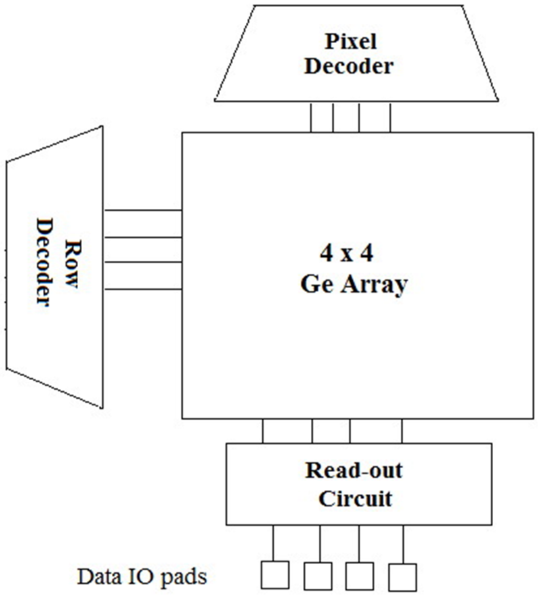

Figure 4.1: Block diagram of a 4×4 SPAD pixel array.

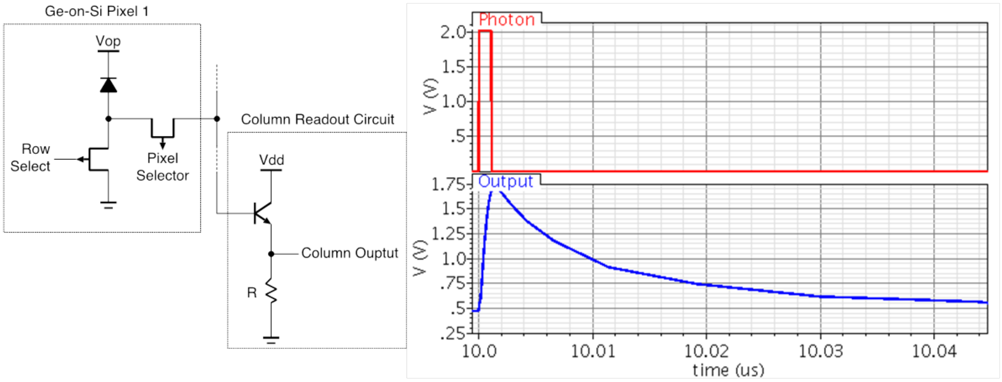

Figure 4.2: JFET type Ge pixel and NPN readout circuit (left), simulation result (right).

For the simulation, the arriving photons are modeled by a narrow voltage signal. The NPN follower circuit (the column readout circuit in Figure 4.2 (left)) can generate SPAD pulses with 1.75 V amplitude, which is enough to be sensed by external monitors. The SPAD dead time, in this case, will be around 30 ns.

4.1.2 JFET-pixel and PNP-differential-amplifier-readout array

The second pixel is shown in Figure 4.3 (left). A pJFET transistor and a resistor control the Ge-on-Si SPAD. The pJFET transistor controls the on/off mode of the pixel, and determines the excess bias. A pixel is selected by biasing voltage V_b. The resistor performs the quenching operation. Detected photons trigger a current pulse, which is propagated along the column. A PNP-based differential amplifier senses the current variation with amplification to generate the output voltage signal. The amplifier circuit generates SPAD pulses with peak of 1.25 V amplitude, and around 40 ns dead time.

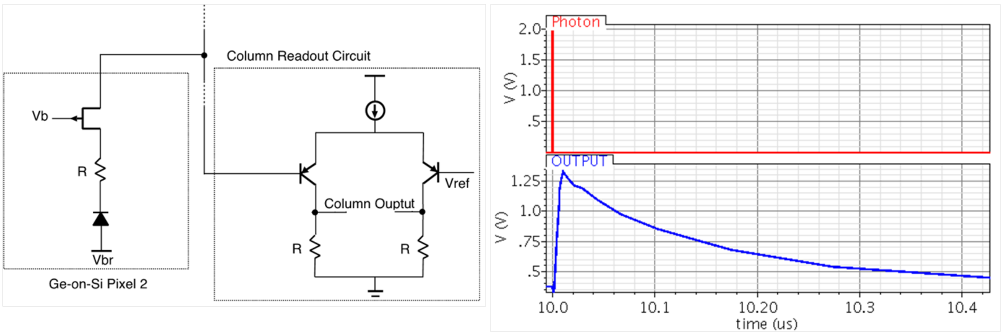

Figure 4.3: JFET-resistor type Ge pixel and PNP-differential-amplifier readout circuit (left), simulation result (right).

4.1.3 JFET-pixel and common-emitter-amplifier-readout array

Figure 4.4 (left) shows the third pixel design. Similarly to the second pixel design, a pJFET transistor and a resistor control the Ge-on-Si SPAD. The pJFET transistor controls the on/off mode and bias the SPAD above breakdown, and the resistor quenches the device. Absorbed photons trigger a current in the column. A PNP-based preamplifier senses the current variation and amplifies it to generate the output voltage signal. While the amplifier circuit generates SPAD pulses with peak of 2.25 V amplitude, the dead time is around 250 ns.

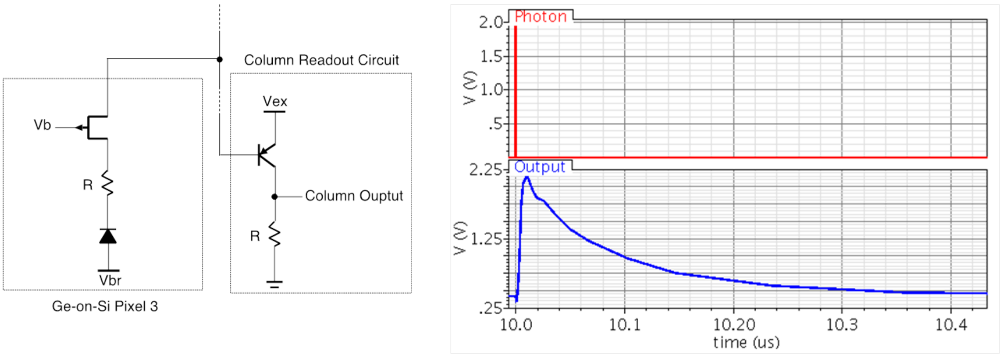

Figure 4.4: JFET-resistor type Ge pixel and PNP common-emitter-amplifier readout circuit (left), simulation result (right).

4.1.4 4×4 array implementation

All the three pixel designs have been implemented in DIMES03 process at TUDelft DIMES cleanroom [78]. A full layout of the chip and a full array photomicrograph are shown in Figure 4.5 and Figure 4.6, respectively.

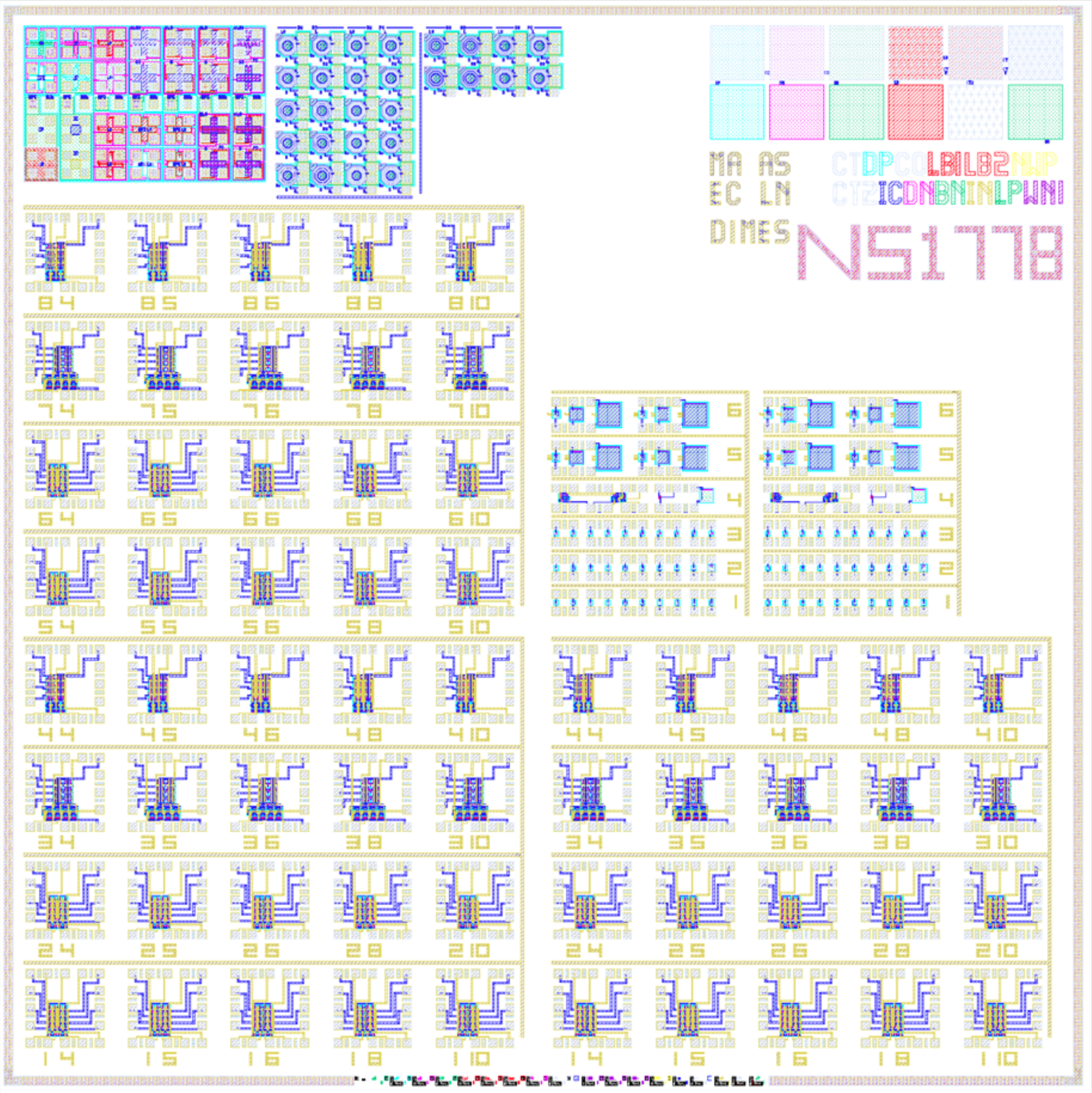

Figure 4.5: Full chip layout of different 4 × 4 Ge SPAD arrays.

4.2 Ge-on-Si 300×1 APD array

In the previous chapters, the process for selective epitaxial growth of high-quality crystalline Ge on Si substrates was introduced combined with a novel procedure for fabrication of ultrashallow p^+n Ge diodes on Si substrates [84]. The process flow has been described in section 2.3.2. We also have previously shown that such devices have electrical characteristics with very low dark currents in comparison with literature and can operate even in Geiger-mode for NIR sensitivity [28].

In this section, we proceed with utilization of this process in high-yield and reproducible detector arrays for NIR imaging (Figure 4.7). Specifically, a 300×1 Ge-on-Si APD array is designed and fabricated using two different photodiode sizes of either $6\times6\ \mu m^2$ or $26\times26\ \mu m^2$.

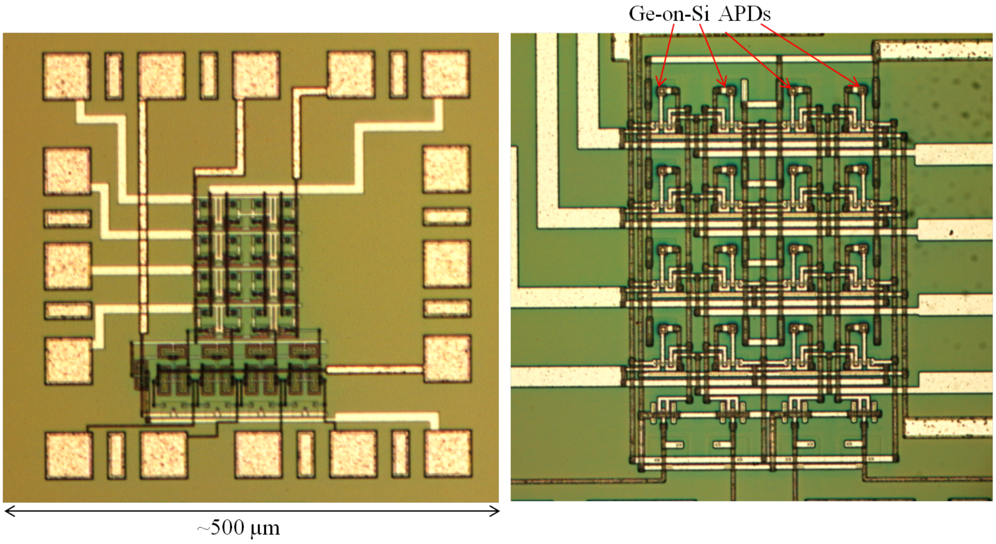

Figure 4.6: Photomicrograph of a 4 × 4 Ge SPAD pixel array.

The basic APD processing is extended for the first time with a module for achieving front-side illumination. The processing is fully CMOS-compatible and even with this extra processing step, the detectors in the array display a yield close to 100% as well as very uniform optical and electrical characteristics over the array.

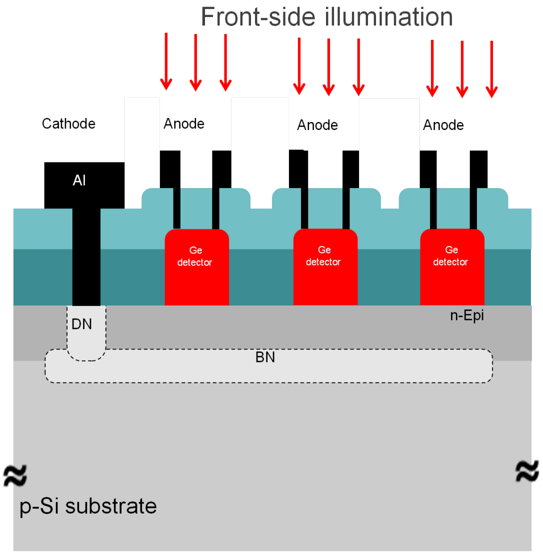

Figure 4.7: Schematic of Ge-on-Si Line array.

4.2.1 Ge-on-Si Line array design

The process flow for the fabrication of a PureGaB Ge APD array on a Si substrate was developed in Prof. Lis Nanver's group in Delft. The process is illustrated in Figure 4.8. If p-type Si wafer is used, buried n-layer is required to make cathode contact. Therefore, all the anode and cathode contacts can be put in front/top side. Otherwise, if n-type Si wafer is used, the substrate will became the cathode and the fabrication process is easier. Thus, the buried n-layer is not required and the cathode contact will be all the back side.

On top of the wafer, a 30 nm thermal SiO_2 is grown, followed by an LPCVD SiO_2 layer deposition with a thickness of ~ 1 μm (Figure 4.8 (a)). The SiO_2 layer is patterned and etched on the Si surface by the mask that defines the Ge photodiode positions in 300 × 1 arrays.

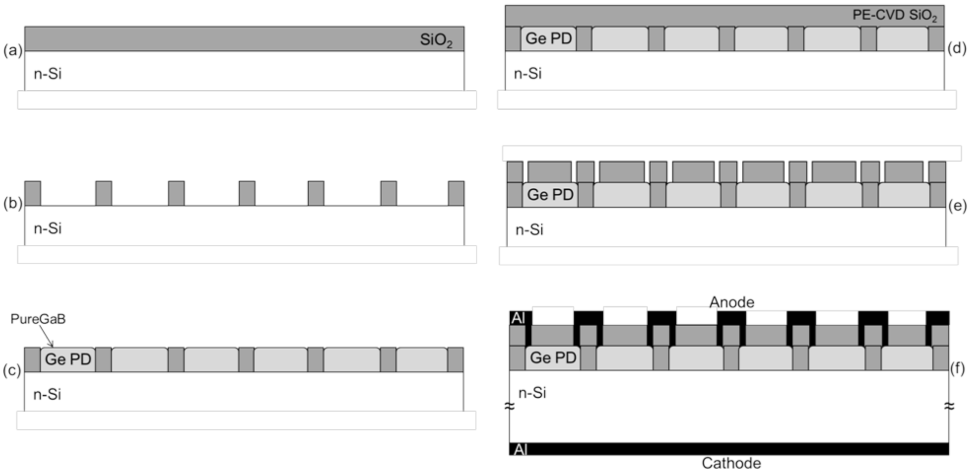

Figure 4.8: Schematic process flows for the fabrication of PureGaB Ge-on-Si photodetector arrays.

Figure 4.9 illustrates the top-view cells of this design and the fabricated photodiode arrays after metallization. This design consists of two types of arrays: one with 6×6 μm^2 APDs (Figure 4.9 (left)) and the other with 26×26 μm^2 APDs (Figure 4.9 (right)). A set of two 5μm-wide lines are also patterned around the whole array as shown in Figure 4.9. The purpose of these extra line-windows to the Si is to prevent the Germanium layer that is deposited and moving across the SiO_2 from reaching the array windows [73]. Such undesirable "loading effects" can otherwise lead to very non-uniform deposition across the array for Ge and As atoms. Moreover, nucleation of Ge on the SiO_2 surface is also counteracted by increasing the surrounding open Si area. The new design delivers a uniform and completely selective Ge growth on Si surface and the fill factor for the 26×26 μm^2 APD array can be made up to 95%.

In this process, before loading the wafers in the CVD reactor for Ge growth, they are dipped in HF 0.55% to remove the native oxide on the Si surface for 4 minutes. Moreover, in the CVD reactor, before the main processing cycle, a 4-minute baking step at 850°C is used to ensure that the Si is completely free of native oxide. The Ge APD growth process then starts by first depositing less than 100 nm As-doped Ge at 400°C and then around 900 nm intrinsic Ge at 700°C at a pressure of 20 Torr. The precursor gases used for Ge and As-doping are GeH_4 and AsH_3, respectively. Without interrupting the process or breaking the vacuum, a nm-thin layer of Ga is then deposited at 400°C using the TMGa bubbler system, followed up by a nm-thin

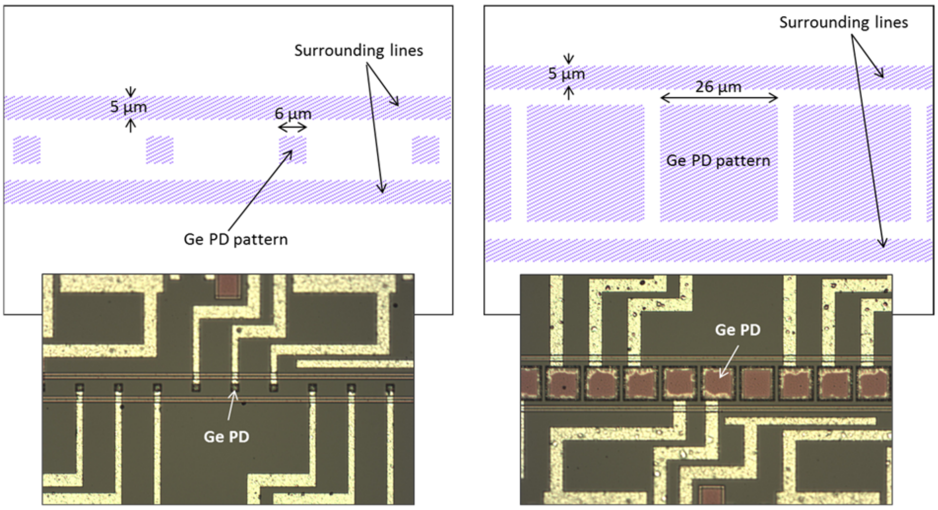

Figure 4.9: Top-view cell of the Ge APD design (top) and the microscopic-view of the fabricated arrays (bottom) with two sizes of 6 × 6 μm^2 (left) and 26 × 26 μm^2 (right).

layer of B at 700°C using B_2H_6 precursor gas to form the so-called PureGaB layer. The PureGaB layer has two main functions: 1) the Ga layer forms an ultrashallow p^+-region on the Ge thus creating the p^+n junction, and 2) the B layer forms a barrier layer that protects the Ge/Ga surface from oxidation when the wafer is removed from the reactor. This ensures a good metal contact while also protecting the APD junction from metal spiking [84].

The process then continues with a uniform deposition of 800-nm-thick SiO_2 over the wafer performed in a plasma-enhanced chemical vapor deposition (PECVD) system. This SiO_2 layer is then patterned and etched to create access to the perimeter of each photodiode as shown in Figure 4.8 (e). Subsequently, a 675 nm Al/Si (1%) is deposited on both front and back sides of the wafer and the front side is patterned in a manner to give individual electrical contact to each photodiode. The metal in the central part of the Ge device is removed to maximize the sensitivity for front-side illumination as shown in Figure 4.8 (f).

4.2.2 Electrical characterization

The I-V characteristics of the array are shown in Figure 4.10 for both sizes of 6 × 6 μm^2 and 26 × 26 μm^2. The variation of the dark current in both cases is found to be less than 500 pA. This analysis shows the high-yield of this technology: up to 99% and 100% of the measured devices were functional, for the 6 × 6 μm^2 and 26 × 26 μm^2 APD-size arrays, respectively. This improvement in uniformity as compared to previous designs originates from a better control of the Ge deposition with new design that includes deposition in lines around the array. As explained before, these lines can minimize any loading effects and non-uniformity of growth-rate and in-situ As-doping. The corresponding ideality factors for both types of APDs were extracted to be 1.02 for 6 × 6 μm^2 and 1.1 for 26 × 26 μm^2.

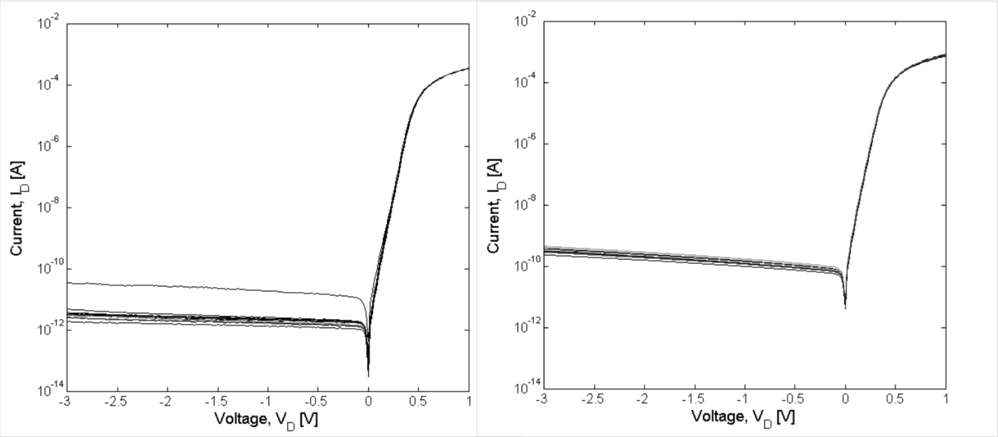

Figure 4.10: I-V characteristics of the Ge APDs across the array for two designs with the photodiode sizes of 6×6 μm^2 (left) and 26×26 μm^2 (right).

4.2.3 Optical characterization

The photocurrents of the PureGaB Ge APDs for both sizes of the 6×6 μm^2 and 26×26 μm^2 have been measured at room temperature and the results for two different light-exposure conditions are shown in Figure 4.11 when exposed either to visible light of high intensity or to light sets of not-visible infrared light sources with a central wavelength at 950 nm. From Figure 4.11 it is possible to conclude that for both APD sizes the sensitivity at higher wavelengths increases with respect to the visible wavelengths.

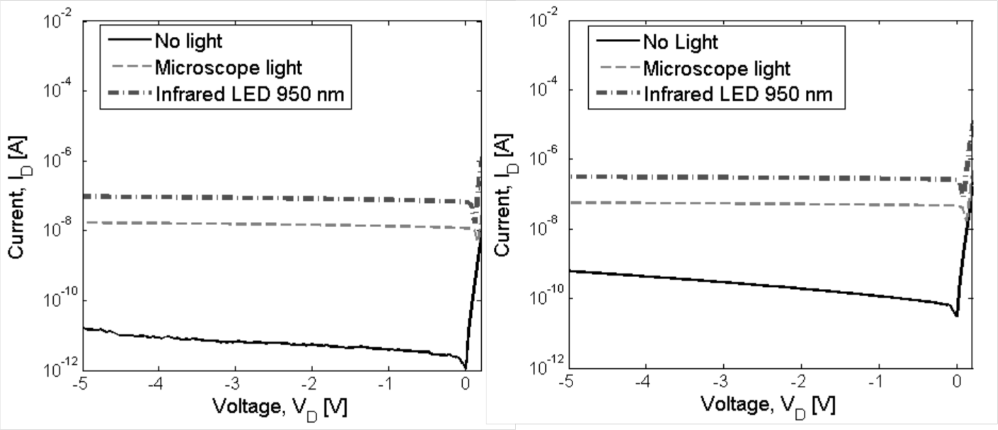

Figure 4.11: Reverse bias I-V characteristics of the Ge APDs at 3 conditions for two designs, (left) 6×6 μm^2, and (right) 26×26 μm^2.

To better understand this behavior, a room temperature study was performed on the 6×6 μm^2 PureGaB Ge APDs and the PureB Si APDs that were fabricated in a similar process for front-side illumination as explained in [85]. The summary of a comparison between these two devices is presented in Table 4.1. The dark currents and photocurrents were measured at a reverse bias voltage of 3 V. The dark current of Si APDs is almost 3 decades lower than that of Ge

APDs for the same size. This behavior is to be expected because the defect density in the deposited Ge APDs is higher and the bandgap is lower than the Si substrate. However, the photocurrent of the Ge APDs is about a decade higher than that of Si APDs. Also the sensitivity of the Ge APDs to infrared light (950 nm LED light) is more than a decade higher as compared to that of Si APDs. From this analysis one can conclude that Ge APDs have a wider wavelength range of light absorption in NIR spectral range and are significantly more sensitive at higher wavelengths at a cost of moderately higher noise.

Table 4.1: Comparison of light sensitivity of the Ge and Si APDs fabricated with PureGaB technology.

Device	APD size $[\mu m^2]$	Ideality factor	Dark current $[A]$	Visible light photocurrent$[A]$	Infrared 950 nm photocurrent$[A]$
PureGaB Ge APD	6×6	1.02	6.72×10^{-12}	1.60×10^{-8}	8.95×10^{-8}
PureB Si APD	6×6	1.06	1.0×10^{-14}	4.63×10^{-9}	5.29×10^{-9}

For further evaluation of the sensitivity, the photocurrent of the 26 × 26 μm^2 PureGaB Ge APDs was measured at room temperature over the entire array at different wavelengths in the NIR spectrum using a monochromator with a light-beam spot that was considerably larger than that of the APD area. This photocurrent was compared with the photocurrent of a reference Ge diode with an active area of 10×10 cm^2 (much larger than the light-beam spot) for which the quantum efficiency (*QE*) was known for the applied range of visible to NIR wavelengths. The ratio of PureGaB Ge APD photocurrent to the reference photodiode photocurrent (I_D/I_{ref}) is plotted in Figure 4.12 for a reverse bias voltage of 1 V. The significant increase of this value for wavelengths above 1100 nm conservatively indicates the high-sensitivity of PureGaB Ge APDs in NIR spectral range.

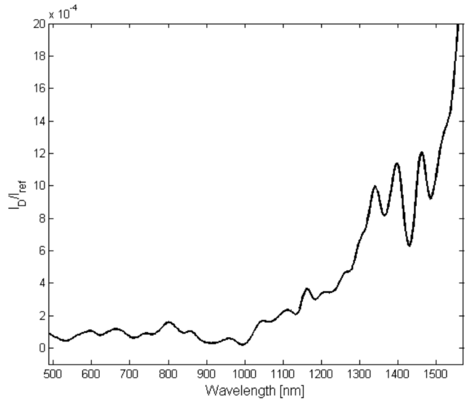

Figure 4.12: I_D/I_{ref} photo-response of the 26 × 26 μm^2 PureGaB Ge APD in the NIR spectrum at reverse bias voltage of 1 V.

4.3 Ge-on-Si Photomultiplier line array (GePM)

Silicon photomultipliers (SiPMs) are used today in a variety of applications, including time-of-flight imaging, positron emission tomography, fluorescence microscopy, to name a few [86]. The SiPM sensitivity is optimized for the visible range and usually peaks at 450-500 nm [87]. In this section, a Germanium photomultiplier (GePM) integrated on Si is proposed that is capable of operating in avalanche mode with peak sensitivity at 850 nm and a peak optical gain at 940 nm.

4.3.1 Device fabrication and structure

The devices are fabricated on Si (100) wafers using the PureGaB Ge-on-Si process methods described in [28, 88]. The n-doped Ge is grown epitaxially at 700°C in a CVD reactor with a pressure of 80 Torr, using a 2% diluted GeH_4 and 0.7% AsH_3 as the precursor gases, followed in-situ by a PureGaB deposition. The Ga forms the p^+-anode region on the Ge and the B is a barrier against oxidation and spiking of the further-deposited PVD Al interconnect layer. The cathode is connected via a buried n^+ layer in the Si. As a last step, the photosensitive junctions are exposed by means of selective etching of the Al layer to the oxide covered PureGaB. In Figure 4.13 the structure is shown schematically along with a TEM micrograph that corresponds to the cross-section, and a SEM photo of a 2D array of 5×5 μm^2 PureGaB Ge photodiodes.

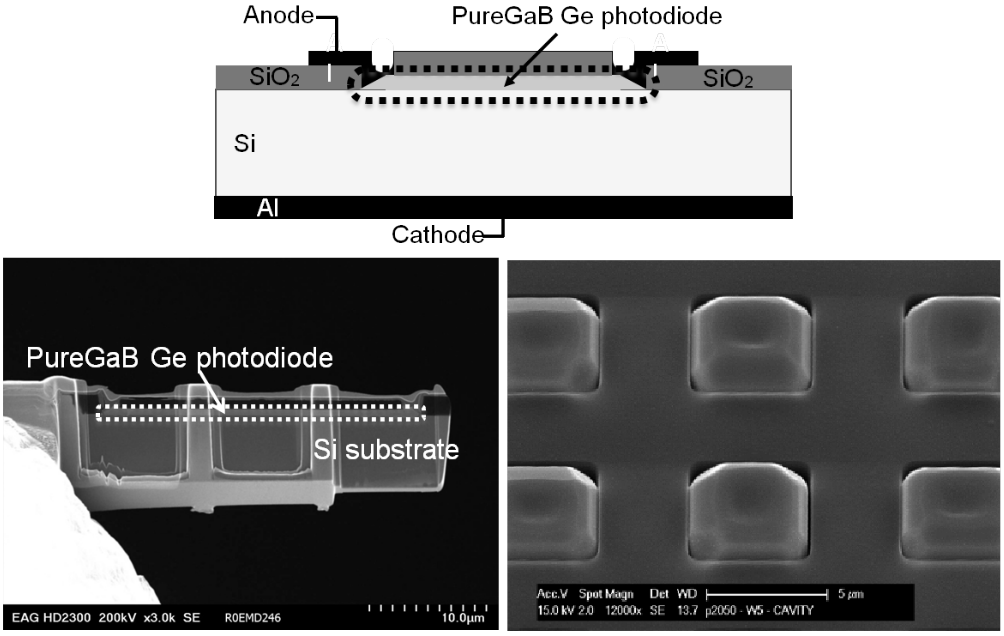

Figure 4.13: Schematic cross section (top) and TEM (bottom-left) of a PureGaB Ge-on-Si photodiode; SEM of a 2D array of 5×5 μm^2 PureGaB Ge photodiodes (bottom-right).

The basic photodetector processing is fully CMOS-compatible and extended with a module for achieving front-side illumination. The detectors in the array, even with this extra processing, display very high yield as well as very uniform optical and electrical characteristics over the array. The arrays were designed with 3 different pixel geometries: (1) a single APD 26 × 26 μm^2, (2) a 2×2 array (quad) of 12 × 12 μm^2 Ge diodes, and (3) a 4×4 array (hexa) of 5 × 5 μm^2 Ge diodes. The pixels all have the same total area of 26 × 26 μm^2 but the actual Ge area is decreased from 676 μm^2 to 400 μm^2 and the Ge perimeter increases from 104 μm to 320 μm (Table 4.2).

Table 4.2: Geometrical differences the GePMs.

	No. of diodes	Diode size $[\mu m]$	Pixel total area $[\mu m^2]$	Ge diode area in pixel $[\mu m^2]$	Ge diode perimeter in pixel $[\mu m]$
Single GePM	1	26×26	26×26	676	104
Quad GePM	4	12×12	26×26	576	192
Hexa GePM	16	5×5	26×26	400	320

In Figure 4.14 a top view of all the fabricated structures is shown along with a TEM micrograph of the quad GePM. An overview of the geometrical parameters of the different GePM pixels is given in Table 4.2.

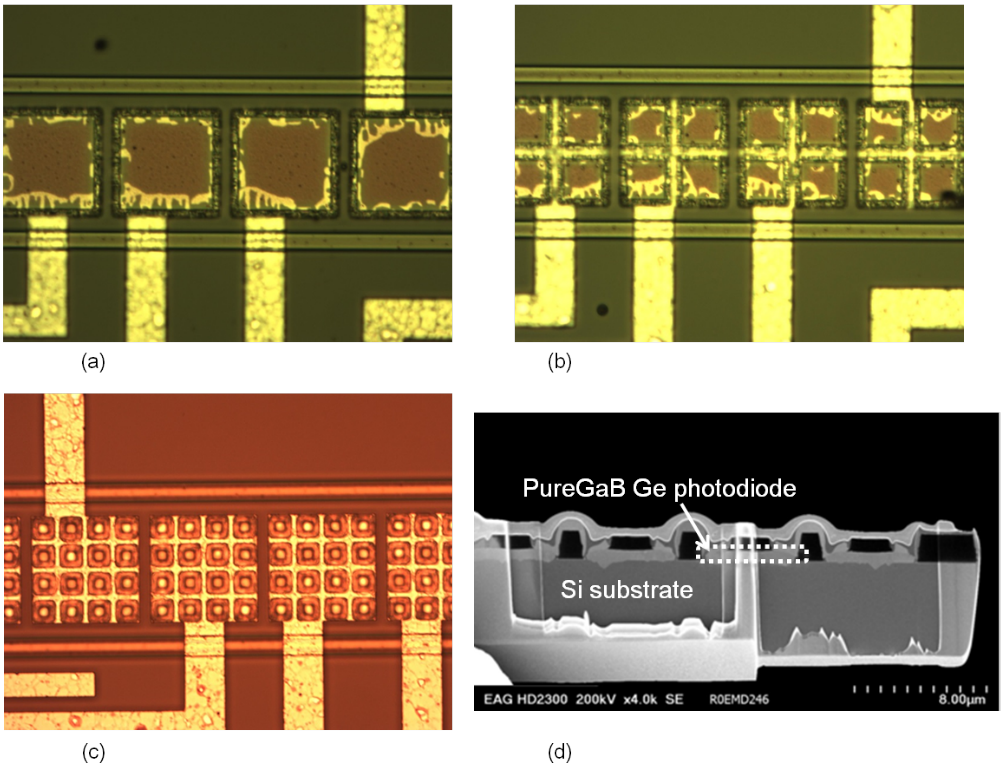

Figure 4.14: Optical images of (a) a PureGaB Ge single-diode pixel, (b) a four-diode quad pixel, (c) a sixteen-diode hexa pixel, and a TEM image of a quad pixel (d).

The 300×1 arrays of PureGaB GePMs are integrated on substrates of 2-5 Ω-cm n-type (100) Si wafers. The fabrication process has been described in section 4.2.1. Around the whole array, a set of two 5 μm-wide lines are also patterned to getter the Ge deposited on the SiO_2 and prevent excessive amounts from reaching the GePM deposition windows. These lines are minimizing any loading effects and growth-rate non-uniformity also of the in-situ As-doping [88].

All arrays displayed high-quality photodiodes with very high-yield over the array. In the following section and also the next chapter, the electrical and optical properties of the fabricated GePM arrays are discussed and compared.

4.3.2 Electrical characterization

Figure 4.15 shows the I-V characteristics of the three GePMs at room temperature. The dark current is less than 1 nA when biased at -1 V.

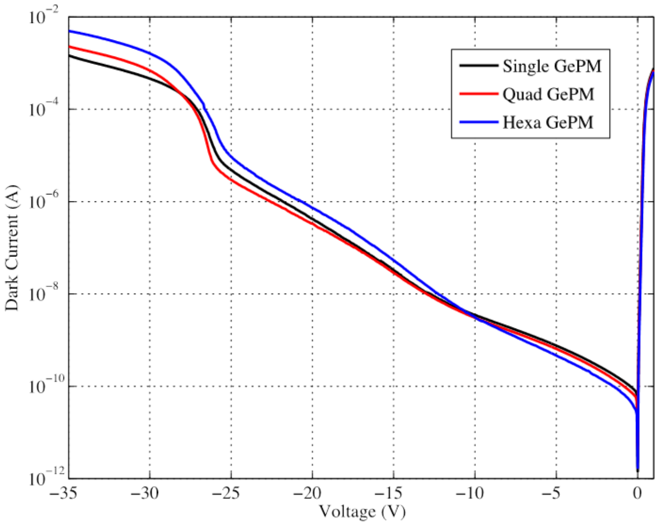

Figure 4.15: Dark current in room temperature for different GePM pixel types.

The 3 different types of GePM, with very different Ge diode areas and perimeters, all have very good electrical and optical performance. Overall, the diodes were found to be of good quality with very high-yield over the arrays of about 99%. They have about the same breakdown voltage with low spread (23.6±0.4 V), and a high maximum optical gain. In the next chapter, the electrical and optical properties of the fabricated photomultiplier arrays are completely characterized in ultra-low temperature.

5 Cryogenic Experimentation

The *cryogenic temperature* range has been defined as from -150°C (123 K) to absolute zero (-273°C or 0 K). In this temperature range, molecular motion comes as close as theoretically possible to ceasing completely. The limit temperature of around 120 K is because the normal boiling points of the main atmospheric gases, as well as of methane, which constitutes the principal component of natural gas, are below this temperature. Cryogenic temperatures are normally described in the absolute or Kelvin scale. The Celsius to the Kelvin scale Conversion can be done by adding -273 to the Celsius scale [89, 90].

Cryogenic temperatures are much lower than those experienced in normal physical processes. At these extreme low temperatures, some material properties such as strength, thermal conductivity, ductility, and electrical resistance are changed in both ways of theoretical and commercial importance. At cryogenic temperatures, because heat is generated by random motion of molecules, motions are small and materials are as close to a static and highly ordered state as possible. Thus, a low-temperature system can be defined as a system, in which a little addition of heat produces a large change in entropy, i.e. a large change in its range of possible microscopic configurations. The average thermal energy of a particle in a system in equilibrium at temperature T is expressed by Boltzmann ($E = K_B T$). The Boltzmann constant (K_B) is around 10^{-5} eV or 10^{-23} J. Therefore, 1 K temperature change is equivalent to a thermal energy of $1 \times K_B$ per particle.

Ionization energy of the dopants typically determines the lower temperature limit. Dopants require certain energy, usually thermal energy, to ionize and produce carriers in the semiconductor. If the temperature is too low, the ionization will not generate sufficient carriers. This condition is called “freeze-out”. For example, Si (dopant ionization energy around 0.05 eV) freezes out at about 40 K and Ge (ionization energy around 0.01 eV) at about 20 K. As a result, Ge devices in general can operate at lower temperatures than Si devices [91].

Nevertheless, there are additional effects that can allow devices to operate below their “freeze-out” temperature. If a semiconductor is doped to a certain concentration, it can reach to a condition in which the dopants require no energy for ionization. As an example, for n-GaAs this happens at a moderately low doping concentration ($\sim 10^{16}\ cm^{-3}$) that is usual in standard devices. For Si, degenerate doping requires much higher concentration ($\sim 10^{19}\ cm^{-3}$) [91]. Therefore, in the device design for low temperature, it is important to have sufficient doping concentration to avoid freeze-out.

In this chapter, the designed Si SPAD devices and Ge-on-Si APD line arrays are characterized both electrically and optically at cryogenic temperatures down to 77 K by cooling with liquid nitrogen.

5.1 Temperature dependence of semiconductor properties

Temperature has an effect on most semiconductor parameters. Some properties such as the energy gap and activation energies for impurities will change slowly with the temperature; they are more dependent on binding types and the short-range order in the material. The properties that depend on the excitation of the lattice vibration spectrum may change widely, for example, the specific heat and transport properties depend on scattering and excitation of carriers [92].

One of the most important parameters in semiconductor materials is the bandgap energy. The bandgap energy of most semiconductors increases with decreasing temperature. Temperature impacts the bandgap of a semiconductor in an inversely proportional fashion. In Equation (5.1), the energy band gap (E_g) is expressed as a function of temperature (T) [93].

$$E_g(T) = E_g(0) - \frac{\alpha T^2}{T+\beta} \tag{5.1}$$

where $E_g(0)$ is the band gap energy at absolute zero Kelvin in the given material, and α and β are material-specific constants, shown in Table 5.1. By increasing the bandgap, higher energy is required to break the bond. This means that lower dark current and dark count noise can be achieved.

Table 5.1: Energy gap equation constants for Si, GaAs, and Ge [93].

Material	$E_g(0)$ (eV)	$\alpha_E(eV/K)$	$\beta_E(K)$
Si	1.170	4.73×10^{-4}	636
Ge	0.7437	4.77×10^{-4}	235
GaAs	1.519	5.41×10^{-4}	204

Another parameter is the conductivity of a material. The conductivity of a semiconductor is given by Equation 5.2 [94], where μ_n and μ_p are the mobility of the electrons and holes, and n

and p refer to the density of electrons and holes.

$$\sigma = q\left(\mu_n n + \mu_p p\right) \tag{5.2}$$

In a doped semiconductor, majority carriers are greatly more numerous than minority carriers: Thus, Equation 5.2 can be reduced to a single term involving the majority carrier of n or p. Two factors have effect on conductivity: the concentration of free carriers and their mobility. Both mobility and carrier concentration in a semiconductor are temperature dependent. Therefore, the conductivity as a function of temperature can be expressed by Equation 5.3.

$$\sigma = q\left(\mu_n(T) \times n(T) + \mu_p(T) \times p(T)\right) \tag{5.3}$$

The mobility of electrons and holes can be affected by two basic types of scattering mechanisms: lattice scattering and impurity scattering. The lattice vibrations cause a decrease in mobility with increasing temperature. Moreover, the carrier mobility is affected by the presence of charged impurities. Crystal defects such as ionized impurities can cause impurity scattering. At lower temperatures, carriers move more slowly, and they have more time to interact with charged impurities. Therefore, with decreasing temperature, the mobility decreases and impurity scattering increases; this is the opposite of the lattice scattering effect.

Thus, the total mobility is the sum of two scattering effects. The approximate temperature dependence of lattice scattering on mobility is $T^{-3/2}$, while the temperature dependence of mobility due to impurity scattering is $T^{+3/2}$. Impurity scattering is typically seen for high doping levels and also at very low temperatures.

The other parameter, carrier concentration in a semiconductor, is also affected by temperature. The intrinsic carrier concentration is given by Equation 5.4, where it is dominated by the exponential temperature dependent component.

$$n_i(T) = 2\left[\frac{2\pi kT}{h^2}\right]^{3/2}(m_n^* m_p^*)^{3/4} exp(\frac{-E_g}{2kT}) \tag{5.4}$$

The total carrier concentration also includes space-charge neutrality as shown in Equation 5.5.

$$n(T) = N_D^+(T) - N_A^- + \frac{n_i^2(T)}{n(T)}, p(T) = N_A^-(T) - N_D^+ + \frac{n_i^2(T)}{p(T)} \tag{5.5}$$

Figure 5.1 illustrates the temperature dependence of electron concentration for doped silicon with 10^{15} donors/cm^3. At very low temperature (larger *1/T*), intrinsic electron-hole pairs are negligible and donor electrons are bound to donor atoms. This region is knows as *ionization* of *freeze-out* region. By increasing the temperature, ionization will be increased. At the extrinsic (or saturation) region all dopants have been ionized and an increase in temperature cannot increase the carrier concentration. In this region, $N_D^+(T) = N_D$, $N_A^-(T) = N_A$, and $n_i(T) \ll \mid N_D - N_A \mid$. At higher temperature (lower 1/T) the thermally generated intrinsic carriers are much larger than the dopants ($n_i(T) > \mid N_D - N_A \mid$), and the carrier concentration increases with the temperature.

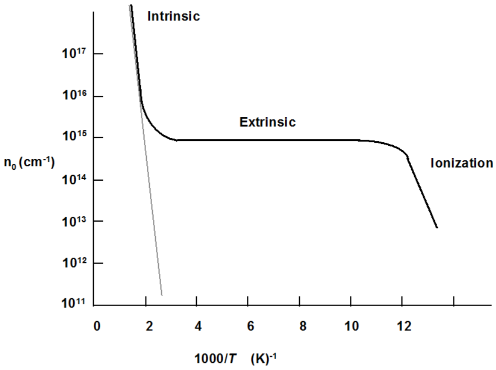

Figure 5.1: Carrier concentration versus reciprocal temperature for silicon [94].

5.2 Cryogenic setup

There are some ways to reach low temperatures for cryogenic experiments, using cryogens or mechanical coolers. The principle of liquid cryogens in cooling cryostats is the same as the ancient technique of using ice blocks to keep food cold, the environment heat melts the ice, keeping a constant temperature until melting of all the ice [95]. In a same way, liquid cryogen evaporation maintains the temperature at the boiling point of the cryogen. Mechanical coolers usually consist of two components, a room temperature compressor and an expansion chamber that are linked by plumbing. The working principle is to compress helium at room temperature in the compressor, then send it into the cryostat that by expansion it produces cooling. The main drawback of mechanical coolers is their vibration. This system is particularly attractive for remote location applications [95].

In this thesis, cooling with cryogens has been used for cooling the experimental setup. Cryogens provide cooling in two ways, using heat by absorbing latent heat to evaporate the liquid, and then the heat is used in warming the gas from the boiling point to room temperature. The enthalpy change provides this heating. Helium and nitrogen are two main cryogens in use in cryogenic systems. Some properties of these two cryogens are given in Table 5.2, where the boiling point is at 1 atmosphere.

Table 5.2: Some properties of Nitrogen and Helium-4 [95].

Cryogen	Boiling point	Latent heat	Cost/Litre
Nitrogen	77 K	161 kJ/L	£0.1
Helium-4	4.2 K	2.6 kJ/L	£3

The temperature requirement determines the appropriate cryogen. If no lower than 77 K is required, then liquid nitrogen is a reasonable option. However, for cooling until 4.2 K, it is better to first cool to 77 K with liquid nitrogen, and then use helium, because liquid nitrogen is around one thousand times cheaper than helium per joule of latent heat.

To cool the designed Si and Ge-on-Si chips, a continuous-flow cryostat system has been used for achieving low temperatures with a low consumption of liquid gas. This system contains several sub-components, as shown in Figure 5.2, which influences the cooling process. The Cryogenic Probe Station (PMC150) is used for manually probing chips at low temperatures. This is implemented under vacuum conditions to be free from ice and frosting on the surface down to a temperature of 20 K. The PMC150 allows probing in a vacuum chamber with Probe-Heads on wafers and substrates up to a diameter of 200 mm.

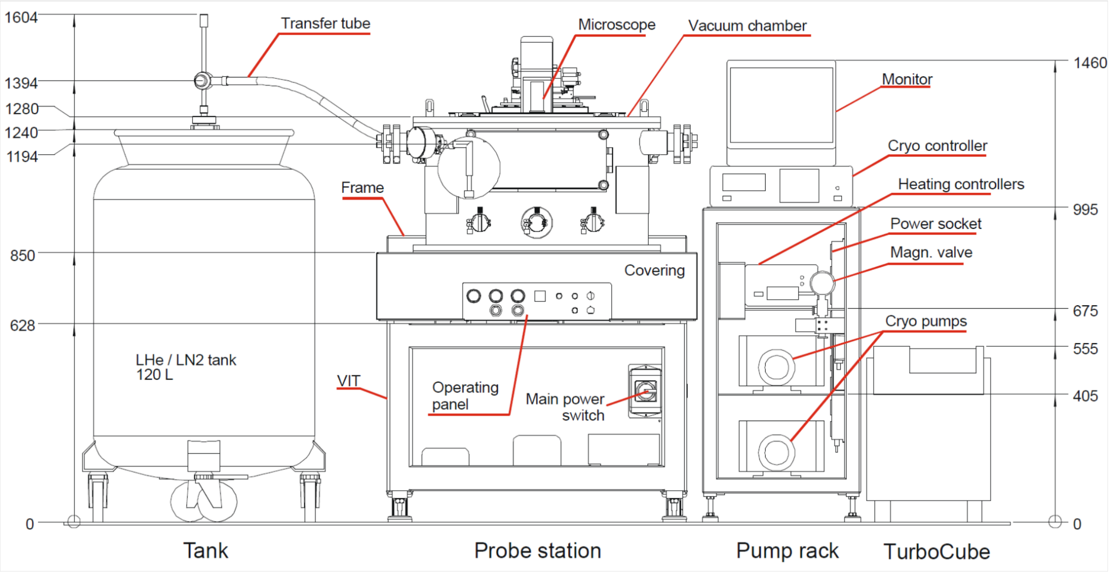

Figure 5.2: Block diagram of a Cryogenic Prober.

A storage dewar (or tank) is used to keep liquid cryogens (liquid helium or nitrogen). The storage dewar continuously refills the cryostat by a steady flow as the cryogen boils. Controlling the temperature of samples is typically performed by managing the flow rate of cryogen into the cryostat accompanied with a heating wire attached to a temperature control loop.

The prober system is an enclosure, which can be cooled to very low temperature. The system consists of a micro-miniature refrigerator (inside the small metal vacuum enclosure, which contains a window on top to see the semiconductor samples), a tank of high-pressure nitrogen or helium for the refrigerating fluid, and a vacuum pump and manifold. The device uses the Joule-Thompson expansion of a high-pressure gas for cooling to liquify the gas in a small reservoir underneath the mounted sample. The fridge is fabricated of a laminated set of glass slides, which has micro-channels etched into the glasses to provide a serpentine path for the gas to proceed through a heat exchanger [96].

The semiconductor sample is mounted on a cold mount at the end of the refrigerator with thermal grease, which makes excellent thermal contact between the sample and the fridge. The sample can be cooled to ~77 K from room temperature in about 3 hours. The refrigerator also has a built-in heater (thin wires) to heat the sample or control the temperature stability. The cooling system and measurement instruments are shown in 5.3.

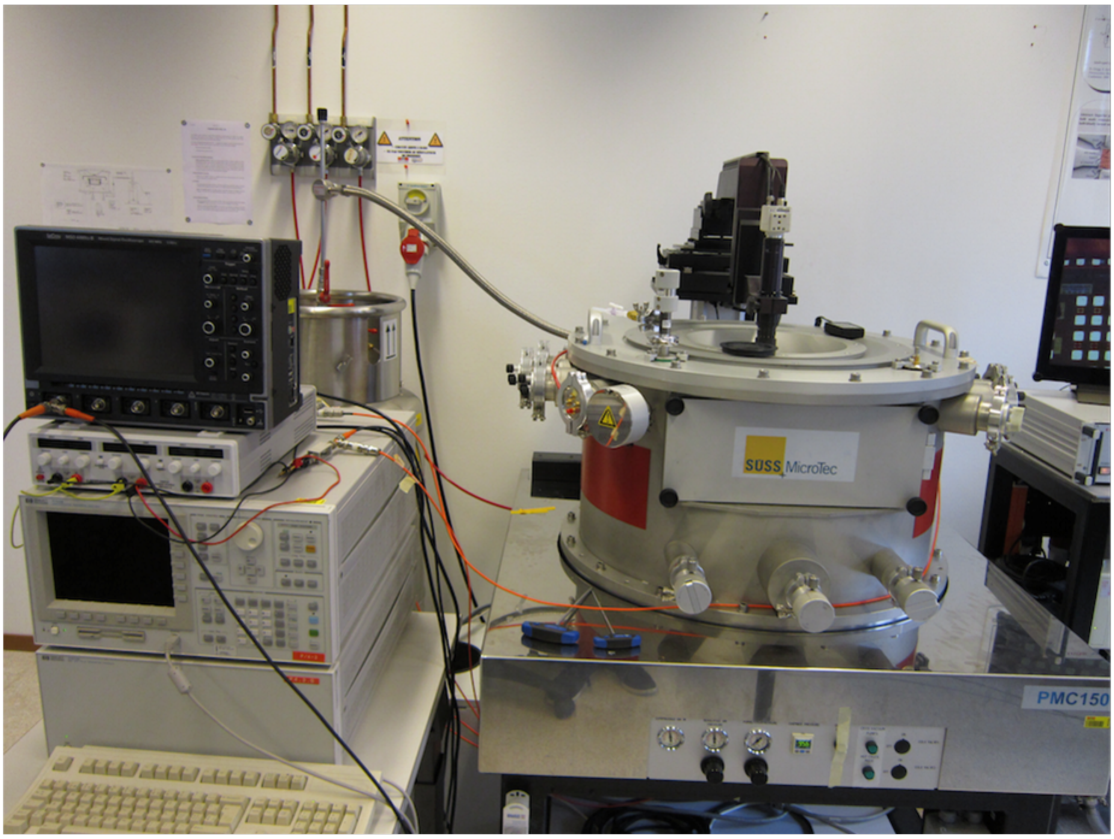

Figure 5.3: Cooling system and measurement instruments.

5.3 Si SPAD measurements

An increasing number of manufacturers offer low temperature cooling of CMOS microprocessors to enhance their performance. Another reason for low temperature operation of microprocessors is to keep the temperature of the microprocessors within accepted limits, due to increased power consumption in scaled technologies. Theoretically, all commercial computers have been designed to operate at temperatures above ambient [97].

Moreover, lowering the temperature will decrease thermal events and undesired noise. The low temperature operation of the devices has also the advantage of significantly increasing the interconnect conductivity. In general, cooling has advantages such as leakage reduction, performance enhancement, and reliability improvement of electronic devices. On the other hand, the cooling has some disadvantages such as extra power consumption during the startup and normal operation [97]. In this section, the effect of cooling silicon SPAD devices is reported.

5.3.1 Breakdown voltage

The breakdown voltage is temperature dependent. Increasing the temperature can decrease the impact ionization due to enhanced photon scattering [98]. Decreasing the impact ionization rate increases the breakdown voltage. There is a linear relationship between temperature and breakdown voltage (V_{BD}) as given in Equation 5.6.

$$\rho = \frac{\Delta V_{BD}}{\Delta T} \tag{5.6}$$

The value of ρ is strongly dependent on the material. The breakdown voltage versus temperature is shown in Figure 5.4. Both SPAD1 and SPAD_RED behave as expected; the breakdown voltage is a linear function of the temperature. In the diode with smaller breakdown voltages, the tunnelling effect is more dominant. In these devices the breakdown voltage decreases faster with the temperature [99].

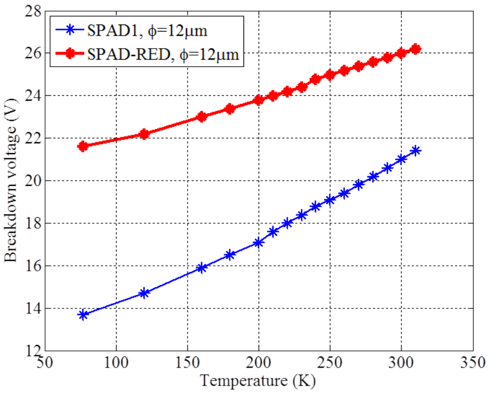

Figure 5.4: Breakdown voltage temperature dependence of Si SPADs from 310 K to 77 K.

5.3.2 DCR versus temperature

Both device types, SPAD1 and SPAD_RED, with diameter of 12 μm were measured in the temperature range of 77-310 K at different excess bias voltages (V_{ex}) from 1 V to 6 V. As the breakdown voltage of SPADs is changing with the temperature, the bias voltage should be adjusted to keep the same excess voltage over the entire temperature range. The dark counts rate as a function of temperature is shown in Figure 5.5.

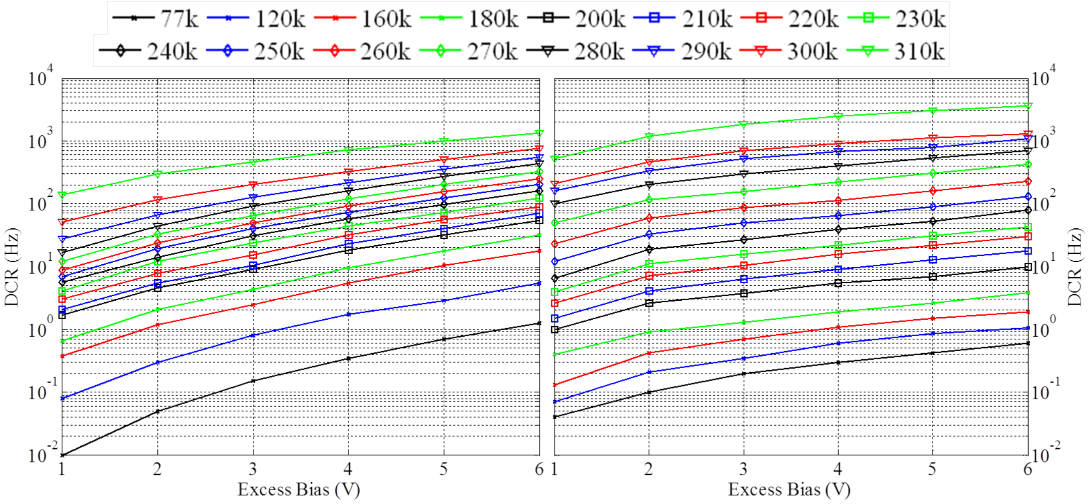

Figure 5.5: Dark count rate (DCR) for the 12μm active diameter device, (left) SPAD1, (right) SPAD_RED.

The DCR curves show steeper descent for SPAD_RED due to higher thermal generation. In low temperature, the DCR is dominated by tunneling effect (either trapped assisted or band-to-band tunneling). Although, at very low temperatures, the tunneling generation is at a limit, both devices have very low DCR (less than 1 count per second) at 77 K. Additionally, the dark count rate has an almost exponential rise with the excess bias. It confirms that the thermal generation rate is strongly enhanced by higher electric field.

5.3.3 Activation energy in low temperature

Increasing the temperature causes higher ionization of impurity atoms, i.e. both electron and hole concentrations will be increased because of electron excitation from the valance band to conduction band (electron-hole generation). This increase is exponential w.r.t. growing temperatures and reduced bandgap energy (as was given by Equation 3.2). An analysis of the activation energies can be used to understand the type of generated currents and defects.

The defects and traps are normally initiated in the fabrication process. Because dark current and dark count rate are proportional to T, the activation energy (E_a) can be calculated from the Arrhenius plot [19]. Figure 5.6 plots ln(DCR) obtained for SPAD1 and SPAD_RED as a function of 1/T for excess bias voltages of 2 V, 4 V, and 6 V. The thermal activation energy is extracted by linear fitting. In the graph, three linear sections can be identified. The activation energy is decreasing drastically with the temperature. At very low temperatures, E_a is very small. It means higher tunneling effect than generation-recombination is present in this region. Moreover, the higher variation of E_a in SPAD1 indicates a higher band-to-band tunneling effect.

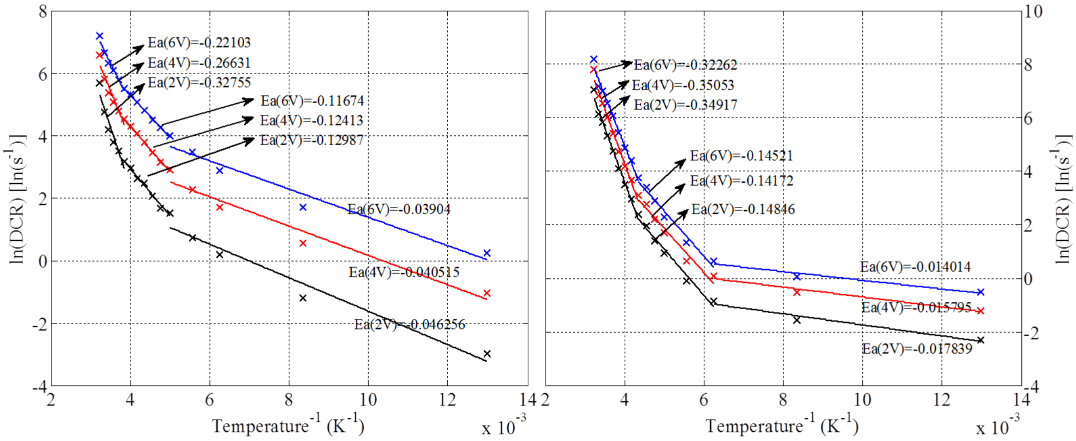

Figure 5.6: Arrhenius plot of DCR from 77 K to 310 K for the 12μm diameter, (left) SPAD1, (right) SPAD_RED.

Additionally, most degradation mechanisms in electronic devices have a thermal activation energy component that follows the Arrhenius correlation. In general, lowering the temperature has effects on degradation mechanisms such as electromigration, inter-diffusion, corrosion, and improving the reliability of the overall system. As the degradation rate decreases exponentially with temperature, improvement of reliability is expected by orders of magnitude [97].

The reliability is measured by the mean time to failure (MTTF). For thermally activated mechanisms, MTTF is proportional to a temperature dependent term expressed by the Arrhenius plot as shown in Equation 5.7 [100], where T_0 is the operating temperature and T_R is the reference temperature.

$$MTTF \propto exp\left[\left(\frac{E_a}{k}\right)\left(\frac{1}{T_0}-\frac{1}{T_R}\right)\right] \tag{5.7}$$

This equation indicates that the MTTF decreases when E_a is decreased. Due to the very low activation energy at low temperature as seen in Figure 5.6, operating at 77 K can improve the MTTF drastically.

5.4 Cryogenic characterization of Ge-on-Si line array

The Ge-on-Si process used in this thesis employs a CVD technique for selective growth of Ge on Si substrates that results in low defect crystalline Ge in tens of microns large window sizes. By this method, most of the defects that are generated due to the lattice-mismatch are localized at the interface of Si-Ge and disappear within the first 200 nm of growth. Because the system was adapted for merging GaAs and Si epitaxies in one reactor, the integration of good-quality crystalline intrinsic layer and GaAs doped layers on Ge could be accomplished directly after the Ge growth.

With utilization of this process in high-yield and reproducible photodiode arrays for NIR imaging, a Germanium photomultiplier (GePM) integrated on Si is proposed that is capable of operating in avalanche mode. The GePM arrays have been fabricated in 3 different types: a single APD 26 × 26 μm^2, a 2 × 2 array (quad) of 12 × 12 μm^2 Ge diodes, and a 4 × 4 array (hexa) 5 × 5 μm^2 Ge diodes, all with identical total area of 26 × 26 μm^2 but the actual Ge area is decreased from 676 μm^2 to 400 μm^2. The high quality Ge-on-Si photodiodes offers ideality and dark currents that are among the lowest values reported in the literature for any Ge diodes, to our knowledge [28], with peak sensitivity at 850 nm, and peak optical gain in avalanche mode at 940 nm.

In diodes, both forward and reverse biased characteristics are temperature dependent. These temperature properties are very important for better device design. The main temperature effect in a diode is due to the strong temperature dependence of the intrinsic concentration n_i (showed in Equation 5.4) and by the exponential temperature relationship of the diode current equation.

In this section, a comprehensive characterization of GePMs fabricated in a CMOS compatible process is described. It is shown that, for a given overall active area, small geometries yield the highest optical gains and the lowest dark current at very low bias voltage. The devices are reliably operational at a wide temperature range, from 77 K to room temperature. The spectral sensitivity of the detectors extends from visible to the telecom band with a maximum responsivity of 0.20-0.25 A/W at both 850 nm and 940 nm and a dark current below 35 $\mu A/cm^2$ and 2.5×10^{-2} $\mu A/cm^2$ at 1 V reverse bias for room temperature and 77 K, respectively. The average optical gain is over 3.18×10^6 at 77 K. The proposed detectors were fabricated in linear arrays of 300 pixels designed for applications, such as time-of-flight imaging, Raman spectroscopy, and near infrared optical tomography.

5.4.1 Dark current temperature dependence

The fabricated GePMs operate reliably at a wide range of temperatures. The current-voltage (I-V) characteristics was measured for three different GePM pixels placed on the PMC150 cryogenic chamber, using a Hewlett-Packard Semiconductor Parameter Analyzer model 4145B. Overall, the diodes were found to be of good quality with very high-yield over the arrays of about 99%. Typical I-V characteristics are shown in Figure 5.7. The dark current ranges from 1 nA at room temperature to well under 10 fA at 77 K with a reverse bias of 6 V.

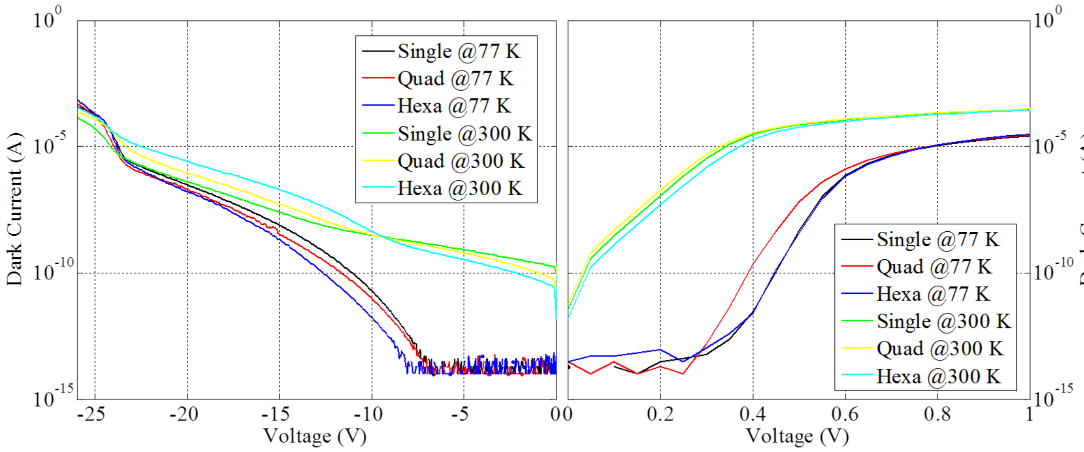

Figure 5.7: Dark current versus temperature of PureGaB GePMs (left) from 0 V to -26 V and (right) from 0 V to 1 V.

The breakdown voltage variation with temperature can be explained by the scattering of electrons and holes by phonons. The applied electric field and the magnitude of the applied electric field will give energy to charge carrier and accelerate them in the electric field, which is proportional to charge carrier mean free path across the direction of this force. The required energy gain for impact ionization should be at least equal to the bandgap energy (E_g) [101].

As can be seen in Table 4.1, the areas and perimeters of the 3 device types are quite different. In the ideal case in forward, for these vertically isolated diodes the current should be proportional to the area. However, when the I-V characteristics of a large number of devices are compared, it is clear that the geometrical effects are not decisive for the current levels. For example, in Figure 5.8 and Figure 5.9 the spread of the characteristics is displayed for the measurements at 77 K. The forward characteristics are all in the same range, although there is a clear trend towards lower values as the size of the individual diodes in the pixel decreases, i.e. the total Ge area decreases. At this low temperature the n = 2 indicates that the main origin of the current is G-R centers, the amount of which will vary from device to device but appears to be minimal in the hexa pixels with the small $5 \times 5\ \mu m^2$ diodes.

Also, the reverse characteristics show dark currents of the same level but with a lower spread in the hexa devices. These devices have a large perimeter of oxide but between adjacent diodes the depletion will encompass the whole oxide interface already at about 6 V of reverse bias. Therefore, the highest electric field will be situated at the perimeter of the pixel, which is the same for all 3 geometries. This will determine the breakdown voltage (V_{BD}), which also appears to be the same, with a small spread, for all geometries. Below a reverse bias of 6 V the dark current is seen to be very low, much less than 10 fA which is the limit of the measurement set-up.

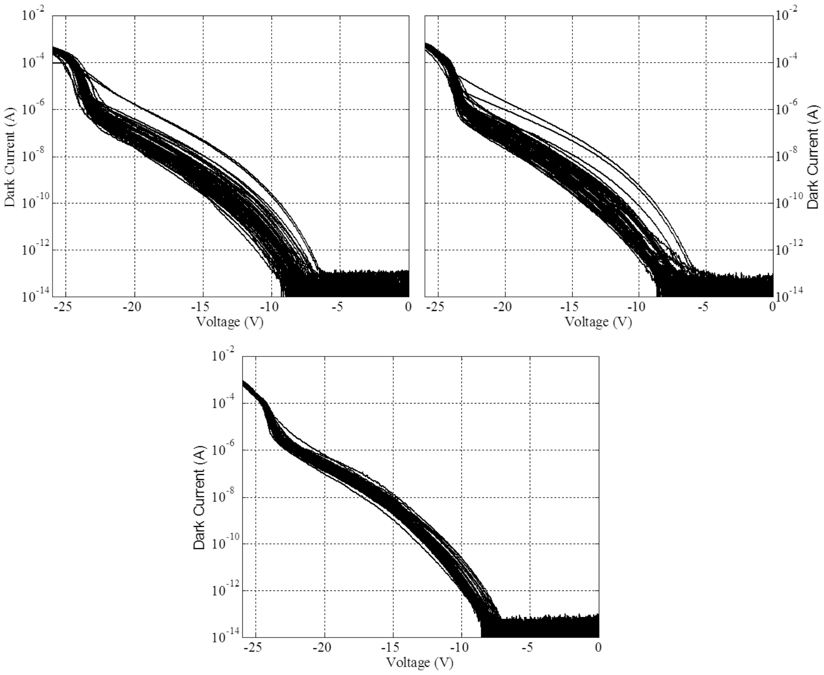

Figure 5.8: Reverse bias current spread across 70 devices measured at 77 K: (top-left) single GePM, (top-right) quad GePM, (bottom) hexa GePM..

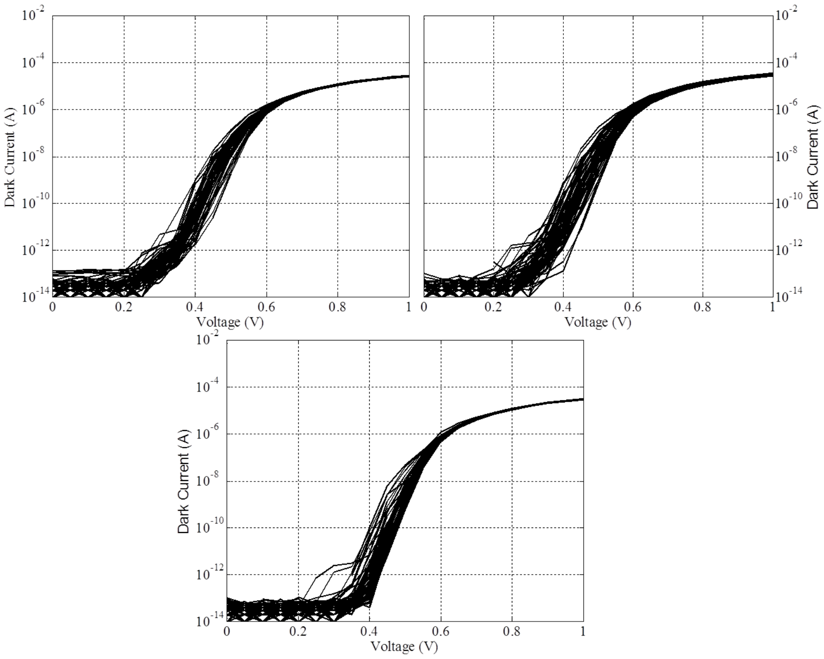

Figure 5.9: Forward bias current spread across 70 devices measured at 77 K: (top-left) single GePM, (top-right) quad GePM, (bottom) hexa GePM.

If we define the (V_{BD}) as the voltage corresponding to a minimum of 10 μA dark current [35], a breakdown voltage distribution of 23.6±0.4 V is obtained. This spread in dark current is low for a Ge-on-Si process but higher than what can be achieved in an optimally designed Si diode process where the depletion of the Si-to-oxide interface at the diode perimeter will account for most of the non-ideal currents in small micrometer sized devices. Therefore, although the outer perimeter of our Ge-on-Si pixels determines the breakdown, the oxide interface to the Si between the Ge diodes would not be expected to be decisive for the dark current level.

For the present Ge-on-Si devices the thickness of the Ge islands and their n-doping is found to be uniform for the different geometries [73]. In forward bias the termination of the depletion is on the Ge-island sidewalls. Nevertheless, there is no correlation between the spread of the forward I-V characteristics and the increasing perimeter, as the individual diode size is decreased. Therefore, it is reasonable to assume that the spread in forward bias is due to defects in the bulk Ge and not the intended structural differences in the device design.

With reverse biasing of the diodes, the defects at the Ge-to-Si interface will also play a role in the generation of dark current. The interface states at the oxide-to-Si interface are expected to be of too low to account for the measured dark current, even for the hexa pixel with a relatively large Ge diode perimeter. All in all, the spread in breakdown is most likely correlated to the variation in dark current that stems from the varying amounts of Ge-related defects. There appears to be a lower defect density for the pixels composed of the smallest diodes. For our method of growth, this effect cannot be compared to the advantages that techniques such as “Aspect Ratio Trapping” [97, 102] have when decreasing their submicron window sizes: they rely on the trapping of dislocations on the oxide sidewalls of the windows that have high aspect ratio. For the growth in our low-aspect-ratio micrometer-sized windows, several other mechanisms may influence the perfection of the crystal formation. For example, differences in the flow of the Ge-source may occur due to the different oxide-to-Si ratios in the 3 designs and the presence of the perimeter Ge-to-oxide region, most dominant in the hexa design, may influence the absorption of defects at the Ge-to-Si interface in a positive manner.

5.4.2 Ideality factor versus temperature

The ideality factor is derived from the slope of the I-V curve in the dark, and occasionally the light. The I-V characteristics of a diode can be described by Equation 5.8. The I_D and V_D are the diode current and voltage, respectively, and I_S is the saturation current that in reverse bias corresponds to the minimum dark current possible for the given junction configuration.

$$I_D = I_S\left(exp\left(\frac{qV_D}{nkT}\right) - 1\right) \tag{5.8}$$

where n is the ideality factor, k is Boltzmann’s constant, T is temperature in Kelvin. The factor "kT/q" is also known as the thermal voltage (V_{th}), and at room temperature (300 K) it is 25.9 mV. For V > 50 - 100 mV the "-1" term can be ignored. For an ideal semiconductor junction n = 1, and n = 2 for semiconductor junctions containing a high level of G-R centers.

For actual diodes, the ideality factor is a number between 1 and 2, which typically increases as the current decreases. In real devices, the saturation current strongly depends on the temperature. Also, mechanisms that change the ideality factor also impact the dark current by creating leakage currents. Taking the log of both sides of the Equation 5.8 gives Equation 5.9:

$$\ln(I_D) = \ln(I_S) + \left(\frac{q}{nkT}\right) V_D \tag{5.9}$$

If the I-V characteristics are plotted in a log-lin graph, the y-intercept is equal to the natural log of the saturation current. The slope of the line gives q/nkT and, therefore, it is proportional to 1/n. The ideality factor can either be plotted as a function of voltage or given as a single value. If it is given as a single value, the voltage range also needs to be given, because the ideality factor varies with voltage.

The corresponding ideality factors for three types of PMs are shown in Figure 5.10 from room temperature to 77 K. The ideality factors were extracted to be about 1.1 at room temperature for the 3 types of GePMs, with good uniformity across the different arrays. The ideality factors are increased to about 2 at 77 K. This is consistent with the fact that ideal current drops by decades when the temperature is lowered and generation-recombination currents will become dominant.

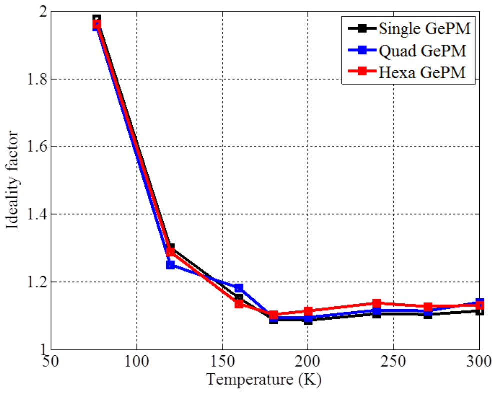

Figure 5.10: Ideality factor of GePMs for various temperature.

5.4.3 Low temperature photoresponse

For optical measurements, the GePMs were mounted in the vacuum chamber and cooled to temperatures down to 77 K. For accurate results it is important that the photodetector arrays are uniformly exposed by a field of light and then the generated photocurrent from each pixel in the array is measured (Figure 5.11). For the responsivity, measurements at several wavelengths were performed. Three lasers were used as light sources, the M660F1, M850F1, and M940F1 from THORLABS, with wavelengths of 660 nm, 850 nm, and 940 nm, respectively.

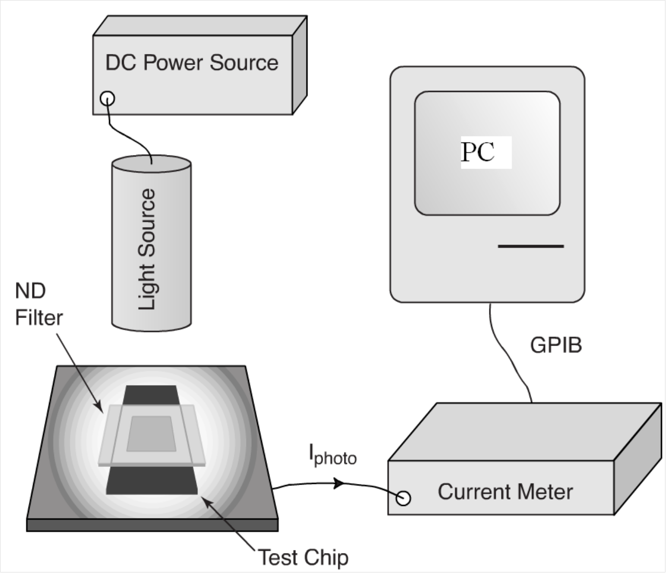

Figure 5.11: The computer controlled data acquisition system for testing the photomultiplier arrays.

The photocurrent was measured using a computer controlled HP Semiconductor Parameter Analyzer model 4145B. A computer with ICCAP data acquisition was used to record the photocurrent through a general-purpose interface bus (GPIB) connection to the HP4145B. The ND filters was used to reduce the intensity of light sources to prevent light saturation on the devices.

In Figure 5.12 and Figure 5.13 the responsivity (R) and quantum efficiency extracted from the photocurrent measurements are shown the three types of GePM. The quantum efficiency (QE) is wavelength dependent and related to responsivity. The QE is equal to $1240 \times R/\lambda$, where λ is the specific wavelength in nanometers. The sensitivity for near infrared wavelengths is higher than for visual wavelengths as would be expected. Moreover, the responsivity/QE increase as the number of diodes in the GePM pixels is increased.

5.4.4 Low temperature optical gain

The total current was measured for three GePMs with the reverse bias voltage going from 0 to -26 V while the devices were illuminated by one of the sources. The output power of the laser sources is 14.5 mW, 7.7 mW, and 6.5 mW for wavelength of 660 nm, 850 nm, and 940 nm, respectively. However, the incident optical power on the devices was attenuated by the distance and filters, resulting in 9.8 μW, 0.75 μW, and 0.78 μW for the respective laser sources.

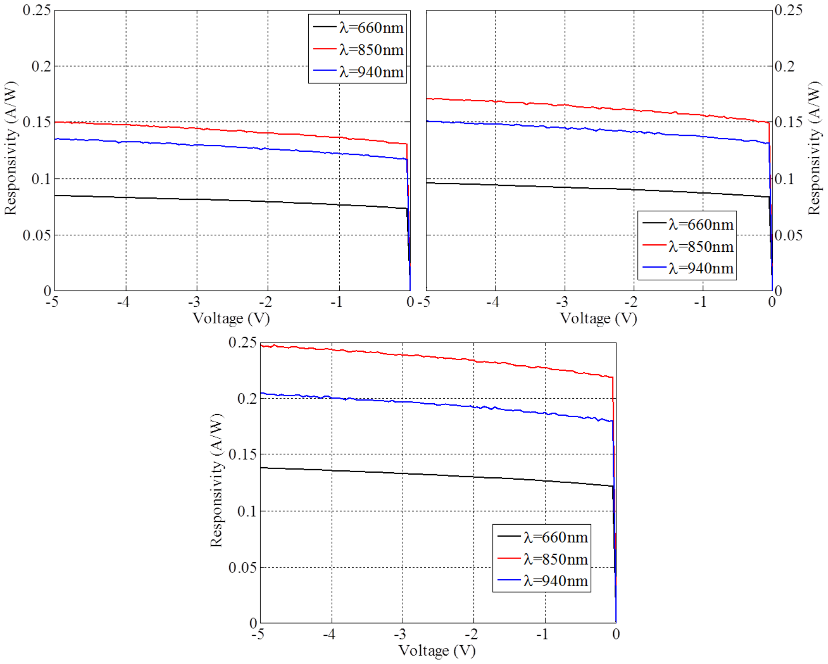

Figure 5.12: Responsivity for three wavelengths at 77 K: (top-left) single GePM, (top-right) quad GePM, (bottom) hexa GePM.

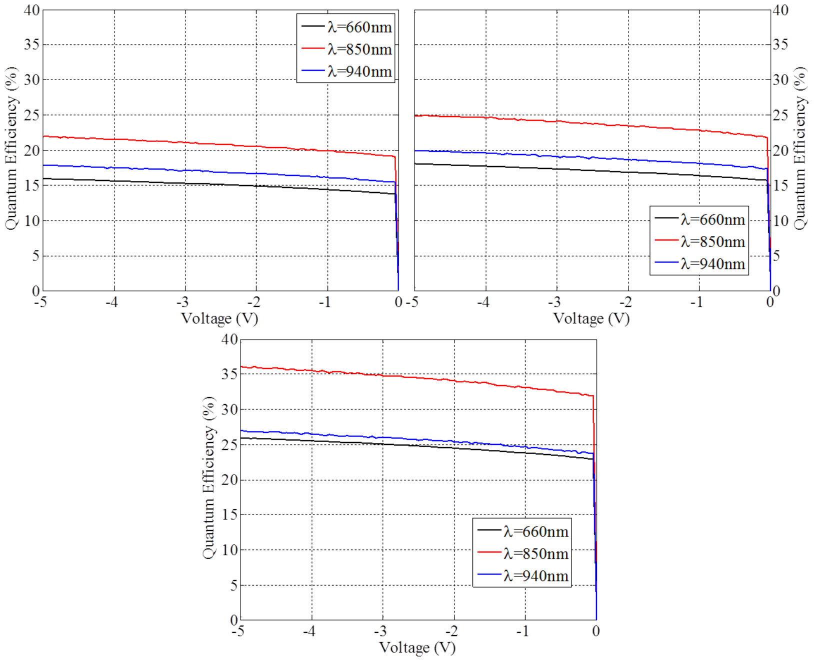

Figure 5.13: Quantum efficiency for three wavelengths at 77 K: (top-left) single GePM, (top-right) quad GePM, (bottom) hexa GePM.

The optical gain is calculated by normalizing the responsivity of the device in APD mode to a reference responsivity taken at 1 V reverse bias. The responsivity at lower bias voltages is shown in Figure 5.12. The optical gain for three different wavelengths at 77 K is also shown in Figure 5.14. For this parameter the NIR wavelengths also display higher values than the visual wavelength, with 940 nm giving the highest optical gain. Any leakage current in the device enhances the multiplication process so variations in dark current due to defects have an influence on the measured optical gain. The difference in optical gain from device type to device type is therefore likely related to the spread in dark current rather than geometrical effects.

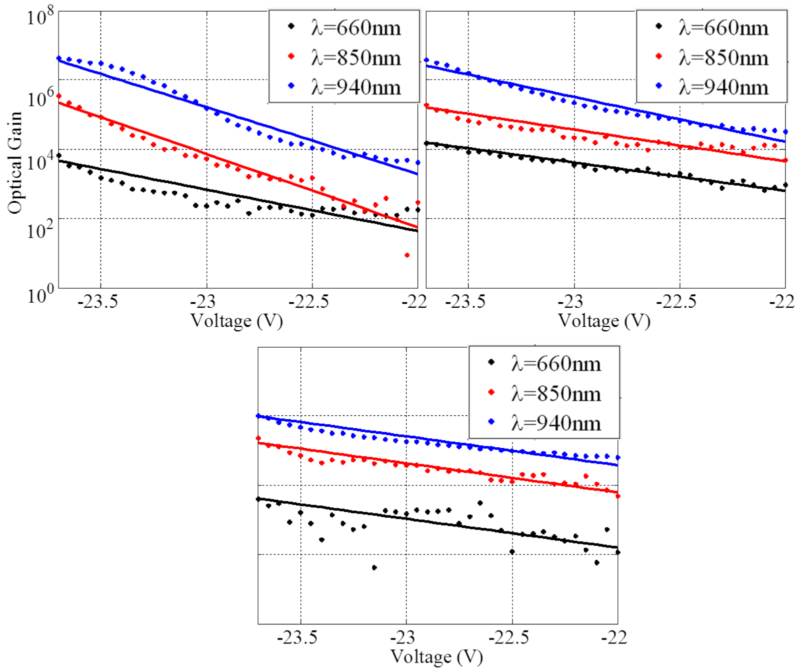

Figure 5.14: Optical gain as a function of reverse voltage for 3 different wavelengths at 77 K (top-left) single GePM, (top-right) quad GePM, (bottom) hexa GePM.

The influence of the spread in dark current is underlined by spread in optical gain displayed in Figure 5.15 for the three different arrays of 300 × 1 GePMs. At least 70 pixels are measured on the same die and over four different dies.

The relationship between optical gain and breakdown voltage spreading is evaluated by plotting the maximum optical gain as a function of V_{BD} in Figure 5.16. The horizontal axis shows the spreading of V_{BD}. From this plot it is clear, as noted in the previous section, that although the breakdown voltage is similar for all three GePMs, the spreading is lowest for the hexa GePM array. This is also true for the spread in maximum optical gain. The standard deviation is represented by the red ellipse for σ and the blue ellipse for 3σ.

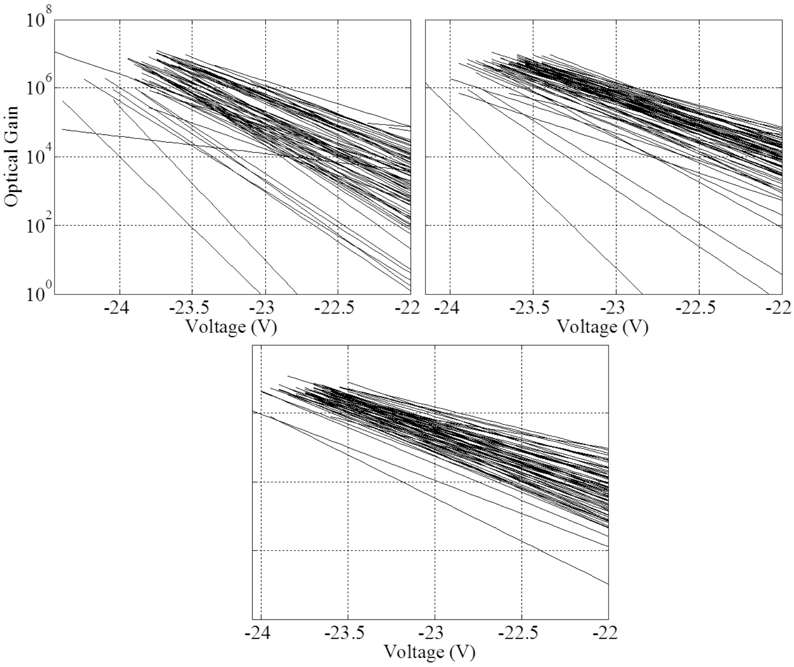

Figure 5.15: Optical gain spread across 70 devices measured at 940 nm and 77 K (top-left) single GePM, (top-right) quad GePM, (bottom) hexa GePM.

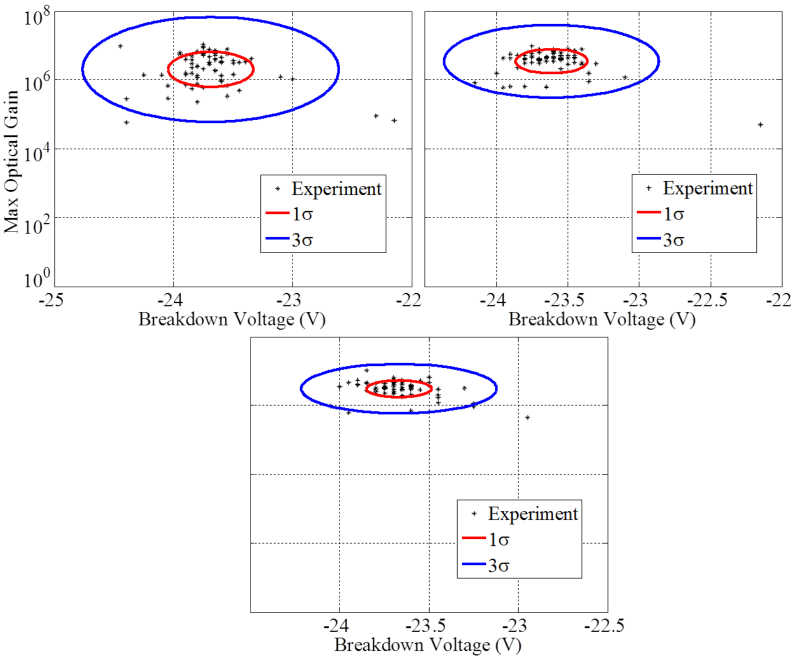

Figure 5.16: Spreading of maximum optical gain versus breakdown voltage across 70 devices measured at 940 nm and 77 K (top-left) single GePM, (top-right) quad GePM, (bottom) hexa GePM.

5.4.5 Performance summary

The mean values of maximum optical gain and the breakdown voltage as well as its standard deviation are listed in Table 5.3. The spreading of V_{BD} is 0.78%, 1.07%, and 1.52% for hexa, quad, and single GePMs, respectively.

Table 5.3: Summary of performance of the GePMs.

	Mean of V_{BD}	$\sigma(V_{BD})$	Mean of MAX Gain
Single GePM	-23.69V V	0.36V	3.18×10^6
Quad GePM	-23.61V	0.25V	4.16×10^6
Hexa GePM	-23.67V	0.18V	3.42×10^6

Table 5.4 gives a summary of the performance of the best devices among the measured GePMs as well as a comparison with devices found in the literature. The dark current density of the Single GePM for 1 V reverse bias at 300 K and 77 K is less than 35 $\mu A/cm^2$ and 2.5×10^{-2} $\mu A/cm^2$, respectively. The dark current density decreases to 13 $\mu A/cm^2$ and 2.5×10^{-2} $\mu A/cm^2$, respectively, for the hexa GePM. The QE increases from nearly 22% for the single GePM to 35% for hexa GePM device at 850 nm, and from 17.8% to 27% at 940 nm.

Table 5.4: Summary of overall best performance compared with several Ge photodetector designs reported in the literature.

Device	Ge Thickness $[\mu m]$	Dark current Density @-1 V,300 K $[\mu A/cm^2]$	Responsivity @77 K (A/W)	QE @77 K (%)
Single GePM	0.6	35	0.15 @850nm 0.135 @940nm	21.9 @850nm 17.8 @940nm
Quad GePM	0.6	18	0.17 @850nm 0.151 @940nm	24.8 @850nm 19.9 @940nm
Hexa GePM	0.6	13	0.24 @850nm 0.205 @940nm	35 @850nm 27 @940nm
Ref [102]	0.4	1500	0.18 @850nm	22 @850nm
Ref [103]	–	62	0.55 @1500nm	45 @1550nm
Ref [35]	1.1	19	0.55 @1300nm	52 @1300nm

The 3 different types of GePM, with very different Ge diode areas and perimeters, all have very good electrical and optical performance. They have about the same breakdown voltage with low spread (23.6±0.4 V), and a high maximum optical gain that spreads over values in the 10^6 range when measured at 77 K. The hexa design, with the smallest Ge diodes, smaller total Ge area but larger perimeter than the single and quad GePMs, appears to provide the most optimal performance with respect to spread in dark current and optical gain at cryogenic temperatures. The results indicate that this is due to the fact that smaller Ge islands are less prone to the formation of dislocations that are induced during Ge growth to correct for the lattice mismatch between the Ge and underlying Si. The lower number of Ge-related defects in the hexa design is nevertheless electrically more dominating than the oxide-to-Si interface traps that are depleted at the Ge diode perimeter. This perimeter is quite large for the hexa design but although it would be the main source of electrically-active defects in a good pure-Si photodiode, this is not the case for these Ge-on-Si diodes. This suggests that the individual diode size can be scaled down even further to reduce bulk Ge defects without paying a penalty in electrical and optical performance.

6 Conclusions

6.1 Achieved results

The first objective of this thesis was to design silicon and germanium avalanche photodiodes for the visible and near infrared ranges that can potentially mass-produced and are intended for bio-medical applications, with a particular emphasis on drugs and doping agent detection in bodily fluids.

Novel Ge-on-Si avalanche photodiodes were demonstrated to operate at near-infrared and visible wavelengths, while being compatible with standard CMOS processes. The APDs were demonstrated both in proportional and in Geiger mode of operation. In Geiger mode of operation a virtually infinite optical gain is achieved, thus enabling detection of single photons. The device fabrication took advantage of important innovations introduced by Prof. Nanver's group in Delft, such as a new selective chemical-vapor deposition (CVD) epitaxial growth and a novel processing technique (PureGaB) for p-Ge surface doping.

The fabricated Ge-on-Si SPADs exhibit relatively low dark counts and high sensitivity at room temperature. This correlates well with the fact that the I-V characteristics have, to our knowledge, uniquely low values of reverse current, series resistance and ideality factors as well as good uniformity over the wafer. Dark current of 2 pA, dark count rates of 10 kHz, 27% peak of I_d/I_{ref} at an IR-wavelength of 1100 nm in Geiger mode, and timing response of 900 ps were measured.

Arrays of Ge-on-Si SPADs were also demonstrated to study large numbers of SPADs and their statistical performance in real conditions of operation. Germanium photomultipliers (GePMs) were introduced with various geometries to study the tradeoff of geometric parameters, and perimeter effects. A design of a 300 × 1 array of PureGaB GePMs of various sizes were designed and tested in this context. A study of breakdown variability (23.6±0.4 V) and cryogenic performance of SPADs at 77 K completed the picture to give us an general understanding of the potential of this technology.

The spread in dark current and optical gain at cryogenic temperatures has been examined in detail and a correlation between performance and the size of Ge islands was found to be less sensitive to dislocations than to Ge growth. The lower number of Ge-related defects in the some designs is nevertheless electrically more dominating than the oxide-to-Si interface traps that are depleted at the diode perimeter.

The second objective of this thesis was the demonstration of deep silicon p-n junction devices as an alternative to Ge for photon detection at 800-900nm. The red and NIR single-photon avalanche diodes, implemented in advanced 180nm imaging sensor technology, were extensively simulated and tested. The SPAD achieves high PDP at 500nm, peaking to 29% at 4 V excess bias, and 13% at 700nm wavelengths. Moreover, the jitter of the SPAD is lower for the deep-red laser (785nm) than that for the red laser (637nm). Dark count rates are lower than 5 $Hz/\mu m^2$ at room temperature, whereas decreasing drastically in cryogenic temperatures. The low timing jitter as 74 ps and small afterpulsing probability of less than 1.5% at 6 V excess bias voltage were achieved.

6.2 Future developments

The fabricated structures have the potential to enable a new generation of massively parallel, Ge-on-Si sensors fabricated in fully CMOS compatible technology. The objective is here to address the next challenges of super-parallel pixel arrays, while exploiting the advantages of Ge substrate, *in primis* its higher mobility. Ultimately, we believe that this technology will become the core of next-generation processors and embedded accelerators operating at very high clock frequencies and, possibly, controlled optically, an idea we started exploring in fully CMOS circuits.

Bibliography

[1] W. S. Zaoui, H. W. Chen, J. E. Bowers, Y. Kang, M. Morse, M. J. Paniccia, A. Pauchard, and J. C. Campbell. Frequency response and bandwidth enhancement in Ge/Si avalanche photodiodes with over 840GHz gain-bandwidth-product. *Opt. Express*, 17(15):12641–12649, Jul 2009.

[2] M. Graf, N. Hoyler, M. Giovannini, J. Faist, and D. Hofstetter. InP based quantum cascade detectors in the mid infrared. *Applied Physics Letters*, 88(24):241118, 2006.

[3] F.R. Giorgetta, E. Baumann, D. Hofstetter, C. Manz, Q. Yang, K. Kohler, and M. Graf. InGaAs/AlAsSb quantum cascade detectors operating in the near infrared. *Applied Physics Letters*, 91(11):111115, 2007.

[4] F. R. Giorgetta, E. Baumann, R. Theron, M. L. Pellaton, D. Hofstetter, M. Fischer, and J. Faist. Short wavelength (4μm) quantum cascade detector based on strain compensated InGaAs/InAlAs. *Applied Physics Letters*, 92:121101, 2008.

[5] S. Cova, A. Longoni, A. Andreoni, and R. Cubeddu. A Semiconductor Detector for Measuring Ultraweak Fluorescence Decays with 70ps FWHM Resolution. *IEEE Journal of Quantum Electronics*, 10(4):630–634, 1983.

[6] A. Rochas, M. Gani, B. Furrer, P. A. Besse, R. S. Popovic, G. Ribordy, and N. Gisin. Single photon detector fabricated in a complementary metal-oxide-semiconductor high-voltage technology. *Review of Scientific Instruments*, 74(7):3263—3270, 2003.

[7] C. Niclass, A. Rochas, P.A. Besse, and E. Charbon. Design and Characterization of A CMOS 3D Image Sensor based on Single Photon Avalanche Diodes. *IEEE Journal of Solid-State Circuits*, 40(9):1847–1854, 2005.

[8] M. R. McCurdy, Y. Bakhirkin, G. Wysocki, R. Lewicki, and F. K. Tittel. Recent advances of laser-spectroscopy-based techniques for applications in breath analysis. *Journal of Breath Research*, 1(1):014001, 2007.

[9] A. Amann and D. Smith. *Breath analysis for clinical diagnosis and therapeutic monitoring*. New Jersey: World Scientific, 2005.

[10] B. Braden, B. Lembcke, W. Kuker, and W. F. Caspary. ^{13}c-breath tests: Current state of the art and future directions. *Digestive and Liver Disease*, 39(9):795–805, 2007.

[11] A. S. Modak. Stable isotope breath tests in clinical medicine: A review. *Journal of Breath Research*, 2007(1):1–13, 2007.

[12] E. R. Crosson, K. N. Ricci, B. A. Richman, F. C. Chilese, T. G. Owano, R. A. Provencal, M. W. Todd, J. Glasser, A. A. Kachanov, B. A. Paldus, T. G. Spence, and R. N. Zare. Stable isotope ratios using cavity ring-down optical spectroscopy: determination of 13C/12C for carbon dioxide in human breath. *Analytical Chemistry*, 74(9):2003–2007, 2002.

[13] A. Sammak. *Silicon-Based Integration of Groups III, IV, V Chemical Vapor Depositions in High-Quality Photodiodes*. PhD thesis, Technische Universiteit Delft, 2012.

[14] Giancarlo Barbarino, Riccardo de Asmundis, Gianfranca De Rosa, Carlos Maximiliano Mollo, Stefano Russo, and Daniele Vivolo. *Silicon Photo Multipliers Detectors Operating in Geiger Regime: an Unlimited Device for Future Applications*. Photodiodes - World Activities, 2011.

[15] S. O. Kasap. *Optoelectronics and Photonics, Principles and Practices*. Prentice-Hall International, 2001.

[16] A. M. Joshi and G. H. Olsen. Photodetectors. *Handbook of Optics: Fundamentals, Techniques, and Design*, I, 1995.

[17] John Ballato and Mool C. Gupta. *The Handbook of Photonics*. Second edition, CRC Press, Boca Raton, 2006.

[18] S. M. Sze. *Semiconductor Devices: Physics and Technology*. John Wiley, 1985.

[19] M. A. Karami. *Deep-submicron CMOS Single Photon Detectors and Quantum Effects*. PhD thesis, Technische Universiteit Delft, 2011.

[20] E. Charbon and S. Donati. SPAD sensors come of age. *Optics and photonics news (OPN)*, 21:35–41, 2010.

[21] H. Finkelstein. *Shallow-trench-isolation bounded single-photon avalanche diodes in commercial deep submicron CMOS technologies*. PhD thesis, University of California, San Diego, 2007.

[22] Y. Kang, M. Zadka, S. Litski, G. Sarid, M. Morse, M. J. Paniccia, Y. H. Kuo, J. Bowers, A. Beling, H. D. Liu, D. C. McIntosh, J. Campbell, and A. Pauchard. Epitaxially-grown Ge/Si avalanche photodiodes for 1.3 μm light detection. *Opt. Express*, 16:9365–9371, 2008.

[23] R. P. Webb, R. J. McIntyre, and J. Conradi. Properties of avalanche photodiodes. *RCA Rev*, 35:234–278, 1974.

[24] M. Gersbach. *Single-Photon Detector Arrays for Time-Resolved Fluorescence Imaging*. PhD thesis, Ecole Polytechnique Fédérale De Lausanne (EPFL), 2009.

[25] T. Yin, R. Cohen, M. M. Morse, G. Sarid, Y. Chetrit, D. Rubin, and M. J. Paniccia. 31 GHz Ge n-i-p waveguide photodetectors on Silicon-on-Insulator substrate. *Opt. Express*, 15:13965–13971, 2007.

[26] L. Vivien, J. Osmond, J. Fédéli, D. Marris-Morini, P. Crozat, J. Damlencourt, E. Cassan, Y. Lecunff, and S. Laval. 42 GHz p-i-n Germanium photodetector integrated in a silicon-on-insulator waveguide. *Opt. Express*, 17:6252–6257, 2009.

[27] M. Casalino, L. Sirleto, L. Moretti, F. Della Corte, and I. Rendina. Design of a silicon RCE Schottky photodetector working at 1.55 μm. *Journal of Luminescence*, 121:399–402, 2006.

[28] A. Sammak, M. Aminian, L. Qi, W. B. de Boer, E. Charbon, and L. K. Nanver. A CMOS compatible Ge-on-Si APD operating in proportional and Geiger modes at infrared wavelengths. In *Proc. IEDM*, pages 8.5.1–8.5.4, 2011.

[29] R. Nihei, N. Usami, and K. Nakajima. Growth of Compositionally Graded SiGe Bulk Crystal and Its Application As Substrate with Lateral Variation in Ge Content. *Japanese Journal of Applied Physics*, 48(11R):115507, 2009.

[30] O. I. Dosunmu, D. D. Cannon, M. K. Emsley, L. C. Kimerling, and M. S. Ünlü. High-Speed Resonant Cavity Enhanced Ge Photodetectors on Reflecting Si Substrates for 1550-nm Operation. *IEEE Photonics Technology Letters*, 17:175–177, 2005.

[31] E. Kasper, M. Oehme, J. Werner, M. Jutzi, and M. Berroth. Fast Ge p-i-n photodetectors on Si. In *SiGe Technology and Device Meeting*, pages 1–2, 2006.

[32] M. Casalino, G. Coppola, M. Gioffrè, M. Iodice, L. Moretti, I. Rendina, and L. Sirleto. Cavity Enhanced Internal Photoemission Effect in Silicon Photodiode for Sub-Bandgap Detection. *Journal of Lightwave Technology*, 28(22):3266–3272, 2010.

[33] L. Vivien, M. Rouvière, J. Fédéli, D. Marris-Morini, J. F. Damlencourt, J. Mangeney, P. Crozat, L. El Melhaoui, E. Cassan, X. Le Roux, D. Pascal, and S. Laval. High speed and high responsivity germanium photodetector integrated in a Silicon-On-Insulator microwaveguide. *Optics Express*, 15:9843–9848, 2007.

[34] Y. Kang, M. Morse, M. J. Paniccia, M. Zadka, Y. Saad, G. Sarid, A. Pauchard, W. S. Zaoui, H. Chen, Daoxin Dai, J. E. Bowers, H. Liu, D. C. Mcintosh, X. Zheng, and J. C. Campbell. Monolithic Ge/Si Avalanche Photodiodes. In *IEEE International Conference on Group IV Photonics*, pages 25–27, 2009.

[35] Y. Kang, H. D. Liu, M. Morse, M. J. Paniccia, M. Zadka, S. Litski, G. Sarid, A. Pauchard, Y. H. Kuo, H. W. Chen, W. S. Zaoui, J. E. Bowers, A. Beling, D. C. McIntosh, X. Zheng, and J. C. Campbell. Monolithic Ge/Si Avalanche Photodiodes with 340GHz Gain-Bandwidth Product. *Nature Photonics*, 3:59–63, 2008.

[36] G. Rieke. *Detection of Light: from the Ultraviolet to the Submillimeter.* Second edition, Cambrige, 2003.

[37] Canberra. High-purity Germanium (HPGe) Detectors. http://canberra.com/products/detectors/germanium-detectors.asp, 2014.

[38] Xenics. Near infrared InGaAs detectors. http://xenics.com/en/infrared_technology/what_are_ingaas_detectors.asp, 2014.

[39] J. G. Fiorenza, J. Park, J. M. Hydrick, J. Li, J. Li, M. Curtin, M. Carroll, and A. Lochtefeld. Aspect ratio trapping: a unique technology for integrating Ge and III-Vs with Silicon CMOS. *ECS transaction*, 33(6):963–976, 2010.

[40] J. Park, J. Bai, M. Curtin, B. Adekore, M. Carroll, and A. Lochtefeld. Defect reduction of selective Ge epitaxy in trenches on Si(001) substrates using aspect ratio trapping. *Applied Physics Letter*, 5(90):052113, 2007.

[41] I. Åberg, B. Ackland, J. V. Beach, C. Godek, R. Johnson, C. A. King, A. Lattes, J. O'Neill, S. Pappas, T. S. Sriram, and C. S. Rafferty. A low dark current and high quantum efficiency monolithic germanium-on-silicon CMOS imager technology for day and night imaging applications. In *Electron Devices Meeting (IEDM)*, pages 14.4.1–14.4.4, 2010.

[42] C. Niclass. *Single-Photon Image Sensors in CMOS: Picosecond Resolution for Three–Dimensional Imaging.* PhD thesis, Ecole Polytechnique Fédérale De Lausanne (EPFL), 2008.

[43] E. R. Fossum. Active pixel sensors: are CCDs dinosaurs? In *Proceedings of SPIE Vol. 1900, Charge-Coupled Devices and Solid State Optical Sensors III*, pages 2–14, 1993.

[44] Hamamatsu Photonics. Silicon APD product family. http://hamamatsu.com, 2014.

[45] G. S. Buller and A. M. Wallace. Ranging and three-dimensional imaging using time-correlated single-photon counting and point-by-point acquisition. *IEEE Journal on Selected Topics in Quantum Electronics*, 13(4), 2007.

[46] Y. Maruyama, J. Blacksberg, and E. Charbon. A 1024×8 700ps time-gated SPAD line sensor for laser raman spectroscopy and LIBS in space and rover-based planetary exploration. In *IEEE Solid-State Circuits Conference (ISSCC)*, pages 110–111, 2013.

[47] C. Niclass, M. Sergio, and E. Charbon. A single photon avalanche diode array fabricated in 0.35-μm CMOS and based on an event-driven readout for TCSPC experiments. In *SPIE Advance Photon Counting Technology Meeting*, 2006.

[48] B. Saleh and M. Teich. *Fundamentals of Photonics.* Wiley, 1994.

[49] R. H. Haitz. Mechanisms contributing to the noise pulse rate of avalanche diodes. *Journal of Applied Physics*, 36(10):3123–3131, 1965.

[50] S. Cova, A. Lacaita, and G. Ripamonti. Trapping phenomena in avalanche photodiodes on nanosecond scale. *IEEE Electron Device Letters*, 12(12):685–787, 1991.

[51] S. Cova, A. Longoni, and A. Andreoni. Towards picosecond resolution with single-photon avalanche diodes. *Review of Scientific Instruments*, 52:408–412, 1981.

[52] A. Lacaita, M. Mastrapasqua, M. Ghioni, and S. Vanoli. Observation of avalanche propagation by multiplication assisted diffusion in pn junctions. *Applied Physics Letters*, 57(5):489–491, 1990.

[53] A. Lacaita, S. Cova, A. Spinelli, and F. Zappa. Photon assisted avalanche spreading in reachthrough photodiodes. *Applied Physics Letters*, 62(6):606–608, 1993.

[54] G. Ripamonti and S. Cova. Carrier diffusion effects in the timeresponse of a fast photodiode. *Solid-State Electronics*, 28(9):925–931, 1984.

[55] M. Gersbach, J. Richardson, E. Mazaleyrat, S. Hardillier, C. Niclass, R. Henderson, L. Grant, and E. Charbon. A low-noise single-photon detector implemented in a 130 nm CMOS imaging process. *Solid-State Electron*, 53(7):803–808, 2009.

[56] J. A. Richardson, L. A. Grant, and R. K. Henderson. Low dark count single-photon avalanche diode structure compatible with standard nanometer scale CMOS technology. *IEEE Photon. Technol. Lett*, 21(14):1020–1022, 2009.

[57] A. Rochas. *Single photon avalanche diodes in CMOS technology*. PhD thesis, Ecole Polytechnique Fédérale De Lausanne (EPFL), 2003.

[58] E. A. G. Webster, J. A. Richardson, L. A. Grant, D. Renshaw, and R. K. Henderson. An infrared sensitive, low noise, single-photon avalanche diode in 90nm CMOS. In *International Image Sensors Workshop (IISW)*, 2011.

[59] M. A. Karami, M. Gersbach, H. J. Yoon, and E. Charbon. A new single-photon avalanche diode in 90nm standard CMOS technology. *Optics Express*, 18(21):102–105, 2010.

[60] S. Mandai, M. Fishburn, Y. Maruyama, and E. Charbon. A wide spectral range single-photon avalanche diode fabricated in an advanced 180 nm CMOS technology. *Optics Express*, 20:5849–5857, 2012.

[61] Synopsys. Device simulation, tools for simulating device performance. http://www.synopsys.ch/Tools/TCAD/DeviceSimulation/Pages/default.aspx, 2014.

[62] S. Selberherr. *Analysis and Simulation of Semiconductor Devices*. Spring-Verlag, Wien, New York, 1984.

[63] A. Tosi, A. Dalla Mora, S. Tisa, F. Acerbi, F. Zappa, and S. Cova. InGaAs/InP SPADs for near-infrared applications: device operating conditions and dedicated electronics. In *Proc. SPIE*, volume 7681, page 76810R, 2010.

[64] R. T. Thew, S. Tanzilli, L. Krainer, S. C. Zeller, A. Rochas, I. Rech, S. Cova, H. Zbinden, and N. Gisin. Low jitter up-conversion detectors for telecom wavelength GHz QKD. *New J. Phys*, 8(32), 2006.

[65] M. Morse, O. Dosunmu, G. Sarid, and Y. Chetrit. Performance of Ge-on-Si p-i-n Photodetectors for Standard Receiver Modules. *IEEE Photonics Technology Letters*, 18(23):2442–2444, 2006.

[66] J. Michel, J. Liu, and L. C. Kimerling. High-Performance Ge-on-Si Photodetectors. *Nature Photonics*, 4(8):527–534, 2010.

[67] M. Kim, O. Olubuyide, J. Yoon, and J. Hoyt. Selective epitaxial growth of Ge-on-Si for photodiode applications. *ECS Transactions*, 16(10):837–847, 2008.

[68] R. Jakomin, G. Beaudoin, N. Gogneau, B. Lamare, and I. Sagnes. *n and p-doped germanium grown by MOVPE for solar cell applications.* EWMOVPE XIII, Ulm, 2009.

[69] J. Nakatsuru, H. Date, S. Mashiro, and M. Ikemoto. Growth of high quality Ge epitaxial layer on Si(100) substrate using ultra thing Si0.5 Ge0.5 buffer. *Mater. Res. Soc. Symp. Proc.*, 891:24.1–24.6, 2006.

[70] Z. Huang, J. Oh, and C. Campbell. Ge on Si photodiodes for Si CMOS monolithic optical receivers. *ECS Transactions*, 3(39):1–10, 2007.

[71] H. Y. Yu, S. L. Cheng, J. H. Park, A. K. Okyay, M. C. Onbas¸li, B. Ercan, Y. Nishi, and K. C. Saraswat. High quality single-crystal germanium-on-insulator on bulk Si substrates based on multistep lateral over-growth with hydrogen annealing. *Applied Physics Letters*, 97(6):063 503, 2010.

[72] K. Terashima, A. Tanabe, T. Nakagawa, K. Mori, T. Ikarashi, J. Nakatsuru, H. Date, M. Ikemoto, and T. Tatsumi. Fabrication of Ge-channel MOSFETs by using replacement gate process and selective epitaxial growth. *Applied Surface Science*, 254(19):6165–6167, 2008.

[73] A. Sammak, W. B. de Boer, and L. K. Nanver. Ge-on-Si: Single-Crystal Selective Epitaxial Growth in a CVD Reactor. *ECS transaction*, 50(9):506–512, 2012.

[74] A. Sammak, M. Aminian, L. Qi, W. B. de Boer, E. Charbon, and L. K. Nanver. Fabrication of PureGaB Ge-on-Si photodiodes for well-controlled 100-pA-level darek currents. In *Electro-Chemical Society (ECS) Meeting*, 2014.

[75] A. Sammak, W. D. de Boer, L. Qi, and L. K. Nanver. High-quality p+n Ge diodes selectively grown on Si with a sub-300nm transition region. In *Proc. European Solid-State Device Research Conference (ESSDERC*, pages 359–362, 2011.

[76] F. Sarrubi, T. L. M. Scholtes, and L. K. Nanver. Chemical vapor deposition of α-boron layers on silicon for controlled nanometer-deep p+n junction formation. *Journal of electronic materials*, 39(2):162–173, 2010.

[77] A. Sammak, L. Qi, W. de Boer, and L. K. Nanver. Chemical vapor deposition of Ga dopants for fabricating ultrashallow p-n junctions at 400°C. In *Proc ICSICT*, pages 969–971, 2010.

[78] Delft Institute for Microsystems and Nanoelectronics (DIMES). Dimes03 manual. http://duteela.et.tudelft.nl/~elca/ICdesign/dimes03/index.html, 2014.

[79] M. W. Fishburn. *Fundamentals of CMOS Single-Photon Avalanche Diodes*. PhD thesis, Technische Universiteit Delft, 2012.

[80] J. Richardson, L. Grant, and R. Henderson. Low dark count single-photon avalanche diode structure compatible with standard nanometer scale CMOS technology. *IEEE Photon. Technol. Lett.*, 21(14):1020–1022, 2009.

[81] S. Cova, A. Longoni, A. Andreoni, and R. Cubeddu. A semiconductor detector for measuring ultraweak fluorescence decays with 70 ps FWHM resolution. *IEEE Journal of Quantum Electronics*, 19:630–634, 1983.

[82] M. Aminian, A. Sammak, L. Qi, L. Nanver, and E. Charbon. A Ge-on-Si Single-Photon Avalanche Diode Operating in Geiger Mode at Infrared Wavelengths. In *SPIE international symposium on Defense, Security, and Sensing*, page 83750Q, 2012.

[83] Z. Lu, Y. Kang, C. Hu, Q. Zhou, H. Liu, and J. C. Campbell. Geiger-mode operation of Ge-on-Si avalanche photodiodes. *Journal of Quantum Electronics*, 47(5):731–735, 2011.

[84] A. Sammak, L. Qi, W. B. de Boer, and L. K. Nanver. Puregab p+n Ge diodes grown in large windows to Si with a sub-300 nm transition region. *Solid-State Electronics*, 74:126–133, 2012.

[85] L. Qi, K. R. C. Mok, L. K. Nanver, M. Aminian, and E. Charbon. Uv-sensitive low dark-count PureB single-photon avalanche diode. In *IEEE Sensors*, pages 1–4, 2013.

[86] V. Saveliev. The recent development and study of silicon photomultiplier. *Nucl. Instrum. Methods Phys. Res. A*, 535:528–532, 2004.

[87] E. Charbon. Single-photon Imaging in Complementary Metal Oxide Semiconductor Processes. *Phil. Trans. R. Soc. A*, 372:20130100, 2014.

[88] A. Sammak, M. Aminian, L. Qi, E. Charbon, and L. K. Nanver. A 270×1 Ge-on-Si photodetector array for sensitive infrared imaging. In *European SPIE*, 2014.

[89] International Institute of Refrigeration (IIR). International Dictionary of Refrigeration, 1975.

[90] Ph. Lebrun. An Introduction to Cryogenics, 2007.

[91] E. A. Gutierrez, M. J. Deen, and C. Claeys. *Low temperature electronics: physics, devices, circuits and applications*. Academic Press, 2000.

[92] A. K. Jonscher. Semiconductors at cryogenic temperatures. *Proceedings of the IEEE*, 52(10):1092–1104, 1964.

[93] Varshni YP. Temperature dependence of the energy gap in semiconductors. *Physica*, 34:149–154, 1967.

[94] E.D.H. Green. Temperature Dependence of Semiconductor Conductivity. http://classes.soe.ucsc.edu/ee145/Fall04/EE145_04_Lab5b.pdf, 2014.

[95] A. L. Woodcraft. *An introduction to cryogenics*. Institute for Astronomy, Edinburgh University, 2007.

[96] Cascade Microtech. PMC 150 Manual. http://wiki.epfl.ch/carplat, 2014.

[97] A. Vassighi and M. Sachdev. *Thermal and Power Management of Integrated Circuits*. Springer, 2006.

[98] H. T. J. Meier. *Design, Characterization and Simulation of Avalanche Photodiodes*. PhD thesis, ETH Zurich, 2011.

[99] B. M. Wilamowski. *Semiconductor Diode, Fundamentals of Industrial Electronics*. 2nd Edition, chapter 8, CRC Press, 2011.

[100] W. F. Clark, B. El-Kareh, R. G. Pires, S. L. Titcomb, and R. L. Anderson. Low temperature CMOS - A brief review. *IEEE Transaction on Components, Hybrids, and Manufacturing Technology*, 15(3), 1992.

[101] R. L. Aggarwal, I. Melngailis, S. Verghese, R. J. Molnar, M. W. Geis, and L. J. Mahoney. Temperature dependence of the break-down voltage for reverse-biased GaN p–n–n+ diodes. *Solid State Communications*, 117(9), 2001.

[102] T. H. Loh, H. S. Nguyen, R. Murthy, M. B. Yu, W. Y. Loh, G. Q. Lo, N. Balasubramanian, D. L. Kwong, J. Wang, and S. J. Lee. Selective epitaxial germanium on silicon-on-insulator high speed photodetectors using low-temperature ultrathin Si0.8Ge0.2 buffer. *Applied Physics Letters*, 91(7):073503, 2007.

[103] M. Takenaka, K. Morii, M. Sugiyama, Y. Nakano, and S. Takagi. Dark current reduction of Ge photodetector by GeO2 surface passivation and gas-phase doping. *Optics Express*, 20(8):8718–8725, 2012.

Curriculum Vitae

MAHDI AMINIAN

Personal and Contact information

Born in Iran, 13/06/1984

email mahdi.aminian@epfl.ch

Mhd.aminian@gmail.com

Professional address EPFL SCI STI EC

INF 134, Station 14

CH-1015 Lausanne, Switzerland

Education

2009-2014 PhD in Electrical Engineering,

École Polytechnique Fédérale de Lausanne (EPFL), Lausanne, Switzerland.

Thesis title: “Ultra-Low Temperature Silicon and Germanium-on-Silicon Avalanche Photodiodes: Modeling, Design, and Characterization”

Doctoral courses (12 credits), Nanoscale MOSFETs and beyond CMOS devices, Nano CMOS Devices & Technologies for Tera-Bit Circuits and Systems, Co-design of SOC on Reconfigurable Hardware, Real-time embedded systems, Electrochemical nano-bio-sensing and bio/CMOS interfaces, Microstructuring of glass.

2006-2008 Master of Science in Computer Architecture Engineering,

Amirkabir University of Technology (Tehran Polytechnic), Tehran, Iran.

Final Thesis: “Emulation of Quantum Circuits with FPGA”

2002-2006 Bachelor of Science in Computer (Hardware) Engineering,

Amirkabir University of Technology (Tehran Polytechnic), Tehran, Iran.

Final Thesis: “Designing Memory Interface Module (MIM) for MPC8280 Microprocessor by VHDL Language”

EXPERIENCES

2009-2014	Researcher as Doctoral assistant, Advanced Quantum Architecture Group, EPFL Design, implementation, and measurement of the first Ge-on-Si single photon avalanche diode (SPAD), working in near infrared wavelengths Design and implementation of Si SPAD devices for visible wavelengths and 1st Ge-on-Si APD Array for near infrared wavelengths
2009-2010	Internship, Quantum Optoelectronics Group, ETH Zurich Working on Waveguide simulations and design
2008-2009	Teaching assistantships Graduate Course of “Advanced VLSI Systems Design”, Undergraduate Course of “VLSI Systems Design”, and “Logic Circuits Design,” Amirkabir University, Tehran, Iran
2006-2008	Research Assistant, Quantum Design Automation Lab, Amirkabir University of Technology Working on various methods for emulation and simulation of Quantum Circuits VHDL implementation of some proposed quantum emulation methods
2007-2008	Teaching assistantships Graduate Course of “Algorithms for VLSI Physical Design”, Undergraduate Course of “Digital Electronics”, Amirkabir University, Tehran, Iran
2005-2006	Research Assistant, Electronic Design Automation Lab, Amirkabir University of Technology Member of Design and Implementation team of ATLAS project (Automatic Tool for LAyout Synthesis, a physical synthesis tool) Standard Cell Design and Implementation of a method for Global Placement of Standard Cells (By KDevelop in Linux)

PROFESSIONAL QUALIFICATIONS

Layout Tools: L-Edit and Cadence, and SKILL programming
Hardware Description Language: VHDL and Verilog
Device-Level Simulation Tools: MEDICI, SPECTRA, and COMSOL
Synthesis and Simulation Tools: Xilinx ISE, Quartus, Leonardo Spectrum, Spectre, HSpice, Modelsim, Active-HDL, and Matlab
Electronics Software: Altium PCB design, and Orcad
Computer programming in C++

AWARDS

2008	Ranked 2nd Highest GPA in Graduate Students of Computer Architecture, Amirkabir University of Technology

2006	The Best Senior Project of the Year 2006 - Recognized by Computer Engineering Department of Amirkabir University of Technology, entitled “Designing Memory Interface Module (MIM) for MPC8280 Microprocessor by VHDL Language”.
2006	Outstanding Undergraduate Students of Engineering Department of Amirkabir University of Technology, 2nd Highest GPA in Hardware Computer Engineering.

PUBLICATIONS

Journal Papers:

- L.Qi, K. Mok, **M. Aminian**, E. Charbon, L. K. Nanver, “UV-Sensitive Low Dark-Count PureB Single-Photon Avalanche Diode,” Transactions on Electron Devices, 2014.
- **M. Aminian**, M. Scandiuzzo, C. Bruschini, E. Charbon, “Deep Junction NIR-Sensitive Single Photon Avalanche Diode Working in Cryogenic Temperature,” Under submission to IEEE Electron Device Letter 2014.
- **M. Aminian**, A. Sammak, L. K. Nanver, E. Charbon, “Low-temperature characterization of near-infrared PureGaB Ge-on-Si photomultipliers,” Under submission.

Conference Papers:

- L. K. Nanver, L. Qi, A. Sammak, K. Mok, **M. Aminian**, E. Charbon, “Towards CMOS-Compatible Photon-Counting Imagers in the Whole 10 nm - 1600 nm Spectral Range with PureB Si and PureGaB Ge-on-Si Technology,” Invited paper to ICSICT 2014.
- A. Sammak, **M. Aminian**, L. Qi, E. Charbon, L. K. Nanver, “Fabrication of Pure-Gab Ge-on-Si Photodiodes for Well-Controlled 100-Pa-Level Dark Currents,” ECS 2014.
- A. Sammak, **M. Aminian**, L. Qi, E. Charbon and L. K. Nanver, “A 270x1 Ge-on-Si Photodetector Array for Sensitive Infrared Imaging,” SPIE Photonics 2014.
- L. Qi, K. Mok, **M. Aminian**, E. Charbon, L. Nanver, “Fabrication of Low Dark-Count PureB Single-Photon Avalanche Diodes”, SBMicro 2014.
- L. Qi, K. Mok, **M. Aminian**, T. Scholtes, E. Charbon, and L. Nanver, “Reverse Biasing and Breakdown Behavior of PureB Diodes”, IWJT 2013.
- **M. Aminian**, A. Sammak, L. K. Nanver, E. Charbon, “ A Ge-on-Si Single Photon Avalanche Diode Operating in Geiger Mode at Infrared Wavelengths”, SPIE international symposium on Defense, Security, and Sensing, April 2012.
- A. Sammak, **M. Aminian**, L. Qi, W. D. de Boer, E. Charbon, L. K. Nanver, “A CMOS Compatible Ge-on-Si APD Operating in Proportional and Geiger Modes at Infrared Wavelengths”, International Electron Device Meeting (IEDM), December 2011.
- **M. Aminian**, M. Saeedi, M. Saheb Zamani, M. Sedighi, “FPGA-Based Circuit Model Emulation of Quantum Algorithms”, IEEE International Symposium on VLSI (ISVLSI), 2008, PP. 399404.
- **M. Aminian**, M. Saeedi, M. Saheb Zamani, M. Sedighi, “Emulation of Quantum Circuits by FPGA”, the 13th International Computer Society of Iran Computer Conference (CSICC), 2008.

LANGUAGES

Persian: Mother tongue

English: Fluent (C1)

French: Intermediate (B1)

German: Beginner (A1)